



Durham E-Theses

Hadronic Higgs production with forward jets

Williams, Peter Howard

How to cite:

Williams, Peter Howard (2003) *Hadronic Higgs production with forward jets*, Durham theses, Durham University. Available at Durham E-Theses Online: <http://etheses.dur.ac.uk/3131/>

Use policy

The full-text may be used and/or reproduced, and given to third parties in any format or medium, without prior permission or charge, for personal research or study, educational, or not-for-profit purposes provided that:

- a full bibliographic reference is made to the original source
- a [link](#) is made to the metadata record in Durham E-Theses
- the full-text is not changed in any way

The full-text must not be sold in any format or medium without the formal permission of the copyright holders.

Please consult the [full Durham E-Theses policy](#) for further details.

Hadronic Higgs Production with Forward Jets

A copyright of this thesis rests with the author. No quotation from it should be published without his prior written consent and information derived from it should be acknowledged.

A thesis presented for the degree of

Doctor of Philosophy

by

Peter Howard Williams

Institute for Particle Physics Phenomenology

Department of Physics

University of Durham

September 2003



1 2 MAR 2004

Hadronic Higgs Production with Forward Jets

by

Peter Howard Williams

Abstract

The production of a Higgs boson with central rapidity, decaying to $b\bar{b}$ and accompanied by two jets that are forward in rapidity is presented as an important class of events at the Large Hadron Collider.

Specifically, we study central Z boson production accompanied by rapidity gaps on either side as a way to gauge Higgs production via weak boson fusion at the LHC. We analyse the possible backgrounds for the $b\bar{b}$ decay mode and show that these can be substantially reduced. Special attention is paid to the evaluation of the gap survival factor, which is the major source of theoretical uncertainty in the rate of H , Z and W central production events with rapidity gaps.

More generally, in relation to Higgs plus forward jet production, we consider the hadronic radiation patterns for the generic process of $b\bar{b}$ plus two forward jet production at the LHC, where the (centrally produced) $b\bar{b}$ originate either from a Higgs, a Z or from standard QCD production processes. A numerical technique for evaluating the radiation patterns for non-trivial final states is introduced and shown to agree with the standard analytic results for more simple processes. Significant differences between the radiation patterns for the Higgs signal and the background processes are observed and quantified. This suggests that hadronic radiation patterns could be used as an additional diagnostic tool in Higgs searches in this channel at the LHC.

We also study the applicability of an equivalent photon/gluon approximation in describing events with a central system accompanied by two forward jets.

Acknowledgements

Firstly, I would like to thank my supervisor, *James Stirling*, who's provision of ideas, guidance and physical intuition could always be relied upon. James had the patience to correct my understanding and inspire investigation of the subject at hand. Just as importantly, he encouraged me when problems arose and made them surmountable.

For a fruitful collaboration and vast knowledge of all areas of our field, I am indebted to *Valery Khoze*. I could count on Valery to explain the finer details of QCD and correct my English! I would also like to thank *Misha Ryskin* who contributed to the investigation in Chapter 4.

The IPPP has been a fun and friendly place in which to spend three years. Among the staff, I would especially like to thank *Nigel Glover* who kept a tight ship on the upper deck, although that sense of humour needs working on(!) *Mike Leech* and *Lydia Heck* deserve praise as the unsung heroes of the institute. Upgrades of both software and hardware occurred with high frequency and were implemented with aplomb. Also, this thesis was completed with the aid of Mike's laptop. *Dave Howe* and *Jon Levell* accompanied me on this journey for the full three years as office mates, mutual problem solvers (well, sometimes), curry eaters, beer drinkers and general dogsbody's. Toward the end of my time they were joined by *Anthony Owen*, *Ben Schofield* and *Thanos Koukoutsakis*. Past students *Kate Adamson*, *Jeppe Andersen*, *Lee Garland*, *Ania Kulesza* and *Neil Pomeroy* deserve credit for showing me the 'shining path'. *Adam Millican-Slater* and *James Haestier* should be mentioned for helping move our piano. All students with years to go have provided light relief during my writeup.

For emotional, financial and support of other forms more numerous to mention, thanks go to my Mother, Grandmother and Grandfather (who passed away during my time here) and my Parents-In-Law.

My Son, *Stuart*, was born halfway through my time in Durham and has provided many happy hours of distraction. My Daughter, *Natalie*, has grown into a kind and cheerful seven year old during these three years and should be thanked for sitting quietly during the final stages of this writeup.

This thesis is dedicated to my Wife, *Kate*, without whose love and endless patience this work would not have been possible.

Declaration

I declare that the work in this thesis has not previously been submitted for a degree at this or any other university.

Part of the research described in this thesis is the result of collaboration between V. A. Khoze, M. G. Ryskin, W. J. Stirling and the author and has been published in the following papers:

- V. A. Khoze, M. G. Ryskin, W. J. Stirling and P. H. Williams,
“A Z Monitor to Calibrate Higgs Production via Vector Boson Fusion with Rapidity Gaps at the LHC”
Eur. Phys. J. **C26** (2002) 429-440 [arXiv:hep-ph/0207365]
- V. A. Khoze, W. J. Stirling and P. H. Williams,
“Hadronic Radiation Patterns in Vector Boson Fusion Higgs Production”
Accepted for publication in Eur. Phys. J. [arXiv:hep-ph/0307292].

Some of the results have been presented by the author at the following conference and written up in the conference proceedings

- P. H. Williams,
“A Z Monitor to Calibrate Higgs Production via Vector Boson Fusion with Rapidity Gaps at the LHC”
Proceedings of the XXXVIIIth Rencontres de Moriond on QCD and High Energy Hadronic Interactions [arXiv:hep-ph/0304098].

©The copyright of this thesis rests with the author. No quotation from it should be published without prior written consent and information derived from it should be acknowledged.

*They talk a lot of wind and they talk a lot of wind,
they talk a lot of wind and they talk a lot of wind,
they talk a lotta, lotta wind.....ah.*

Mark E. Smith

We want information, information, information.

Number Two

Contents

Acknowledgements	i
Declaration	ii
1 QCD: The Exemplary Quantum Field Theory	1
1.1 The Quark Parton Model and A New Quantum Number	1
1.2 A Confining Force and its Quantum Field Theory	3
1.2.1 The Underlying Local Gauge Symmetry: $SU(3)$	3
1.2.2 The QCD Lagrangian	4
1.3 Making Predictions: Perturbation Theory	7
1.3.1 Going Beyond Leading Order	10
1.3.2 Regularisation of Integrals	11
1.4 Renormalisation	12
1.4.1 The Renormalisation Group and the Running Coupling	14
1.4.2 Confinement and Asymptotic Freedom	17
1.5 Infra-Red Divergences	18
1.5.1 Cancellation of IR Divergences in $R^{e^+e^-}$	18
1.5.2 Infra-Red Safety	26
1.5.3 Infra-Red Safe Definitions of Jets	27
1.6 Initial State Hadrons and Factorisation	29
1.6.1 Factorisation in the Drell-Yan Process	29
1.6.2 DGLAP Evolution of Parton Distribution Functions	31
1.7 Resummation	32
1.7.1 Resummation in an Event Shape Variable: Thrust	32
1.8 Summary	35
2 The Standard Electroweak Model and its Broken Symmetry	37
2.1 The Electroweak Symmetry	38

2.1.1	Higgs Mechanism	38
2.2	Electroweak Feynman Rules	40
2.3	Electroweak Parameter Space	41
3	Higgs Production at Hadron Colliders	47
3.1	Decay Channels	47
3.2	Production Mechanisms	49
3.2.1	Gluon Fusion	49
3.2.2	Vector Boson Fusion	54
3.2.3	Associated Weak Boson Production	55
3.2.4	Associated Top Production	55
3.3	Discovery Prospects at the Tevatron	56
3.4	Discovery Prospects at the LHC	57
3.5	Higgs Production with Rapidity Gaps	59
3.5.1	Diffractive Higgs Production	60
3.5.2	Spectator Effects and the Soft Survival Probability	63
3.5.3	Electroweak Production with Rapidity Gaps	65
4	Higgs Production via Vector Boson Fusion in Rapidity Gap Events and its Calibration	67
4.1	Helicity Amplitude Techniques	68
4.1.1	Colour Decomposition	69
4.1.2	Spinor Product Formalism	71
4.1.3	MadGraph / HELAS	73
4.2	Phase Space Integration	77
4.2.1	Monte Carlo Integration and Importance Sampling	78
4.3	Parton Level Calculation of Higgs, Z and W production	81
4.3.1	Total cross sections	85
4.3.2	Distributions	89
4.3.3	Selection cuts	99
4.3.4	Properties of the QCD $b\bar{b} + 2$ jet Backgrounds	106
4.4	Gap Survival Probabilities	109
4.4.1	Parton Level Gap Survival	109
4.4.2	Soft Survival Probability	115
4.5	LHC Predictions	118
4.5.1	Experimental Issues	120

4.6	Conclusions	121
5	Soft QCD Radiation as a Discriminator in Higgs Searches	124
5.1	Amplitudes for Soft Gluon (and Photon) Emission	126
5.2	Experimental Verification	131
5.3	Hadronic Antenna Patterns for Higgs and $Z + 2$ Jet Production	131
5.3.1	Higgs and Electroweak Z Production	131
5.3.2	QCD Z Production	136
5.4	Numerical Hadronic Antenna Patterns	139
5.4.1	Comparison of Numerical and Analytic Antenna Pat- terns for Signal Processes	140
5.4.2	Numerical Antenna Patterns for Background Processes	145
5.5	Conclusions	151
6	Approximating Higgs Production in Forward Dijet Events	154
6.1	Equivalent Photon Approximation	155
6.2	Testing an Equivalent Gluon Approximation	161
6.2.1	The High Energy Limit	162
6.2.2	Comparing the Results	163
6.3	Extending the Investigation	167
A	Soft Gluon Radiation Probability	169
A.1	Summation of Infrared Divergences in QED	170
A.2	The QCD Result	177
	Bibliography	187

List of Figures

1.1	The gluon self energy	11
1.2	Virtual corrections to $R^{e^+e^-}$	19
1.3	Real corrections to $R^{e^+e^-}$	20
1.4	Drell-Yan production.	30
2.1	Electroweak Standard Model Higgs mass constraints.	45
2.2	Recent W -boson mass measurements.	46
3.1	Standard Model branching ratios for $H \rightarrow$ fermions.	48
3.2	Standard Model branching ratios for $H \rightarrow$ bosons.	49
3.3	Hadronic Higgs production cross sections.	51
3.4	Benchmark hadronic cross sections.	53
3.5	Tevatron Higgs discovery potential.	57
3.6	LHC Higgs discovery potential.	58
4.1	Higgs production via electroweak vector boson fusion.	82
4.2	The three topologies for Zqq production via electroweak vector boson exchanges.	83
4.3	The three topologies for Wqq production via electroweak vector boson exchanges.	83
4.4	QCD background $Z + 2$ jet production processes.	84
4.5	Continuum QCD backgrounds to $qq \rightarrow qq(H, Z)$, $(H, Z) \rightarrow b\bar{b}$	85
4.6	Total cross sections for $(H, Z, W) + 2$ jet production at the LHC.	86
4.7	Ratio between total cross sections of the W and Z electroweak production processes as a function of $p_{T \min}$ of the forward jets.	88
4.8	LHC $qq \rightarrow qqH$ cross section as a function of the Higgs mass.	88
4.9	Jet transverse momentum distribution for $qq \rightarrow qqH$	89
4.10	Parton sampling distribution	90

4.11	Jet rapidity distribution for $qq \rightarrow qqH$ with $p_{T\min} = 40$ GeV and $\eta_1, \eta_2 < 0$	91
4.12	Dijet rapidity difference for $qq \rightarrow qqH$	92
4.13	Contribution to the $\mathcal{O}(\alpha_W^3)$ electroweak $q\bar{q} \rightarrow q\bar{q}H$ that resonates when $m_{jj} \sim m_Z$	92
4.14	Dijet invariant mass for $qq \rightarrow qqH$ showing a double resonance around m_Z and m_W	93
4.15	Jet azimuthal distribution for $qq \rightarrow qqH$	94
4.16	Jet rapidity distribution for electroweak Z production.	95
4.17	Jet azimuthal distribution for electroweak $qq \rightarrow qqZ$	96
4.18	Azimuthal angle distribution of Higgs or electroweak Z from the forward jets.	97
4.19	Higgs and electroweak Z rapidity distribution for $p_{T\min} = 40$ GeV.	98
4.20	Electroweak Z and W rapidities at low jet $p_{T\min}$	99
4.21	Jet rapidity distribution for QCD $Z + 2$ jet production.	100
4.22	Comparison of dijet rapidity differences for electroweak and QCD Z production.	101
4.23	Jet azimuthal distribution for $qq \rightarrow qqZ$ (QCD).	102
4.24	Transverse momentum of b jets.	103
4.25	Parton level LHC cross sections for Higgs production processes after application of cuts.	104
4.26	Parton level LHC cross Sections for Z production processes after application of cuts.	105
4.27	Hard subprocess cross sections for QCD continuum $b\bar{b} + 2$ jet backgrounds.	108
4.28	Screening of QCD dijet + $b\bar{b}$ production via gluon exchange.	110
4.29	Screening of QCD dijet + Z production via quark exchange.	114
4.30	Hadron level cross sections for the LHC.	119
5.1	Soft gluon emission from an initial state quark.	127
5.2	Soft gluon emission from an internal quark.	128
5.3	Diagrams for $q\bar{q} \rightarrow Wg$	130
5.4	LPHD prediction and data compared for $W +$ jet events at DØ.	132
5.5	Antenna pattern for $qq' \rightarrow qq'H$; $H \rightarrow b\bar{b}$ with $\eta_{\text{jet}} = 3.5$	135
5.6	The point $(\eta_g, \phi_g) = (0, \pi/2)$ in $\mathcal{R}(qq' \rightarrow qq')$ as one varies η_{jet}	136

5.7	Antenna pattern for $qq' \rightarrow qq'Z$ (QCD); $Z \rightarrow b\bar{b}$ with $\eta_{\text{jet}} = 3.5$.	137
5.8	The point $(\eta_g, \phi_g) = (0, 0)$ in $\mathcal{O}(\alpha_s^2)$ $qq' \rightarrow qq'$ as the rapidity of the forward jets is varied.	138
5.9	Ratio of Higgs to QCD Z production antenna patterns.	139
5.10	Ratio of numerical $qq' \rightarrow qq'H$ to analytic $qq' \rightarrow qq'$ antenna patterns with $ \eta_{\text{jet}} = 2$ and $k_{Tg} = 1$ GeV.	141
5.11	Ratio of numerical $qq' \rightarrow qq'H$ to analytic $qq' \rightarrow qq'$ antenna patterns with $ \eta_{\text{jet}} = 2$ and $k_{Tg} = 10^{-5}$ GeV.	142
5.12	Ratio of numerical EW $qq' \rightarrow qq'Z$ to analytic $qq' \rightarrow qq'$ antenna patterns with $ \eta_{\text{jet}} = 2$ and $k_{Tg} = 10^{-5}$ GeV.	143
5.13	Ratio of numerical EW $qq' \rightarrow qq'Z$ to analytic $qq' \rightarrow qq'$ antenna patterns with $ \eta_{\text{jet}} = 4$ and $k_{Tg} = 10^{-5}$ GeV.	143
5.14	Ratio of numerical QCD $qq' \rightarrow qq'Z$ to analytic $qq' \rightarrow qq'$ antenna patterns with $ \eta_{\text{jet}} = 2$ and $k_{Tg} = 10^{-5}$ GeV.	144
5.15	Ratio of numerical QCD $qq' \rightarrow qq'Z$ to analytic $qq' \rightarrow qq'$ antenna patterns with $ \eta_{\text{jet}} = 4$ and $k_{Tg} = 10^{-5}$ GeV.	145
5.16	Numerical antenna pattern for $qq' \rightarrow qq'b\bar{b}$ with $ \eta_{\text{jet}} = 4$ and $k_{Tg} = 1$ GeV.	146
5.17	Numerical antenna pattern for $qg \rightarrow qgb\bar{b}$ with $ \eta_{\text{jet}} = 4$ and $k_{Tg} = 1$ GeV.	147
5.18	Numerical antenna pattern for $gg \rightarrow ggb\bar{b}$ with $ \eta_{\text{jet}} = 4$ and $k_{Tg} = 1$ GeV.	147
5.19	Numerical antenna pattern for $q\bar{q} \rightarrow ggb\bar{b}$ with $ \eta_{\text{jet}} = 4$ and $k_{Tg} = 1$ GeV.	148
5.20	Numerical antenna pattern for $gg \rightarrow q\bar{q}b\bar{b}$ with $ \eta_{\text{jet}} = 4$ and $k_{Tg} = 1$ GeV.	148
5.21	Ratio of antennas for $qg \rightarrow qgb\bar{b}$ and $qq' \rightarrow qq'b\bar{b}$	149
5.22	Analytic antenna pattern for $qg \rightarrow qgZ$; $Z \rightarrow b\bar{b}$	150
5.23	Ratio of numerical $qq' \rightarrow qq'H$; $H \rightarrow b\bar{b}$ to numerical $qq' \rightarrow qq'b\bar{b}$ with $ \eta_{\text{jet}} = 4$ and $k_{Tg} = 1$ GeV.	151
5.24	Ratio of numerical QCD $qq' \rightarrow qq'Z$; $Z \rightarrow b\bar{b}$ to numerical $qq' \rightarrow qq'b\bar{b}$ with $ \eta_{\text{jet}} = 4$ and $k_{Tg} = 1$ GeV.	152
5.25	Slice in $\eta_g = 0$ of Fig. 5.24 as the rapidity of the forward jets is varied.	152
6.1	'Nearly' on-shell gluon approximation	155

6.2	High energy electron scattering.	155
6.3	Higgs plus two jet production in the high energy limit.	164
6.4	Ratio of EGA with exact gluon fusion Higgs production.	165
6.5	Approximate and exact cross sections for gluon fusion Higgs production at parton level.	166
6.6	Approximate and exact cross sections for gluon fusion Higgs production at hadron level (qq -induced only).	167
A.1	Soft real and virtual photons (left) emitted from an arbitrary hard process (right).	170
A.2	The outgoing electron line of Fig. A.1.	171

List of Tables

1.1	The Feynman rules of QCD.	9
2.1	Feynman rules for electroweak lepton-vector boson interactions.	39
2.2	Feynman rules for electroweak vector boson self-interactions.	42
2.3	Feynman rules for Higgs interactions	43
3.1	Dominant hadronic Higgs production modes.	50
3.2	Diffractive Higgs production.	61
3.3	Diffractive Higgs cross sections predictions for $m_H = 120$ GeV in fb.	65
4.1	Loss of $qq \rightarrow qqH$ LHC cross section with $m_H = 115$ GeV when applying selection cuts.	103

Chapter 1

QCD: The Exemplary

Quantum Field Theory

Of all established elementary forces in Nature, the one describing the structure of hadrons has proved to be the most reticent in revealing its secrets. It is no coincidence that this force possesses attributes that set it apart from all other natural processes.

During the 1960's, deeply inelastic electron-proton scattering experiments conducted at the Stanford Linear Accelerator Centre established that hadrons had substructure and uncovered the two basic facts of the perverse physical phenomenon governing their constituents, namely *asymptotic freedom* / *confinement* and the quantum number *colour*.

1.1 The Quark Parton Model and A New Quantum Number

The plethora of distinct hadrons discovered and classified over the previous decades had led many to the view that some type of substructure was in-



evitable. Gell-Mann [1] and Zweig [2] had proposed a plausible paradigm: the Quark Parton Model (QPM).

Hadrons would thus be composed of fractionally charged, fermionic (spin 1/2) constituents - the *quarks*. The correct spin/parity nature of hadrons can be reproduced if mesons are composed of a quark and its antiparticle and baryons of three quarks.

Suggestively, these constructions lead to a contradiction with the Fermi-Dirac statistics of the postulated constituents. For example, in the QPM the $\Delta^{++}(J = 3/2)$ baryon is composed of three quarks of charge 2/3. In combining three spin-1/2 particles to make a spin-3/2 product using the group theory relations in Clebsch-Gordan tables we must have all constituent spins parallel thus

$$\Delta^{++} = |u^\uparrow u^\uparrow u^\uparrow\rangle. \quad (1.1)$$

This combination is clearly symmetric under the interchange of two quarks, implying Bose-Einstein statistics for the Δ^{++} . The paradox is resolved by introducing a *new quantum number* carried by hadronic constituents such that the antisymmetry under exchange is restored. This is the *colour charge* [3]. There must exist at least three independent values of the charge in order for the antisymmetry of baryons to be restored. Contrast this with the single-valued quantum number of electric charge - this is truly a new natural phenomenon.

We supplement this new degree of freedom with the requirement that observed hadrons must be colourless. Experimentally, by measuring the ratio

$$R^{e^+e^-} \equiv \frac{\sigma(e^+e^- \rightarrow \text{hadrons})}{\sigma(e^+e^- \rightarrow \mu^+\mu^-)} \quad (1.2)$$

the number of colours is found to be exactly three [4, 5]. Therefore mesons exist in the combination $|q_\alpha q^\alpha\rangle$ and baryons $|\varepsilon^{\alpha\beta\gamma} q_\alpha q_\beta q_\gamma\rangle$ where $\alpha, \beta, \gamma = 1, 2, 3$ labels the colour quantum number and $\varepsilon^{\alpha\beta\gamma}$ is the totally antisymmetric tensor.

1.2 A Confining Force and its Quantum Field Theory

If the Quark Parton Model is to be taken seriously we must immediately explain *why* only colourless hadrons are observed in nature and not their fractionally charged constituents. This will lead us to the defining aspect of the strong force; the notions of confinement and asymptotic freedom.

1.2.1 The Underlying Local Gauge Symmetry: $SU(3)$

We now require our colour quantum number to display *local gauge symmetry* under transformations of the *non-Abelian* group $SU(3)$. This group is chosen because quarks are observed to be colour triplets. Other plausible candidate groups would be $SO(3)$ or $U(3)$. $SO(3)$ is disfavoured as this makes no distinction between colour and anticolour, thereby allowing fractionally charged qq combinations, which are not observed. $U(3)$ is also inadequate because of the existence of a colour singlet “photon” that would mediate long distance interactions between colour singlet hadrons. We are thus left with $SU(3)$. $SU(3)$ is the Lie group of 3×3 unitary matrices with determinant one. Any element of the group, U , can be constructed given eight parameters, $\Theta_a(x)$ thus

$$U(x) = \exp\{iT \cdot \Theta(x)\}. \quad (1.3)$$

The T^a are generators of the group $SU(3)$ and obey the commutation relation

$$[T^a, T^b] = if^{abc}T_c, \quad (1.4)$$

which defines the Lie algebra of the group. The f^{abc} are called the *structure constants* of QCD and are real and antisymmetric. The generators in the conventional normalisation give the following representation Casimir's or *QCD colour factors*, T_R , C_F and C_A

$$\text{Tr}(T^a T^b) = T_R \delta^{ab}; \quad T_R = 1/2 \quad (1.5)$$

$$\sum_a T_{\alpha\beta}^a T_{\beta\gamma}^a = C_F \delta_{\alpha\gamma}; \quad C_F = 4/3 \quad (1.6)$$

$$\sum_{a,b} f^{abc} f^{abd} = C_A \delta^{cd}; \quad C_A = 3, \quad (1.7)$$

with $a \dots d = 1 \dots 8$ and $\alpha, \beta, \gamma = 1, 2, 3$.

1.2.2 The QCD Lagrangian

The partition of energy in a relativistic field can be completely described by specifying a Lagrangian density that obeys Hamilton's principle of least action. The equations of motion for the field can then be obtained from the Euler-Lagrange equations. We split the QCD Lagrangian thus

$$\mathcal{L}_{\text{QCD}} = \mathcal{L}_{\text{classical}} + \mathcal{L}_{\text{gauge}} + \mathcal{L}_{\text{ghost}} \quad (1.8)$$

and consider each term in order.

The Classical Part

The classical Lagrangian density is constructed in direct analogy to QED. Firstly we consider the dynamical and mass properties of the quark fields

$$\mathcal{L}_{\text{quark}} = \sum_q \bar{\psi}_q^i (\not{D} - m_q)_{ij} \psi_q^j. \quad (1.9)$$

They transform in the fundamental representation of our chosen gauge group $SU(3)$

$$\psi_q^i(x) \rightarrow U^{ij}(x) \psi_q^j(x) = \tilde{\psi}_q^i(x). \quad (1.10)$$

The Lagrangian is invariant under the transformation, thus the covariant derivative is defined

$$(\mathcal{D}^\mu)_{ij} \equiv \partial^\mu \delta_{ij} + ig_s A_a^\mu T_a^{ij} \quad (1.11)$$

where g_s is the strong coupling and the A_a^μ are eight vector fields that guarantee the local gauge invariance by propagating the strong interaction. They are called *gluons*. The covariant derivative satisfies the following commutation relation

$$[\mathcal{D}^\mu, \mathcal{D}^\nu] = -ig_s G_a^{\mu\nu} T_a \quad (1.12)$$

where $G_a^{\mu\nu}$ is the gluon field strength tensor

$$G_a^{\mu\nu} \equiv \partial^\mu A_a^\nu - \partial^\nu A_a^\mu + g_s f_{abc} A_b^\mu A_c^\nu. \quad (1.13)$$

At this point one should note the final term in $G_a^{\mu\nu}$. It arises from the non-Abelian nature of the gauge group and implies that the vector fields undergo *self interactions* and are themselves colour charged. This feature sets it apart from QED and asymptotic freedom derives from it.

To complete the classical Lagrangian we must add a term describing the

free propagation of the gluons à la QED

$$\mathcal{L}_{\text{gluon}} = -\frac{1}{4}G_{\mu\nu}^a G_a^{\mu\nu}. \quad (1.14)$$

We are unable to add a mass term and keep gauge invariance therefore the gluons are massless.

The Gauge Part

When we attempt to canonically quantise the theory, we hit a snag. The gluon fields A_a^μ are classical quantities and their canonical momentum vanishes. The source of this ambiguity is the fact that we are trying to describe a spin-1 massless particle that therefore has two physical degrees of freedom (polarisations) in terms of a Lorentz four vector. We therefore need two extra constraints on the gluon fields. A choice for one of these is

$$\partial_\mu A_a^\mu = 0, \quad (1.15)$$

the *Lorentz condition*. Translating this to the Lagrangian we see that we now have a *gauge fixing* term

$$\mathcal{L}_{\text{gauge}} = -\frac{1}{2\xi}(\partial_\mu A_a^\mu)^2. \quad (1.16)$$

The Lagrangian is now no longer explicitly gauge invariant, however any physical prediction is independent of the variable ξ and is gauge invariant. We are thus free to choose any value for ξ . Common choices are the Landau gauge $\xi = 0$, the Feynman gauge $\xi = 1$ and the unitary gauge $\xi \rightarrow \infty$.

The Ghost Part

We still have one unphysical degree of freedom for the gluon fields. It leads to unphysical contributions to predictions that we may arrange to cancel by introducing extra, unphysical fields. These must be anticommuting (fermionic) scalar fields living in the adjoint representation of $SU(3)$, coupling only to gluons. They are called *Faddeev-Popov ghosts* and have the term

$$\mathcal{L}_{\text{ghost}} = -\bar{\eta}^a (\partial_\mu \mathcal{D}_{ab}^\mu) \eta^b. \quad (1.17)$$

Expanding the covariant derivative in terms of the gauge fields and structure constants gives

$$\mathcal{L}_{\text{ghost}} = -\bar{\eta}^a (\partial^2 \delta_{ab} + g_s \partial_\mu A_c^\mu f_{abc}) \eta^b. \quad (1.18)$$

It should be noted that if we choose a non-covariant gauge, the need for these fictitious fields can be removed.

1.3 Making Predictions: Perturbation Theory

Leaving aside the issue of QCD bound states such as hadrons, we wish to make predictions concerning the interactions of strongly interacting particles at high energy scattering experiments. This is done by using the LSZ reduction formula to relate an experimental quantity such as the cross section to the scattering matrix via Feynman amplitudes. The *S-matrix* relates two states in which particles are in principle infinitely spatially separated, these are the initial and the final state, which are in principle infinitely temporally separated. However, as with most interacting quantum field theories,

QCD scattering amplitudes are not exactly solvable. Therefore we treat the interaction terms in the Lagrangian as perturbations of the free theory or vacuum solution. This is done by expanding the interaction terms as powers in the coupling constant, g_s . Of course, this may only be done if the coupling is small - a requirement that in quantitative form puts strict limits on the validity of perturbative QCD.

The Feynman Rules of QCD

Thus divided we use Wick's theorem to write a Feynman amplitude, $i\mathcal{M}$, in terms of parts derived from the exactly solvable free theory (free particle *propagators*) and parts derived from the perturbative interaction terms (interaction *vertices*). The mathematical terms representing field propagators and allowed vertices and their traditional diagrammatic pseudonyms are listed in Table 1.1. Colour indices for quarks are labelled i, j and take the values 1, 2, 3, being in the fundamental representation. Those for ghosts and gluons are denoted $a \dots d$ and, as they are in the adjoint representation, take values 1 \dots 8. Greek script denotes the Lorentz indices.

The amplitude is constructed by first writing down all topologically distinct diagrams of the required order in the coupling for the process being considered. Then one uses the Feynman rules to write a mathematical expression for each diagram taking care to preserve the correct order of the Dirac matrices (ensured by following fermion lines 'upstream'). To complete the amplitude one must then apply the following prescription.

- Multiply by -1 for each antifermion connecting the initial and final state.
- Multiply by -1 for each fermion or ghost loop.

Incoming Particles

$$u(p) = \text{diagram: fermion line with arrow pointing right, momentum } p \text{ above}$$

$$\bar{v}(p) = \text{diagram: fermion line with arrow pointing left, momentum } p \text{ above}$$

$$\varepsilon_\mu(p) = \text{diagram: gluon line with momentum } p \text{ above}$$

Outgoing Particles

$$\bar{u}(p) = \text{diagram: fermion line with arrow pointing left, momentum } p \text{ above}$$

$$v(p) = \text{diagram: fermion line with arrow pointing right, momentum } p \text{ above}$$

$$\varepsilon_\mu^*(p) = \text{diagram: gluon line with momentum } p \text{ above}$$

Propagators

$$\frac{i\delta_{ij}(\not{p} + m)}{p^2 - m^2} = \text{diagram: fermion line with arrow pointing right, momentum } p \text{ above}$$

$$\frac{-i\delta_{ab}}{k^2} \left(g^{\mu\nu} - (1 - \xi) \frac{k^\mu k^\nu}{k^2} \right) = \text{diagram: gluon line with momentum } k \text{ above}$$

$$\frac{i\delta_{ab}}{k^2} = \text{diagram: ghost line with momentum } k \text{ above}$$

Vertices

$$ig_s \gamma^\mu T_{ij}^a = \text{diagram: quark-gluon vertex with incoming quark } i, \text{ outgoing quark } j, \text{ and outgoing gluon } a, \mu$$

$$g_s f^{abc} [(k_1 - k_2)^\rho g^{\mu\nu} + (k_2 - k_3)^\mu g^{\nu\rho} + (k_3 - k_1)^\nu g^{\mu\rho}] = \text{diagram: three-gluon vertex with momenta } k_1, a, \mu; k_2, b, \nu; k_3, c, \rho$$

$$g_s f^{abc} k^\mu = \text{diagram: ghost-gluon vertex with incoming ghost } b, \text{ outgoing ghost } c, \text{ and outgoing gluon } a, \mu$$

$$-ig_s^2 [f^{abe} f^{cde} (g^{\mu\rho} g^{\nu\sigma} - g^{\mu\sigma} g^{\nu\rho}) + f^{ace} f^{bde} (g^{\mu\nu} g^{\rho\sigma} - g^{\mu\sigma} g^{\nu\rho}) + f^{ade} f^{bce} (g^{\mu\nu} g^{\rho\sigma} - g^{\mu\rho} g^{\nu\sigma})] = \text{diagram: four-gluon vertex with momenta } a, \mu; b, \nu; c, \rho; d, \sigma$$

Table 1.1: The Feynman rules of QCD.

- Impose momentum conservation at each vertex.
- Integrate over any unconstrained momenta appearing in closed loops with the measure $\int \frac{d^4 p}{(2\pi)^4}$
- Multiply by a symmetry factor to allow for permutations of fields

In Table 1.1 we have neglected the *Feynman prescription* where $+i\epsilon$ is added to the denominators in the propagators. These serve as a prompt to *Wick rotate* the integral to Euclidean space to perform its evaluation. To proceed, one now has a choice. One method is to square the amplitude and use spin sum relations of the Dirac spinors $u(p)$ and polarisation vectors $\varepsilon_\mu(p)$ and properties of the Dirac matrices to reduce the expressions, this is called the *trace technique*. The other method is to consider each term where external particles have different spins separately, square these terms and sum the spins at the end of the calculation, this is called the *helicity method*. The details of the latter will be explained more fully in Chapter 4

1.3.1 Going Beyond Leading Order

Present day experiments test the accuracy of theory in such a way that calculations at leading order in the perturbative coupling are not sufficient. Indeed recently there has been a need to go beyond next-to-leading order in the calculations of some processes. When one does this, formally infinite quantities begin to appear. To understand the calculation one needs to reformulate or reinterpret the divergent expressions.

We illustrate these considerations by way of a simple example - the one-loop gluon self energy (Fig. 1.1). In this process it is the unconstrained momentum flowing round the loop that is the source of divergences. Applying

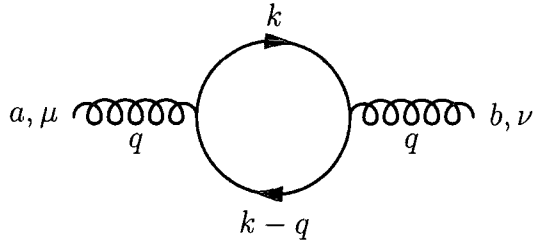


Figure 1.1: The gluon self energy

the Feynman rules one arrives at the expression

$$i\Pi_{ab}^{\mu\nu} = -g_s^2 t_{ij}^a t_{ji}^b \int \frac{d^4 k}{(2\pi)^4} \frac{\text{Tr}[\gamma^\mu(\not{k} + m_q)\gamma^\nu(\not{k} - \not{q} + m_q)]}{(k^2 - m_q^2)[(k - q)^2 - m_q^2]} \xrightarrow{m_q \rightarrow 0} \int \frac{d^4 k}{k^2}. \quad (1.19)$$

This displays two types of divergence

1. *Infra-Red divergence*: Occurs when the mass of the particle involved (here m_q) becomes zero, for this reason they are also called *mass singularities*. Then the k -integral diverges in the $k \rightarrow 0$ limit. These divergences display the amazing property that they formally cancel between diagrams of different types. This will be further explained in Section 1.5 and generalised in Appendix A.
2. *Ultra-Violet divergence*: Occurs in the k -integral in the $k \rightarrow \infty$ limit. This is dealt with by *regularising* the integral and applying the method of *renormalisation*. Renormalisability of a quantum field theory is a crucial property without which all predictive power would be lost. We shall explore this issue first.

1.3.2 Regularisation of Integrals

The aim of regularisation is to quantitatively separate the UV divergent part of a Feynman integral from its finite parts. There are three popular ways

of doing this, *cut off*, *mass* and *dimensional* regularisation. We describe the latter method as it is computationally the most useful.

Feynman integrals are reinterpreted as being analytic functions of space-time dimensionality D . We then notice that the integrals converge when $D < 4$. Thus we calculate our expression in a dimension infinitesimally less than four - usually written $D = 4 - 2\epsilon$, then we take the limit $\epsilon \rightarrow 0$ in the end result. When this procedure is followed, divergences are quantified as poles in ϵ . The method has the advantage of preserving Lorentz and gauge invariance and also unitarity.

There are some subtleties associated with dimensional regularisation, notably all integration measures become D -dimensional as do the Dirac matrices. Also the dimensionality of the Lagrangian is altered. One corrects for this by introducing an arbitrary *regularisation scale*, μ , which then appears to preserve the dimensionlessness of the coupling, $g_s \rightarrow \mu^\epsilon g_s$.

Applying this to the gluon self energy and performing the sum over colours one obtains the result

$$\Pi_{ab}^{\mu\nu} = \frac{4}{3} T_R \delta_{ab} (-q^2 g^{\mu\nu} + q^\mu q^\nu) \left(\frac{\mu^\epsilon g_s}{4\pi} \right)^2 \left[\frac{1}{\epsilon} - \gamma_E + \ln(4\pi) - \ln(-q^2/\mu^2) + \frac{5}{3} + \mathcal{O}(\epsilon) \right] \quad (1.20)$$

where $\gamma_E = 0.57722\dots$ is the Euler-Mascheroni constant.

1.4 Renormalisation

Having isolated the UV divergent nature of integrals in the form of poles in ϵ we can remove them to leave a finite result. We do this by reinterpreting the parameters with which we work. The philosophy is that the Feynman rules and diagrams derived from them are expressed in terms of *bare param-*

eters (fields, couplings and masses) that are not physically observable. We therefore have the freedom to rescale them and reconstruct the Lagrangian in terms of observed *physical parameters*. For example, if the bare parameter is represented with a zero subscript, the quark fields become $\psi_{0q}^i \equiv Z_\psi^{1/2} \psi_q^i$ and the coupling $g_{0s} \equiv Z_g g_s$ where the *renormalised* parameters are prepended by renormalisation constants, Z . These constants are constructed to absorb the UV divergences and are therefore formally infinite. If this process can be carried out order by order in the coupling, then the field theory one is dealing with is said to be *renormalisable*. Technically, we introduce counterterms into the Lagrangian to construct the constants. Provided we now consider the Feynman rules to be expressed in terms of the renormalised parameters the constants, Z , do not enter physically observable quantities. This is just because we have rescaled the parameters.

The practical prescription for what to absorb is not uniquely defined and is subject to choice. A particular choice is called a *renormalisation scheme*. One popular choice is the *Minimal Subtraction* (MS) scheme where one simply absorbs the ϵ pole. Another commonly used scheme is called *Modified Minimal Subtraction* ($\overline{\text{MS}}$) where one absorbs the combination

$$(4\pi)^\epsilon \frac{\exp(-\epsilon\gamma_E)}{\epsilon} = \frac{1}{\epsilon} + \ln(4\pi) - \gamma_E + \mathcal{O}(\epsilon) \quad (1.21)$$

which often appears in calculations, such as our example of the gluon self energy (1.20).

1.4.1 The Renormalisation Group and the Running Coupling

In calculating our physical process, we have introduced an ambiguity and a new parameter - the renormalisation scheme and the regularisation scale, μ .

Unfortunately, the renormalisation scheme independence only reappears for exact results - those which are calculated to all orders in perturbation theory. The act of truncation of the full perturbative series necessitates scheme dependence by disturbing cancellations between terms of different orders, it is therefore unavoidable.

Let us now turn to regularisation scale dependence. Any physical quantity, \mathcal{R} , now depends not only on the couplings and masses involved in it, but also on μ . More generally, the couplings and masses themselves will also acquire μ dependence. If \mathcal{R} is dimensionless and measured at a scale Q , it will have the form

$$\mathcal{R} = \mathcal{R}(Q^2/\mu^2, \alpha_s(\mu^2), m_i(\mu^2)), \quad (1.22)$$

where we have rescaled the coupling

$$\alpha_s \equiv \frac{g_s^2}{4\pi}. \quad (1.23)$$

For our theory to be meaningful, this dependence on μ must be spurious, in other words \mathcal{R} must remain invariant under a change of scale $\mu \rightarrow \mu'$. We

can cast this requirement thus

$$\mu^2 \frac{d\mathcal{R}(Q^2/\mu^2, \alpha_s(\mu^2), m_i(\mu^2))}{d\mu^2} = 0$$

$$\left[\beta(\mu^2) \frac{\partial}{\partial \alpha_s} - \gamma_{m_i}(\mu^2) \frac{\partial}{\partial m_i} + \mu^2 \frac{\partial}{\partial \mu^2} \right] \mathcal{R}(Q^2/\mu^2, \alpha_s(\mu^2), m_i(\mu^2)) = 0, \quad (1.24)$$

which defines the β -function and the *anomalous dimension*, γ_{m_i} thus

$$\beta(\mu^2) = \mu^2 \frac{\partial \alpha_s}{\partial \mu^2}, \quad \gamma_{m_i} = -\frac{\mu^2}{m_i} \frac{\partial m_i}{\partial \mu^2}. \quad (1.25)$$

These are the *Renormalisation Group Equations* and quantify the phenomenon of *running parameters* - here the coupling and the masses are shown to depend upon the scale at which one measures them.

Rewriting the coupling RGE as an integral equation

$$\ln \left(\frac{Q^2}{\mu^2} \right) = \int_{\alpha_s(\mu)}^{\alpha_s(Q)} \frac{d\alpha}{\beta(\alpha)} \quad (1.26)$$

one can see that it may be solved by writing the β -function as a series in α_s ,

$$\beta(\alpha_s) = -\alpha_s^2 (\beta_0 + \alpha_s \beta_1 + \dots). \quad (1.27)$$

The coefficients may be calculated according to the QCD Feynman rules obtaining

$$\beta_0 = \frac{1}{4\pi} \left(11 - \frac{2}{3} N_f \right), \quad \beta_1 = \frac{1}{16\pi^2} \left(102 - \frac{38}{3} N_f \right), \quad (1.28)$$

where N_f is the number of active flavours. Solving Eq. (1.26) to first order leads to

$$\alpha_s(Q^2) = \frac{\alpha_s(\mu^2)}{1 + \beta_0 \ln(Q^2/\mu^2) \alpha_s(\mu^2)}. \quad (1.29)$$

Rearranging this, the μ independence becomes obvious

$$\frac{1}{\alpha_s(Q^2)} - \beta_0 \ln(Q^2) = \frac{1}{\alpha_s(\mu^2)} - \beta_0 \ln(\mu^2) \equiv -\beta_0 \ln(\Lambda). \quad (1.30)$$

Λ represents a new scale, one where the coupling becomes large and perturbation theory is no longer valid. It plays the rôle of gatekeeper between the perturbative and non-perturbative regimes of QCD. In the $\overline{\text{MS}}$ scheme with five active flavours we find that $\Lambda \sim 208 \text{ MeV}$.

Scale Dependence

We have seen how observables depend on the scale μ and how this leads to running couplings. How does this manifest itself in a fixed order calculation? Consider the perturbative expansion of an observable, in general both the coupling and its perturbative coefficients are scale dependent

$$\mathcal{R}(\alpha_s(\mu^2), Q^2/\mu^2) = \sum_{n=1}^{\infty} r_n(Q^2/\mu^2) \alpha_s(\mu^2)^n. \quad (1.31)$$

If we truncate the series at N terms, its scale dependence is

$$\frac{d}{d \ln \mu^2} \sum_{n=1}^N r_n(Q^2/\mu^2) \alpha_s(\mu^2)^n = -\frac{d}{d \ln \mu^2} \sum_{n=N+1}^{\infty} r_n(Q^2/\mu^2) \alpha_s(\mu^2)^n \sim \mathcal{O}(\alpha_s^{N+1}), \quad (1.32)$$

where we have used the fact that the full series is independent of μ . This makes plain that the scale dependence of our fixed order calculation decreases as we add more terms. We will see examples of this as the thesis progresses.

1.4.2 Confinement and Asymptotic Freedom

The behaviour of the coupling outlined above is responsible for the anti-intuitive nature of QCD.

- **Confinement:** When the energy scale decreases, the coupling increases. This signifies the limit of applicability of our most useful mathematical paradigm - perturbation theory. We cannot expand observables in a parameter that is large. At first this may seem bad news, our best method fails, however one should realise that this fact makes possible the existence of hadrons! QCD is the only natural construct that could explain such stable composite entities. The *confining* nature of QCD at low energies cannot be proved or explored using perturbative techniques. This has led to the development of *lattice* methods whereby attempts are made to fully solve the action numerically. This is an interesting and increasingly predictive method.
- **Asymptotic Freedom:** When the energy increases, the coupling decreases. This is what enables us to do perturbation theory. The correct degrees of freedom to describe a high energy collision are the perturbative constituents of hadrons - quark and gluon fields.

It is the sign of the first β -function coefficient that produces these two effects. In QED $\beta_0 < 0$ leading to a screening, long range force. In QCD $\beta_0 > 0$ produces an anti-screening, short range force. The extra (with respect to QED) positive signed contributing terms originate from the fact that gluons have colour and thus self interact. This is in turn a consequence of the non-Abelian nature of the underlying symmetry governing the colour quantum number.

1.5 Infra-Red Divergences

When we considered the self energy of the gluon (Eq. (1.20) and Fig. 1.1) we saw that it displays an IR divergence when $m_q \rightarrow 0$. More generally, IR singularities can be classified into two types:

- **Soft Divergences:** When a massless on-shell particle emits a massless low momentum ($k \sim 0$) particle and remains on-shell. Then integration over k yields a divergence originating from the region where $k \rightarrow 0$.
- **Collinear Divergences:** When an on-shell particle with momentum p emits a massless particle with momentum k and remains on-shell. Integration over k yields a divergence originating from the region where $k \rightarrow p$.

These divergences have the astounding property that they exactly cancel between terms of different order. We show this by way of an example.

1.5.1 Cancellation of IR Divergences in $R^{e^+e^-}$

The ratio of the total hadronic to total muonic cross sections in e^+e^- annihilation (Eq. (1.2)) is an ideal quantity in which to demonstrate IR divergence cancellation. $\sigma(e^+e^- \rightarrow \mu^+\mu^-)$ is a well known quantity determined from QED. The total hadronic cross section is calculable perturbatively because we are able to separate the non-perturbative process of hadron formation from the perturbative process of parton creation. This separation is called *factorisation* and allows us to consider short distance physics without interference from long distance physics. This concept will be explained fully in Section 1.6. Factorisation justifies the statement that the total hadronic cross section is equal to the perturbative cross section $\sigma(e^+e^- \rightarrow q\bar{q} + X)$.

At leading order (and assuming we excite five quark flavours) the ratio of the total hadronic to total muonic cross sections in e^+e^- annihilation (Eq. (1.2)) is found to be

$$R^{e^+e^-} = N_c \sum_q e_q^2 = \frac{11}{3} \simeq 3.67. \quad (1.33)$$

The experimentally determined value at $\sqrt{s} = 34$ GeV is $R^{e^+e^-} = 3.9$. Corrections due to virtual Z exchange are small at this energy. One must conclude that higher order corrections are needed in order to compare theory with experiment. Working to $\mathcal{O}(\alpha_s)$ we see that there are two contributions to the matrix element

$$|\mathcal{M}_{qq}\rangle = |\mathcal{M}_{qq}^{(0)}\rangle + |\mathcal{M}_{qq}^{(1)}\rangle + \mathcal{O}(\alpha_s^2) \quad (1.34)$$

and

$$|\mathcal{M}_{qqg}\rangle = |\mathcal{M}_{qqg}^{(0)}\rangle + \mathcal{O}(\alpha_s^2) \quad (1.35)$$

where $|\mathcal{M}_{qq}^{(0)}\rangle$ indicates the leading order (LO) matrix element for $e^+e^- \rightarrow q\bar{q}$, $|\mathcal{M}_{qq}^{(1)}\rangle$ indicates the next-to-leading order (NLO) virtual corrections to $e^+e^- \rightarrow q\bar{q}$ (Fig. 1.2) and $|\mathcal{M}_{qqg}^{(0)}\rangle$ indicates the leading order real emission process $e^+e^- \rightarrow q\bar{q}g$ (Fig. 1.3).

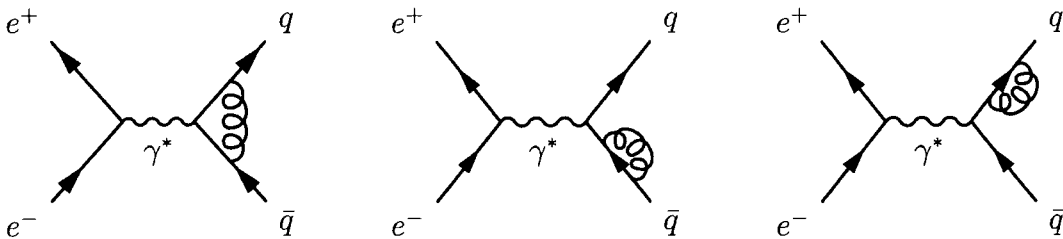


Figure 1.2: Virtual corrections to $R^{e^+e^-}$.

As usual we may now write the cross section as an integral over n -body

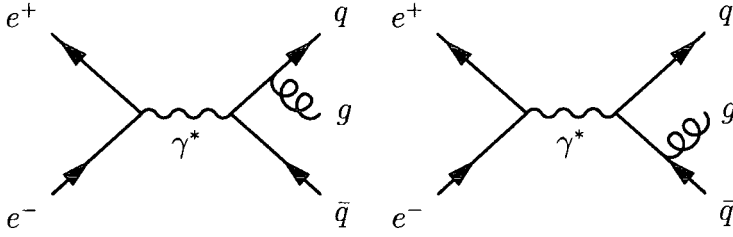


Figure 1.3: Real corrections to $R^{e^+e^-}$.

phase space

$$\sigma_{q\bar{q}+X} = \mathcal{F} \int \sum_{\substack{\text{spins} \\ \text{colours}}} \langle \mathcal{M}_{q\bar{q}+X} | \mathcal{M}_{q\bar{q}+X} \rangle d\Pi_n \quad (1.36)$$

where \mathcal{F} denotes the flux factor and $d\Pi_n$ represents differential n -body phase space. Using Eqs. (1.34) we may expand the $q\bar{q}$ contribution to the cross section in the coupling

$$\sigma_{q\bar{q}} = \sigma_{q\bar{q}}^{(0)} + \sigma_{q\bar{q}}^{(1)} + \mathcal{O}(\alpha_s^2) \quad (1.37)$$

where

$$\sigma_{q\bar{q}}^{(0)} = \mathcal{F} \int \sum_{\substack{\text{spins} \\ \text{colours}}} \langle \mathcal{M}_{q\bar{q}}^{(0)} | \mathcal{M}_{q\bar{q}}^{(0)} \rangle d\Pi_2 \quad (1.38)$$

and

$$\begin{aligned} \sigma_{q\bar{q}}^{(1)} &= \mathcal{F} \int \sum_{\substack{\text{spins} \\ \text{colours}}} \left[\langle \mathcal{M}_{q\bar{q}}^{(0)} | \mathcal{M}_{q\bar{q}}^{(1)} \rangle + \langle \mathcal{M}_{q\bar{q}}^{(1)} | \mathcal{M}_{q\bar{q}}^{(0)} \rangle \right] d\Pi_2 \\ &= \mathcal{F} \int \sum_{\substack{\text{spins} \\ \text{colours}}} 2\Re \langle \mathcal{M}_{q\bar{q}}^{(0)} | \mathcal{M}_{q\bar{q}}^{(1)} \rangle d\Pi_2. \end{aligned} \quad (1.39)$$

Similarly we use Eq. (1.35) to write the $q\bar{q}g$ contribution

$$\sigma_{q\bar{q}g} = \sigma_{q\bar{q}g}^{(0)} + \mathcal{O}(\alpha_s^2) \quad (1.40)$$

where

$$\sigma_{q\bar{q}g}^{(0)} = \mathcal{F} \int \sum_{\substack{\text{spins} \\ \text{colours}}} \langle \mathcal{M}_{q\bar{q}g}^{(0)} | \mathcal{M}_{q\bar{q}g}^{(0)} \rangle d\Pi_3. \quad (1.41)$$

A calculation of $\sigma_{q\bar{q}}^{(0)}$ using conventional dimensional regularisation with massless quarks gives us the leading order result presented at the start of this section, Eq. (1.33).

The NLO Virtual Correction

Our first $\mathcal{O}(\alpha_s)$ term is $\sigma_{q\bar{q}}^{(1)}$, Eq. (1.39). Applying the Feynman rules we obtain the matrix element

$$\begin{aligned} \sum_{\substack{\text{spins} \\ \text{colours}}} \langle \mathcal{M}_{q\bar{q}}^{(0)} | \mathcal{M}_{q\bar{q}}^{(1)} \rangle &= \alpha_s C_F N_c \sum_q e_q^2 2^{2-D} \pi^{1-D/2} \\ &\times \int \frac{d^D k}{i\pi^{D/2}} \frac{\text{Tr}[\gamma^\mu (\not{k} + \not{p}_2) \gamma^\nu (\not{k} - \not{p}_1) \gamma_\mu \not{p}_1 \gamma_\nu \not{p}_2]}{k^2 (k - p_1)^2 (k + p_2)^2}, \end{aligned} \quad (1.42)$$

where k is the momentum of the gluon in the first diagram of Fig. 1.2 and p_1, p_2 are the momenta of the external (anti)quark¹. The k -integral can be performed and the IR divergences become explicit as poles in the regulating parameter, ϵ :

$$\begin{aligned} \sum_{\substack{\text{spins} \\ \text{colours}}} \langle \mathcal{M}_{q\bar{q}}^{(0)} | \mathcal{M}_{q\bar{q}}^{(1)} \rangle &= \alpha_s C_F N_c \sum_q e_q^2 (-1)^{-\epsilon} 2^{1+2\epsilon} \pi^{-1+\epsilon} s^{1-\epsilon} \mu^{2\epsilon} \left(\frac{1-\epsilon}{1-2\epsilon} \right) \\ &\times \frac{\Gamma(1+\epsilon)\Gamma^2(1-\epsilon)}{\Gamma(1-2\epsilon)} \left[-\frac{1}{\epsilon^2} + \frac{1}{2\epsilon} - 1 \right], \end{aligned} \quad (1.43)$$

¹In the conventional dimensional regularisation scheme it turns out that the other two diagrams give zero contribution.

where $\Gamma(1+x)$ is the well known Euler Gamma function and s is the Mandelstam variable equal to the square of the centre of mass energy. Integrating this over the two body phase space,

$$\int d\Pi_2 = \frac{1}{8\pi} \frac{\Gamma(1-\epsilon)}{\Gamma(2-2\epsilon)} \left(\frac{4\pi}{s}\right)^\epsilon \int dS \delta(S-s), \quad (1.44)$$

gives the result

$$\begin{aligned} \sigma_{q\bar{q}}^{(1)} = \sigma_{q\bar{q}}^{(0)} C_F \frac{\alpha_s}{2\pi} \left(\frac{4\pi\mu^2}{s}\right)^\epsilon & \left[-\frac{2}{\epsilon^2} + \frac{(-3+2\gamma_E)}{\epsilon} \right. \\ & \left. + (-8 - \gamma_E(\gamma_E - 3) + 7\zeta(2)) + \mathcal{O}(\epsilon) \right], \quad (1.45) \end{aligned}$$

where Riemann $\zeta(2) \simeq 1.6449$.

The LO Real Correction

We have seen that the NLO virtual correction to $R^{e^+e^-}$ is IR divergent, however the ratio is a physically measurable quantity so we must have missed something. The reason why this missing piece is the LO $e^+e^- \rightarrow q\bar{q}g$ will be fully explained in Section 1.5.2. For now, let us just calculate it.

Applying the Feynman rules to the matrix element in Eq. (1.41) gives

$$\begin{aligned} \sum_{\substack{\text{spins} \\ \text{colours}}} \langle \mathcal{M}_{q\bar{q}g}^{(0)} | \mathcal{M}_{q\bar{q}g}^{(0)} \rangle = 4\pi\alpha_s\mu^{2\epsilon} C_F N_c \sum_q e_q^2 & \left[\frac{\text{I}}{(2p_1 \cdot k)^2} + \frac{\text{II}}{(2p_1 \cdot k)(2p_2 \cdot k)} \right. \\ & \left. + \frac{\text{III}}{(2p_2 \cdot k)(2p_1 \cdot k)} + \frac{\text{IV}}{(2p_2 \cdot k)^2} \right], \quad (1.46) \end{aligned}$$

where k represents the external gluon momentum and **I**, **II**, **III** and **IV**

represent trace terms shown below:

$$\begin{aligned} \mathbf{I} &= \text{Tr} [(\not{p}_1 + \not{k})\gamma_\mu \not{p}_1 \gamma^\mu (\not{p}_1 + \not{k})\gamma_\nu \not{p}_2 \gamma^\nu] \\ &= 8(D-2)^2(p_1 \cdot k)(p_2 \cdot k), \end{aligned} \quad (1.47)$$

$$\begin{aligned} \mathbf{II} &= \text{Tr} [\gamma^\mu (\not{p}_1 + \not{k})\gamma^\nu \not{p}_1 \gamma_\mu (\not{p}_2 + \not{k})\gamma_\nu \not{p}_2] \\ &= 8(D-2) [2(p_1 \cdot p_2)^2 + 2\{(p_1 \cdot k) + (p_2 \cdot k)\}(p_1 \cdot p_2) \\ &\quad + (D-4)(p_1 \cdot k)(p_2 \cdot k)]. \end{aligned} \quad (1.48)$$

IV and **III** are obtained by exchanging $p_1 \leftrightarrow p_2$ in **I** and **II** respectively. Suggestively, it is convenient to define particle momentum fractions

$$x_i \equiv \frac{2p_i \cdot Q}{s} = \frac{2E_i}{\sqrt{s}}, \quad (1.49)$$

where $s \equiv (p_1 + p_2)^2$ and Q is the momentum carried by the γ^* (with $Q^2 = s$). These are easily related to angles θ_{ij} between two external partons via

$$x_i x_j (1 - \cos \theta_{ij}) = 2(1 - x_k), \quad (1.50)$$

with $(i, j, k) = \text{perm}(1, 2, 3)$. In terms of these variables the matrix element becomes

$$\begin{aligned} \sum_{\substack{\text{spins} \\ \text{colours}}} \langle \mathcal{M}_{q\bar{q}g}^{(0)} | \mathcal{M}_{q\bar{q}g}^{(0)} \rangle &= 8\pi\alpha_s \mu^{2\epsilon} C_F N_c \sum_q e_q^2 (D-2) \\ &\times \left[(D-2) \left(\frac{1-x_1}{1-x_2} + \frac{1-x_2}{1-x_1} \right) + 4 \frac{x_1+x_2-1}{(1-x_1)(1-x_2)} + 2(D-4) \right]. \end{aligned} \quad (1.51)$$

In obtaining this we have eliminated x_3 using the fact that the x_i must sum

to 2 to satisfy energy conservation. Three body phase space in terms of the x_i is

$$\int d\Pi_3 = \frac{1}{128\pi^3} \frac{s}{\Gamma(2-2\epsilon)} \left(\frac{4\pi}{s}\right)^{2\epsilon} \int \left[\prod_{i=1}^3 dx_i (1-x_i)^{-\epsilon} \right] \delta\left(2 - \sum_{i=1}^3 x_i\right). \quad (1.52)$$

Rewriting the denominators of Eq. (1.51) using Eq. (1.50):

$$1 - x_1 = \frac{2E_q E_g}{s} (1 - \cos\theta_{qg}) \quad \text{and} \quad 1 - x_2 = \frac{2E_{\bar{q}} E_g}{s} (1 - \cos\theta_{\bar{q}g}), \quad (1.53)$$

we can see clearly the singularities in the phase space. The factors of $(1-x_i)$ vanish when either θ_{qg} or $\theta_{\bar{q}g} \rightarrow 0$ - the *collinear singularities*, or when $E_g \rightarrow 0$ - the *soft singularity*. Since we are using CDR these will become apparent as poles in ϵ . Integrating over the x_i gives

$$\begin{aligned} \sigma_{q\bar{q}g}^{(0)} = \sigma_{q\bar{q}}^{(0)} C_F \frac{\alpha_s}{2\pi} \left(\frac{4\pi\mu^2}{s}\right)^\epsilon & \left[\frac{2}{\epsilon^2} + \frac{(3-2\gamma_E)}{\epsilon} \right. \\ & \left. + \left(\frac{19}{2} + \gamma_E(\gamma_E-3) - 7\zeta(2)\right) + \mathcal{O}(\alpha_s^2) \right] \end{aligned} \quad (1.54)$$

The Cancellation

Having assembled the relevant cross sections we can construct the cross section, correct to $\mathcal{O}(\alpha_s)$, for the process $e^+e^- \rightarrow q\bar{q} + X$

$$\begin{aligned} \sigma_{q\bar{q}+X} &= \lim_{\epsilon \rightarrow 0} (\sigma_{q\bar{q}}^{(0)} + \sigma_{q\bar{q}}^{(1)} + \sigma_{q\bar{q}g}^{(0)}) + \mathcal{O}(\alpha_s^2) \\ &= \sigma_{q\bar{q}}^{(0)} \left[1 + \frac{\alpha_s}{\pi} + \mathcal{O}(\alpha_s^2) \right]. \end{aligned} \quad (1.55)$$

A finite result! This gives us the NLO correction to $R^{e^+e^-}$

$$R^{e^+e^-} = N_c \sum_q e_q^2 \left[1 + \frac{\alpha_s}{\pi} + \mathcal{O}(\alpha_s^2) \right]. \quad (1.56)$$

To compare with the measurement made at $\sqrt{s} = 34$ GeV of $R^{e^+e^-} = 3.9$ we take the value of $\alpha_s = 0.15$, obtaining our NLO prediction of $R^{e^+e^-} = 3.84$. Thus we have greatly improved the theoretical prediction.

The Origin of the Singularities in $\sigma_{q\bar{q}g}^{(0)}$

The propagator of the parent quark of the gluon has the following form:

$$\frac{1}{(p_q + k)^2} = \frac{1}{2E_q E_g (1 - \cos \theta_{qg})} \sim \frac{1}{E_g \theta_{qg}^2}, \quad (1.57)$$

thus the divergent behaviour of squared matrix elements is given by

$$|\mathcal{M}|^2 \propto \left(\frac{\theta_{qg}}{E_g \theta_{qg}^2} \right)^2. \quad (1.58)$$

The integration over the doubly singular region of phase space can be written as

$$\int \frac{d\phi d\theta_{qg} \theta_{qg} dE_g E_g^2}{E_g} \sim \int d\phi d\theta_{qg} \theta_{qg} dE_g E_g \quad (1.59)$$

and consequently the divergent contribution to the cross section is

$$\sigma \sim \int d\phi \frac{d\theta_{qg}^2}{\theta_{qg}^2} \frac{dE_g}{E_g}. \quad (1.60)$$

Therefore, each type of singularity contributes a *singly logarithmic* divergence to the cross section, leading to a *doubly logarithmic* singularity in the soft and collinear region.

1.5.2 Infra-Red Safety

Later in this thesis we shall explore the consequences of soft gluon emission in a hadronic event. We will see that these processes also have singularities in the phase space. The point should be emphasised that these divergences *do not* appear in the *total* hadronic cross section for precisely the reasons outlined above.

To summarise, in order to calculate $e^+e^- \rightarrow$ hadrons to any order in perturbation theory we should not calculate $e^+e^- \rightarrow q\bar{q}$ which is an *exclusive* process. Instead we should consider $e^+e^- \rightarrow q\bar{q} + X$ to the required order - this is an *inclusive* process.

The cancellation of divergences between different orders is no accident, indeed the Kinoshita-Lee-Nauenberg (KLN) theorem [6, 7] guarantees this will occur. KLN states that:

In a theory with massless fields, transition probabilities are free of IR divergences if all degenerate initial and final states are taken into account.

Any quantity that sums over possible initial and final states is said to be *infra-red* safe. The total hadronic cross section is an example of an IR safe quantity.

An alternative (and intuitive) way of viewing how this works in our example is to realise that, in any experiment, the observed quantities are not perturbative partons but *jets* of hadrons. During the process of hadronisation, soft and collinear partons will become absorbed into any definition of the jet. Thus, if the gluon in the LO $q\bar{q}g$ event is soft or collinear then it will be ‘mistaken’ for a $q\bar{q}$ event.

1.5.3 Infra-Red Safe Definitions of Jets

The coloured partons in the final state of any event that we calculate perturbatively *fragment* into colourless hadrons. These will remain collimated and roughly follow the momentum of the parent parton. We need a practical method to tell us how to group the observed hadrons into jets originating from a particular parton. As long as we do not resolve soft and collinear gluon emission our method will be IR safe. Popular definitions are:

Cone Algorithm (Sternan-Weinberg)

For two jets, all but a fraction, ϵ , of the total energy is contained within a pair of cones of half angle, δ . Integrating the $q\bar{q}g$ matrix element over phase space gives the probability of a two jet event at $\mathcal{O}(\alpha_s)$ [8]

$$f_2(\epsilon, \delta) = 1 - 8C_F \frac{\alpha_s}{2\pi} \left\{ \ln \frac{1}{\delta} \left[\ln \left(\frac{1}{2\epsilon} - 1 \right) - \frac{3}{4} + 3\epsilon \right] + \frac{\pi^2}{12} - \frac{7}{16} - \epsilon + \frac{3}{2}\epsilon^2 + \mathcal{O}(\delta^2 \ln \epsilon) \right\}, \quad (1.61)$$

then the three jet rate is just $f_3 = 1 - f_2$.

JADE Algorithm

The Sternan-Weinberg definition is ill-suited for studying multijet final states. One reason is cones of fixed angle lead to an inefficient tiling of the 4π solid angle. An alternative is the JADE algorithm, also known as the minimum invariant mass algorithm. A three jet event is defined as one in which the minimum invariant mass of the parton pairs is larger than some fixed fraction y_{cut} :

$$\min(p_i + p_j)^2 = \min 2E_i E_j (1 - \cos \theta_{ij}) > y_{\text{cut}} \quad (1.62)$$

for massless partons. Integrating the $q\bar{q}g$ matrix element over this phase space gives

$$f_3(y_{\text{cut}}) = C_F \frac{\alpha_s}{2\pi} \left[(3 - 6y_{\text{cut}}) \ln \left(\frac{y_{\text{cut}}}{1 - 2y_{\text{cut}}} \right) + 2 \ln^2 \left(\frac{y_{\text{cut}}}{1 - y_{\text{cut}}} \right) + \frac{5}{2} - 6y_{\text{cut}} - \frac{9}{2}y_{\text{cut}}^2 + 4\text{Li}_2 \left(\frac{y_{\text{cut}}}{1 - y_{\text{cut}}} \right) - \frac{\pi^3}{3} \right] \quad (1.63)$$

where the dilogarithm function

$$\begin{aligned} \text{Li}_2(x) &\equiv - \int_0^x dy \frac{\ln(1-y)}{y} \\ &= \frac{x}{1^2} + \frac{x^2}{2^2} + \frac{x^3}{3^2} + \dots \quad \text{for } |x| \leq 1. \end{aligned} \quad (1.64)$$

Then $f_2 = 1 - f_3$.

k_T (Durham) Algorithm

JADE is well suited to experimental jet measurements, but is problematic theoretically. It tends to reconstruct spurious jets that do not lie collinear to a set of hadrons in an event. If a soft gluon is radiated from each of two almost back to back jets into the same hemisphere, JADE will group these two gluons into a jet if their invariant mass is smaller than y_{cut} , *even if the angle between them is large*. This is connected with the fact that the algorithm is not amenable to *resummation*, a concept that will be explained in Section 1.7. The solution is to replace the invariant mass measure in Eq. (1.62) by a quantity which, when the angle between the partons is small, is the minimum of the relative transverse momentum

$$2\min(E_i^2, E_j^2)(1 - \cos\theta_{ij}) > y_{\text{cut}} \quad (1.65)$$

As with JADE, one may calculate expressions for f_3 and f_2 in perturbation theory. In addition, one may also resum the large logarithms.

1.6 Initial State Hadrons and Factorisation

Can we meaningfully define IR safe quantities when we have hadrons in the initial state or particular hadrons in the final state? The answer is yes, because of the property of *QCD factorisation*. We are able to factorise out the short distance, perturbatively calculable physics, from the long distance, confining physics, which must be experimentally determined. In general, the factorisation theorem must be proved for each process separately. It is the property of factorisation that enabled the establishment of the parton model in describing deeply inelastic electron-proton scattering. There are many texts discussing factorisation in QCD in both DIS and hadron-hadron collisions, see for example [9]. During this thesis, we will be considering processes at hadron colliders, therefore we will outline factorisation in Drell-Yan production.

1.6.1 Factorisation in the Drell-Yan Process

The hadronic production of a lepton pair is referred to as the Drell-Yan process

$$A + B \rightarrow X + \gamma^*(\rightarrow l^+ + l^-) + Y \quad (1.66)$$

where X and Y denote hadron remnants that we do not require to observe (this guarantees that the process is inclusive). The cross section is given

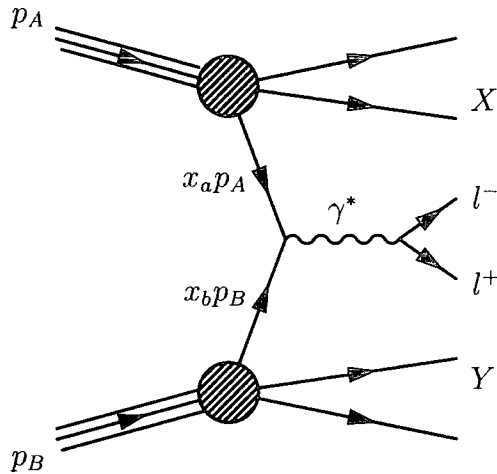


Figure 1.4: Drell-Yan production.

by the factorisation theorem

$$\sigma(p_A, p_B) = \sum_{a,b} \int_0^1 \int_0^1 dx_a dx_b f_{a/A}(x_a, \mu_F^2) f_{b/B}(x_b, \mu_F^2) \hat{\sigma}_{ab}(x_a p_A, x_b p_B, \alpha_s(\mu_F^2), Q^2/\mu_F^2). \quad (1.67)$$

Here, the scattering hadrons have momenta p_A and p_B . $\hat{\sigma}_{ab}$ is the IR safe hard scattering subprocess cross section that is perturbatively calculable from the IR divergent partonic cross section by removing the singularities and absorbing them into the *parton distribution functions* (PDF's) $f_{a/A}$. In the parton model, these represent the probability of finding a parton of type a with a fraction, x_a , of the hadrons momentum, in a hadron of type A . Since they contain collinear divergences they are non-perturbative functions sensitive to long distance physics and must therefore be determined from experiment. Q is the typical scale of the hard subprocess. μ_F is the *factorisation scale*, an arbitrary parameter that separates long and short distance physics. A parton emitted with transverse momentum less than μ_F is considered to be part of the hadron structure and is absorbed into the PDF. In Eq. (1.67) the factorisation scale has been set equal to the renormalisation scale for

simplicity. In fact, it is usual to set $\mu_F = \mu_R = Q$.

1.6.2 DGLAP Evolution of Parton Distribution Functions

Consider how our factorised Drell-Yan cross section (Eq. (1.67)) depends on variation of the arbitrary factorisation scale. The RGE has the following form

$$\mu_F^2 \frac{df_{a/A}(x, \mu_F^2)}{d\mu_F^2} = \sum_b \int_x^1 \frac{d\zeta}{\zeta} P_{ab} \left(\frac{x}{\zeta}, \alpha_s(\mu_F^2) \right) f_{b/A}(\zeta, \mu_F^2). \quad (1.68)$$

This is called the Dokshitzer-Gribov-Lipatov-Altarelli-Parisi (DGLAP) evolution equation [10–12]. It enables us to evolve any given PDF to another scale according to QCD. The right-hand side would be zero in the parton model as it describes QCD scaling violation. The functions P_{ab} are called *splitting functions*, describing the splitting of parton b into parton a , and are perturbatively calculable. At leading order they are

$$P_{qq}(x) = C_F \left[\frac{1+x^2}{(1-x)_+} + \frac{3}{2} \delta(1-x) \right] \quad (1.69)$$

$$P_{qg}(x) = T_R [x^2 + (1-x)^2] \quad (1.70)$$

$$P_{gq}(x) = C_F \left[\frac{1+(1-x)^2}{x} \right] \quad (1.71)$$

$$P_{gg}(x) = 2C_A \left[\frac{x}{(1-x)_+} + \frac{1-x}{x} + x(1-x) \right] + \delta(1-x) \frac{(11C_A - 4N_F T_R)}{6}, \quad (1.72)$$

where a *plus distribution* is defined as

$$\int_0^1 dx \frac{f(x)}{(1-x)_+} \equiv \int_0^1 \frac{f(x) - f(1)}{1-x}. \quad (1.73)$$

The splitting functions are also known at NLO [13, 14].

1.7 Resummation

In Section 1.5 we computed the NLO correction to the ratio of total cross sections for hadron and muon production at an electron-positron collider, however this tells us nothing about the *shape* of an event. It is surely reasonable to expect a predictive theory such as QCD to say something about differential distributions.

If we assume collinear fragmentation of a parton into hadrons then we might expect a leading order $e^+e^- \rightarrow q\bar{q}$ process would look like two back-to-back jets - a *two jet event*. At NLO we have discovered that the matrix element for $q\bar{q}g$ is much larger when the gluon is close to one of the quarks. Therefore we would expect that $q\bar{q}g$ events exhibit two jet and three jet configurations, but with three jets being suppressed by $\mathcal{O}(\alpha_s)$.

1.7.1 Resummation in an Event Shape Variable: Thrust

In order to quantify shape, we need to define an IR safe variable. An example of one such variable is *thrust*

$$T \equiv \max_{\vec{n}} \frac{\sum_i |\vec{p}_i \cdot \vec{n}|}{\sum_i |\vec{p}_i|} \quad (1.74)$$

where \vec{n} is the vector that maximises the numerator. An event that is exactly back-to-back thus has $T = 1$ and one that is exactly isotropic has $T = 1/2$. The perturbative prediction for thrust has the form

$$\frac{1}{\sigma} \frac{d\sigma}{dT} = \alpha_s [A_1(T) + \alpha_s A_2(T, s/\mu^2) + \alpha_s^2 A_3(T, s/\mu^2) + \dots] \quad (1.75)$$

where $\alpha_s = \alpha_s(\mu^2)$. Currently $A_1(T)$ and $A_2(T, s/\mu^2)$ are known in full. There are a number of sources of unreliability in comparing this result with data. In addition to higher order corrections, renormalisation scale dependence and hadronisation corrections, there is an effect which shows up as $T \rightarrow 1$. To see this, let us compute $A_1(T)$.

Rewriting our expression for the LO $q\bar{q}g$ cross section, Eq. (1.54), as an integral over the two independent momentum fractions

$$\sigma_{q\bar{q}g}^{(0)} = \sigma_{q\bar{q}}^{(0)} 3e_q^2 \int_I dx_1 dx_2 \frac{2\alpha_s}{3\pi} \frac{x_1^2 + x_2^2}{(1-x_1)(1-x_2)} \quad (1.76)$$

and noticing that in terms of the momentum fractions

$$T = \max\{x_1, x_2, x_3\}, \quad (1.77)$$

we see that in order to obtain the thrust distribution we must integrate

$$\frac{1}{\sigma_{q\bar{q}}^{(0)}} \frac{d^2\sigma}{dx_1 dx_2} = \frac{\alpha_s}{2\pi} C_F \frac{x_1^2 + x_2^2}{(1-x_1)(1-x_2)} \quad (1.78)$$

over

$$\int dx_1 dx_2 \delta(T - \max\{x_1, x_2, 2 - x_1 - x_2\}). \quad (1.79)$$

This gives

$$\alpha_s A_1(T) = \frac{1}{\sigma} \frac{d\sigma}{dT} = \frac{\alpha_s}{2\pi} C_F \left[\frac{2(3T^2 - 3T + 2)}{T(1-T)} \ln \frac{2T-1}{1-T} - \frac{3(3T-2)(2-T)}{1-T} \right]. \quad (1.80)$$

Now we see the source of the problem:

$$A_1(T) \underset{T \rightarrow 1}{\sim} \frac{-\ln(1-T)}{1-T}. \quad (1.81)$$

In fact this malady generalises to all orders

$$A_n(T) \underset{T \rightarrow 1}{\sim} \frac{-\ln^{2n-1}(1-T)}{(1-T)n!}. \quad (1.82)$$

Perturbation theory has a problem in this region. The requirement that $\alpha_s \ll 1$ is no longer sufficient. Instead we must have $\alpha_s \ln^2(1-T) \ll 1$.

We are able to systematically extend the region of applicability of perturbation theory by identifying the large logarithms and re-ordering the series expansion in such a way that these terms are taken into account at *all orders* in α_s . This is the resummation procedure. Performing this for thrust, taking the first logarithmic term at each order (the *leading logarithmic approximation*) leads to an exponential series that we write as

$$\frac{1}{\sigma} \frac{d\sigma}{dT} \underset{T \rightarrow 1}{\sim} \frac{\alpha_s - 4C_F \ln(1-T)}{2\pi(1-T)} \exp \left\{ -\frac{\alpha_s}{2\pi} 2C_F \ln^2(1-T) \right\}. \quad (1.83)$$

In general, the full series is

$$\frac{1}{\sigma} \frac{d\sigma}{dT} = -\frac{d}{dT} \left\{ \mathcal{C}(\alpha_s) e^{\mathcal{G}(\alpha_s, L)} + \mathcal{D}(\alpha_s, T) \right\} \quad (1.84)$$

where $L \equiv -\ln(1 - T)$,

$$\mathcal{C}(\alpha_s) \equiv 1 + \sum_{n=1}^{\infty} C_n \left(\frac{\alpha_s}{2\pi}\right)^n, \quad (1.85)$$

$$\begin{aligned} \mathcal{G}(\alpha_s, L) &\equiv \sum_{n=1}^{\infty} \sum_{m=1}^{n+1} G_{nm} \left(\frac{\alpha_s}{2\pi}\right)^n L^m \\ &= Lg_1(\alpha_s L) + g_2(\alpha_s L) + \alpha_s g_3(\alpha_s L) + \dots \end{aligned} \quad (1.86)$$

and the finite remainder $\mathcal{D}(\alpha_s, T)$ vanishes as $T \rightarrow 1$. The function g_1 resums all the leading logarithmic terms of order $\alpha_s^n L^{n+1}$, g_2 resums the next-to-leading logarithmic (NLL) terms $\alpha_s^n L$ and all the other g 's resum subdominant corrections. Provided we know g_1 and g_2 , we may extend the region of predictability from $\alpha_s \ln^2(1 - T) \ll 1$ to $\alpha_s \ln(1 - T) \leq 1$.

1.8 Summary

In this Chapter we have provided a brief overview of the theory of QCD. We started from the basic mathematical building blocks of a locally gauge invariant field theory with a non-abelian symmetry. We considered the perturbative expansion of this and showed that it was renormalisable and IR safe. We then explored how non-perturbative quantities factorise from perturbative ones, thus allowing us to parametrise the strongly coupled regions of the initial and final states. Finally, we showed how the region of applicability of perturbation theory can be extended by the means of resummation.

The subject of this thesis is the study of hadronic Higgs production in a certain kinematical regime. We must therefore sketch the other half of the Standard Model of particle physics - the electroweak theory, and see how

the Higgs boson arises from it. This we do in Chapter 2. In Chapter 3 we apply this knowledge to the specific case of hadronic Higgs production and discuss the current experimental challenges. We argue that the established Higgs search channels do not guarantee a swift discovery and present an additional class of modes that we believe merit further exploration by the particle physics community. In Chapter 4 we conduct a detailed study of one of these channels: Higgs production via vector boson fusion with rapidity gaps. We use the novel method of calibrating against a known particle production process in order to control ambiguities caused by a model of the non-perturbative structure of the proton. In Chapter 5 we relax our requirement of rapidity gaps and consider the distribution of soft hadrons in signal and background events. This proves to be a useful additional discriminatory tool. Finally, in Chapter 6 we explore the applicability of using a high energy limit and an equivalent gluon approximation to describe the Higgs production with forward jets and its backgrounds.

Chapter 2

The Standard Electroweak Model and its Broken Symmetry

The focus of this thesis is to investigate QCD effects at the Large Hadron Collider. The aim is to understand these more fully in order that we may separate them from any new physics phenomena. Specifically, the most pressing issue in contemporary particle physics is the need to establish or refute the existence of a Higgs boson. It is therefore appropriate to give a brief account of the theoretical justification for this new particle. More generally, if we wish to study high energy physics we need a working knowledge of quantum electrodynamics and the weak interaction. In the 1970's these were unified to form a single electroweak Standard Model that predicted the heavy gauge bosons W and Z [15–17]. These were subsequently discovered at UA1 and UA2 in 1983 [18, 19].

In this Chapter we outline this theory, a more complete treatment can be found in, for example [20] .

2.1 The Electroweak Symmetry

The gauge group of the Standard Electroweak Model is $SU(2)_L \otimes U(1)_Y$, this has two conserved charges and two couplings g and g' . The number of states in the adjoint representation and hence the number of massless gauge bosons is thus three from the $SU(2)_L$ ($W_\mu^i, i = 1, 2, 3$) plus one from the $U(1)_Y$ (B_μ). However, there is only one massless electroweak gauge boson in Nature, the photon. Also a Lagrangian constructed from this symmetry cannot have a mass term for fermions. We are thus forced to modify the theory in such a way that there will remain only a single conserved quantity, electric charge, corresponding to a single massless gauge boson. This modification must also permit fermionic mass terms. The construction by which we achieve this is called the *Higgs mechanism*.

2.1.1 Higgs Mechanism

The simplest (but by no means only) way to break our $SU(2)_L \otimes U(1)_Y$ symmetry down to $U(1)_Q$ is by introducing a complex doublet of scalar fields, $\phi \equiv \begin{pmatrix} \phi^+ \\ \phi^0 \end{pmatrix}$. We add to our original Lagrangian a term representing free propagation of this scalar and also a Yukawa interaction term between it and the fermions. We then choose the coefficient of the quadratic term in the scalar potential to be negative. This *spontaneously breaks* the symmetry by creating a nonzero vacuum expectation value. Each original generator of the gauge group no longer leaves the vacuum invariant. However, the combination corresponding to the electric charge does. Expanding the Lagrangian about this new vacuum reveals that the fermions have acquired mass terms, as have the intermediate vector bosons. Moreover, our new scalar field also acquires a mass term, this corresponds to a massive, physical *Higgs boson* [21, 22].

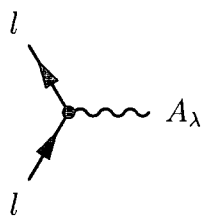
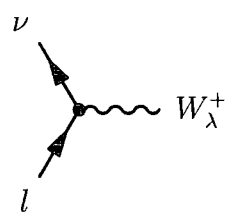
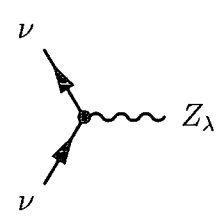
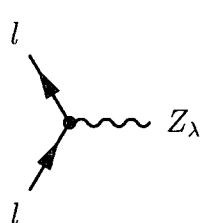
$-ie\bar{l}\gamma_\lambda l$	=	
$-i\left(\frac{G_F m_W^2}{\sqrt{2}}\right)^{1/2} \bar{\nu}\gamma_\lambda(1-\gamma_5)l$	=	
$-\frac{i}{\sqrt{2}}\left(\frac{G_F m_Z^2}{\sqrt{2}}\right)^{1/2} \bar{\nu}\gamma_\lambda(1-\gamma_5)\nu$	=	
$-\frac{i}{\sqrt{2}}\left(\frac{G_F m_Z^2}{\sqrt{2}}\right)^{1/2} \bar{l}\gamma_\lambda [R_l(1+\gamma_5) + L_l(1-\gamma_5)]l$	=	

Table 2.1: Feynman rules for electroweak lepton-vector boson interactions.

2.2 Electroweak Feynman Rules

Expanding out our spontaneously broken Lagrangian, we can extract the Feynman rules in the same way as we did for QCD. We denote left handed fermion fields $\psi_i = \begin{pmatrix} \nu_i \\ l_i^- \end{pmatrix}$ and $\psi_i = \begin{pmatrix} u_i \\ d_i^- \end{pmatrix}$ which transform as doublets under $SU(2)$ where $d' \equiv \sum_j V_{ij} d_j$ and V is called the *Cabbibo-Kobayashi-Maskawa* (CKM) mixing matrix. This is needed because the mass eigenstates do not correspond to the weak eigenstates, therefore there is mixing between quark flavours. For brevity, we present here only the broken Lagrangian for the fermion fields. This has the following form

$$\begin{aligned}
\mathcal{L}_f = & \sum_i \bar{\psi}_i \left(i\not{\partial} - m_i - \frac{gm_i H}{2m_W} \right) \psi_i \\
& - \frac{g}{2\sqrt{2}} \sum_i \bar{\psi}_i \gamma^\mu (1 - \gamma_5) (T^+ W_\mu^+ + T^- W_\mu^-) \psi_i \\
& - e \sum_i q_i \bar{\psi}_i \gamma^\mu \psi_i A_\mu \\
& - \frac{g}{2 \cos \theta_W} \sum_i \bar{\psi}_i \gamma^\mu (V^i - A^i \gamma_5) \psi_i Z_\mu.
\end{aligned} \tag{2.1}$$

$\theta_W \equiv \tan^{-1}(g'/g)$ is the Weinberg angle; $e = g \sin \theta_W$ is the positron electric charge; and $A \equiv B \cos \theta_W + W^3 \sin \theta_W$ is the photon field. $W^\pm \equiv (W^1 \mp iW^2)/\sqrt{2}$ and $Z \equiv -B \sin \theta_W + W^3 \cos \theta_W$ are the now massive charged and neutral weak boson fields. T^\pm are the weak isospin raising and lowering operators. The vector and axial vector couplings are

$$\begin{aligned}
V^i & \equiv T_{3L}(i) - 2q_i \sin^2 \theta_W \\
A^i & \equiv T_{3L}(i)
\end{aligned} \tag{2.2}$$

where $T_{3L}(i)$ is the weak isospin of fermion i and q_i is the charge of ψ_i in units of e .

The first term in Eq. (2.1) describes free propagation, mass and Higgs (H) interactions of the fermions. The second term describes the charged weak current where the constant g can be related (at energies small compared to m_W) to Fermi's effective theory via the tree level relation, $G_F/\sqrt{2} = g^2/8m_W^2$. The third term describes QED and the last is the weak neutral current.

Tables 2.1, 2.2 and 2.3 show the derived rules for fermion-boson, boson-boson and Higgs vertices. There are many texts that provide a more complete account of the derivation of the Feynman rules, for example [20].

As with QCD, the gauge group is non-Abelian and we therefore have boson self interactions. The Higgs couples to all particles in proportion to their mass, therefore if we wish to establish its existence we must consider processes where it couples to a heavy particle.

2.3 Electroweak Parameter Space

In the twenty years since the confirmation of the electroweak theory, the parameter space has been determined with an astounding degree of precision at lepton colliders, most notably LEP. For example the mass of the Z boson is now known to an accuracy of one part in 10^5 ! Its value is $m_Z = 91.1882 \pm 0.0022$ GeV and was obtained by a scan of the Z lineshape at LEP1 [23]. Using this and the measured values for $m_W = 80.419 \pm 0.056$ GeV, $m_t = 174.3 \pm 5.1$ GeV and $\sin^2 \theta_W$ (which depends on the renormalisation scheme being used) one can constrain m_H due to its contribution to processes at higher orders in perturbation theory. Figure 2.1 [24] shows the $\Delta\chi^2$ likelihood plot derived from LEP and previous experiments as a function

$$\begin{aligned}
 ig_V [g_{\alpha\beta}(k_+ - k_-)_\lambda - g_{\alpha\lambda}(p + k_+)_\beta + g_{\beta\lambda}(p + k_-)_\alpha] &= \text{Diagram 1} \\
 g_A = e, \quad g_Z = g_W \cos \theta_W & \\
 ig_W^2 [2g_{\mu\nu}g_{\lambda\rho} - g_{\mu\lambda}g_{\nu\rho} - G_{\mu\rho}g_{\nu\lambda}] &= \text{Diagram 2} \\
 ig_W^2 \cos \theta_W [2g_{\mu\nu}g_{\lambda\rho} - g_{\mu\lambda}g_{\nu\rho} - G_{\mu\rho}g_{\nu\lambda}] &= \text{Diagram 3} \\
 ie^2 [2g_{\mu\nu}g_{\lambda\rho} - g_{\mu\lambda}g_{\nu\rho} - G_{\mu\rho}g_{\nu\lambda}] &= \text{Diagram 4} \\
 ieg_W \cos \theta_w [2g_{\mu\nu}g_{\lambda\rho} - g_{\mu\lambda}g_{\nu\rho} - G_{\mu\rho}g_{\nu\lambda}] &= \text{Diagram 5}
 \end{aligned}$$

Table 2.2: Feynman rules for electroweak vector boson self-interactions.

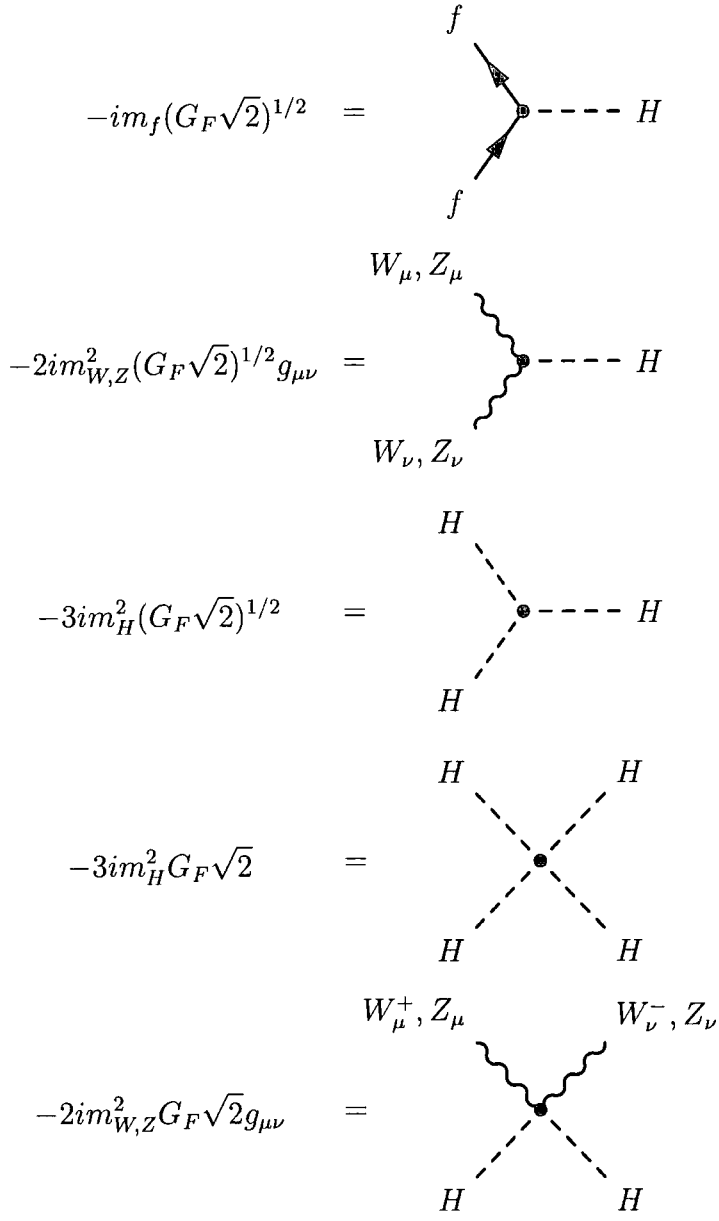


Table 2.3: Feynman rules for Higgs interactions

of the Standard Model Higgs boson mass. The plot summarises to what extent the Higgs mass can be constrained through higher order corrections to the observed electroweak quantities. For example, the Z, W propagator is modified by a Higgs loop such that $\delta_H \propto \ln(m_H/m_{Z,W})$. The best fit value is $m_H = 77^{+69}_{-39}$ GeV and $m_H < 215$ GeV at the 95% confidence level ($\Delta\chi^2 = 2.7$). The blue band is the uncertainty arising from unknown higher order contributions to processes involving the Higgs mass, including renormalisation scale dependence¹.

Through non-observance, LEP II has also placed a direct limit of $m_H > 114.4$ GeV at CL = 95% [25] (indicated by the yellow area on Fig. 2.1). This originates from the search channel $e^+e^- \rightarrow ZH$ with both bosons $\rightarrow b\bar{b}$ at $\sqrt{s} \rightarrow 206$ GeV.

Figure 2.2 [24] shows measurements of m_W comparing the LEP I/II results with that from the Tevatron/SPS and the NuTeV experiment. NuTeV obtains the mass (through $\sin^2\theta_W$) by measuring the ratio of $\sigma(\nu N) - \sigma(\nu\bar{N})$ between neutral and charged current interactions and has been a topic of great interest recently, being 2.9σ away from the world average.

¹The main source of error is due to the unknown NNLO contribution to $\sin^2\theta_{eff}$.

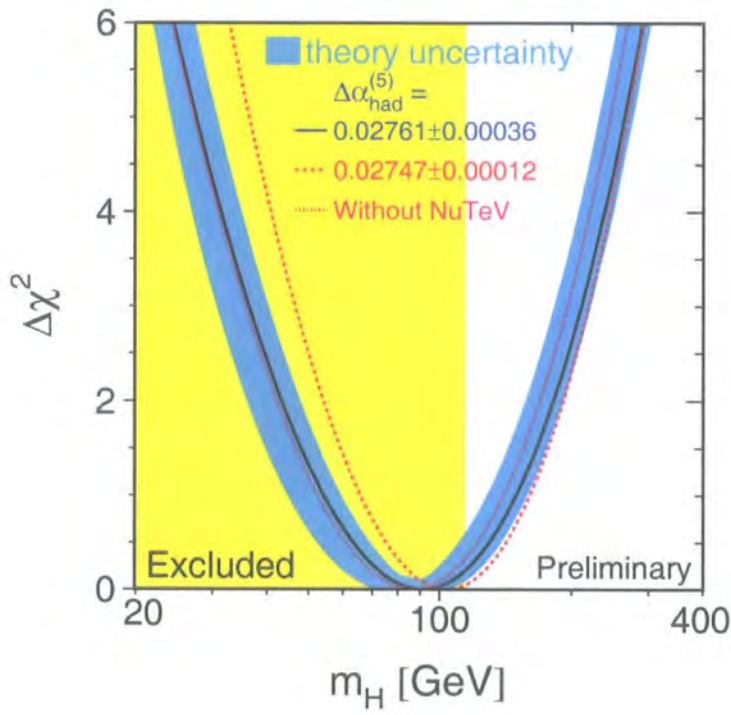


Figure 2.1: Electroweak Standard Model Higgs mass constraints.

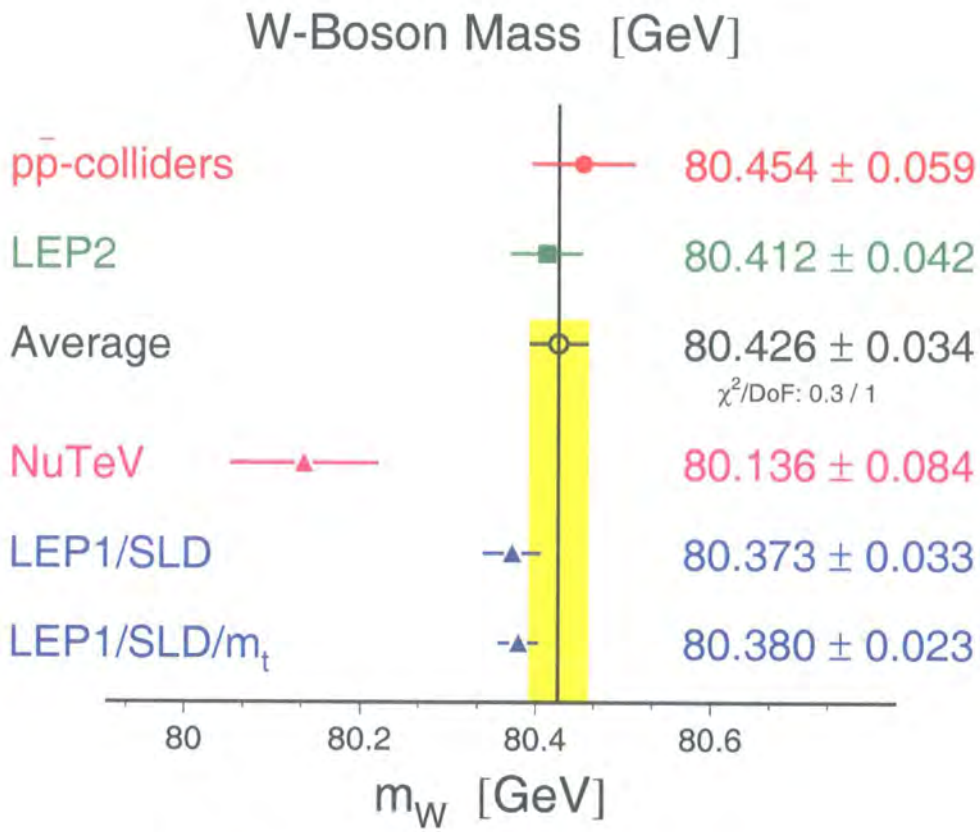


Figure 2.2: Recent W -boson mass measurements.

Chapter 3

Higgs Production at Hadron Colliders

The failure of LEP to detect a Higgs signal¹ leaves other colliders to confirm or refute its existence. At the time of writing, the main currently running experiment performing Higgs searches is the Fermilab Tevatron. In 2007 the Large Hadron Collider (LHC) is due to commence running at CERN. Both of these are hadron colliders, the Tevatron being proton-antiproton and the LHC proton-proton. In this Chapter, we will describe the main production and decay channels for the Higgs at hadron colliders and assess their advantages and shortcomings. We will concentrate on the LHC, but will note differences applicable to the Tevatron

3.1 Decay Channels

As previously discussed, the Higgs couples to massive fields. Figures 3.1 and 3.2 show the Standard Model branchings to fermions and bosons as a

¹In fact a small excess was seen at 115 GeV by ALEPH [26] and DELPHI [27]. A reanalysis downgraded the importance of this.

function of m_H [28].

Far below the WW threshold, $H \rightarrow b\bar{b}$ is dominant. At a hadron collider, this channel is swamped by continuum QCD $b\bar{b}$ production (see Fig. 3.4) which is $\sim 10^7$ times larger. Unless we have an additional way to discriminate signal and background (more of which in the following Chapter), it is experimentally useless. In fact, the channel that commands most attention is $H \rightarrow \gamma\gamma$ as the backgrounds are more manageable, even though its branching ratio is $\sim 10^{-3}$.

As the WW threshold is approached, off-shell $H \rightarrow WW$ and ZZ become dominant. Above threshold, branching to the heavy vector bosons is nearly 100% - even branching to $t\bar{t}$ is not large ($\sim 20\%$) when this threshold is reached. The most fruitful way to search for $H \rightarrow WW, ZZ$ experimentally is when the vector bosons both decay leptonically. In fact the ‘golden channel’ is $H \rightarrow ZZ \rightarrow 4\mu$.

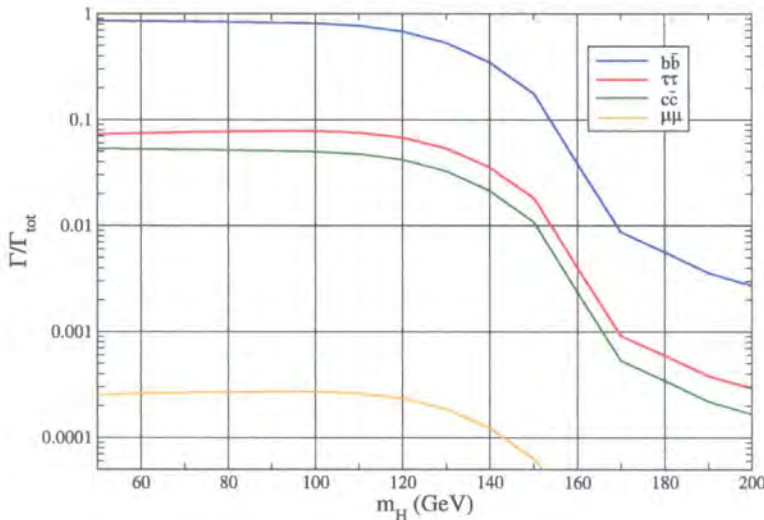


Figure 3.1: Standard Model branching ratios for $H \rightarrow$ fermions.

Of course, as m_H rises, the total decay width increases, becoming of the

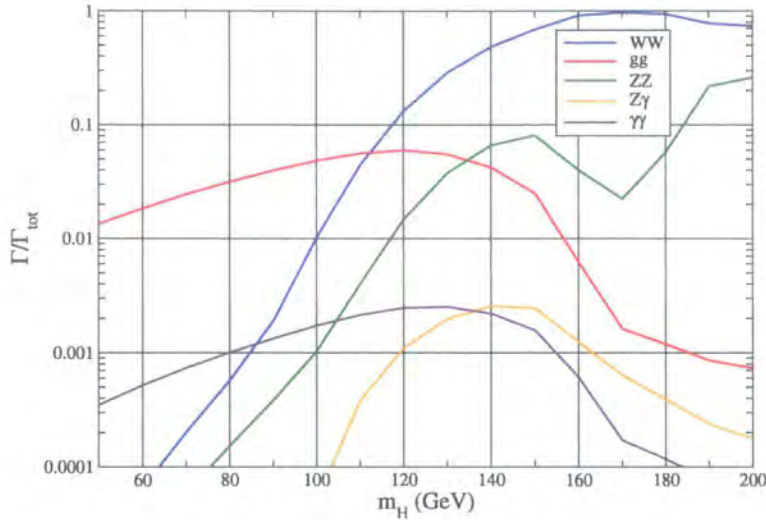


Figure 3.2: Standard Model branching ratios for $H \rightarrow$ bosons.

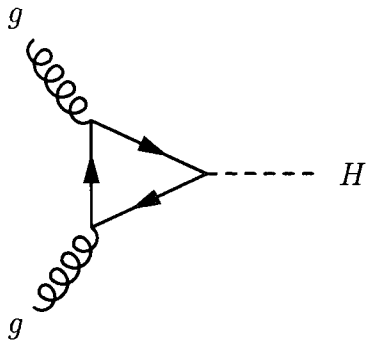
same order as its mass at around 2 TeV.

3.2 Production Mechanisms

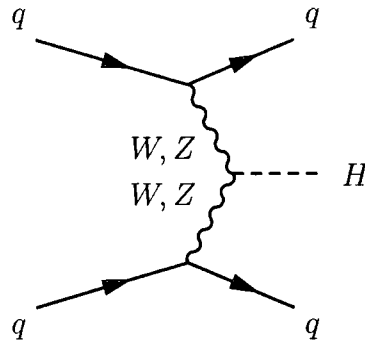
Table 3.1 shows the four observable production channels and Figure 3.3 [9] shows the leading order production cross sections at the LHC. These are calculated using the MRS98LO parton set. We will describe each process in detail.

3.2.1 Gluon Fusion

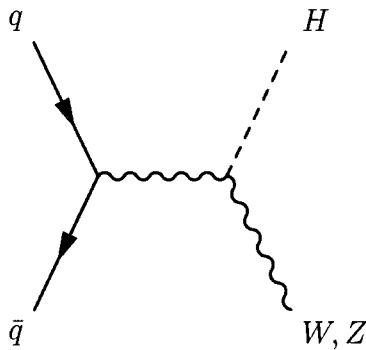
Over the whole range of the Higgs mass preferred by LEP, gluon fusion is the dominant production mode. This is already a higher order process, being mediated by heavy fermions in the loop. The only phenomenologically relevant fermion involved is the top quark. The spin summed, squared matrix



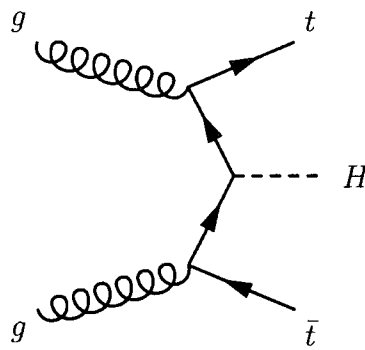
Gluon Fusion



Vector Boson Fusion



Associated Weak Boson Production



Associated Top Production

Table 3.1: Dominant hadronic Higgs production modes.

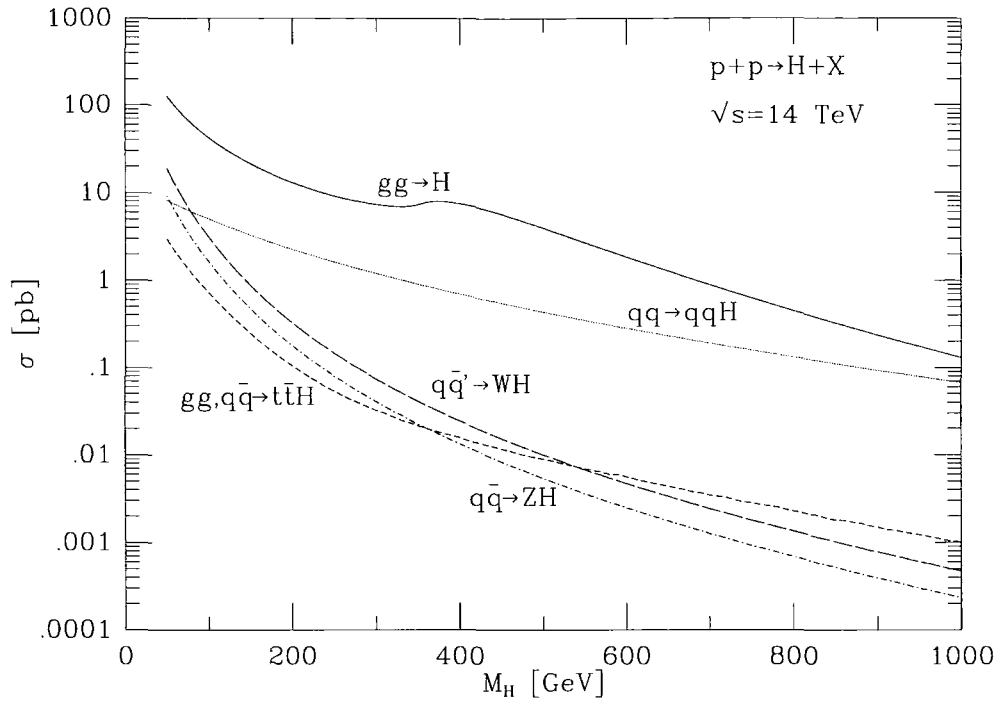


Figure 3.3: Hadronic Higgs production cross sections.

element is [29]

$$|\mathcal{M}(gg \rightarrow H)|^2 = \frac{\alpha_s^2(m_H^2) G_F m_H^4}{288 \sqrt{2} \pi^2} \left| I \left(\frac{m_t^2}{m_H^2} \right) \right|, \quad (3.1)$$

where $I(x)$ is a dimensionless function given by

$$I(x) = 3x[2 + (4x - 1)F(x)] \quad (3.2)$$

with

$$F(x) = \theta(1 - 4x) \frac{1}{2} \left[\ln \left(\frac{1 + \sqrt{1 - 4x}}{1 - \sqrt{1 - 4x}} \right) - i\pi \right] - \theta(4x - 1) 2 [\sin^{-1}(1/2\sqrt{x})]^2. \quad (3.3)$$

A reasonable approximation for $I(x)$ for the case where $m_t > m_H$ is $I(x) \simeq 1 + \frac{1}{4x}$. This defines an effective ggH vertex. The parton level cross section is

$$\hat{\sigma}(gg \rightarrow H) = \frac{\pi}{\hat{s}} \delta(\hat{s} - m_H^2) |\mathcal{M}(gg \rightarrow H)|^2. \quad (3.4)$$

The gluon fusion subprocess has also been calculated at NLO [30, 31] and recently at NNLO [32, 33]. These corrections increase the cross section by almost a factor of two over the whole range.

While it is dominant, gluon fusion is extremely problematic to identify in a hadronic environment because of its QCD induced nature. In order to resurrect the signal, one must rely on rare decay modes, the most popular being $H \rightarrow \gamma\gamma$ which has small QCD induced backgrounds.² This poses a major experimental challenge. Indeed, the CMS collaboration has invested greatly in producing an electromagnetic calorimeter with very fine granularity and energy resolution in order to pin down the diphoton mass [35]. The aim is that they will achieve sufficient precision to claim a 5σ discovery with this channel alone.

Figure 3.4 [36] shows leading order gluon fusion Higgs production for Higgs masses of 120, 200 and 500 GeV. The plot compares these with other important hadronic cross sections and the bands show errors originating from parton distribution function uncertainties.³ The kinks in the lines arise from switching our considerations from the proton-antiproton Tevatron to the proton-proton LHC. They thus occur in those final states dominated by quark induced processes.

²The main irreducible background to this is now very well determined thanks to a recent calculation of $pp \rightarrow \gamma\gamma$ at NLO [34]. At the time of writing the major worry is due to the reducible background from neutral pion decay, which can fake the diphoton signal.

³The NLO DGLAP evolved MRST2001 parton distributions [37] were used and uncertainties were estimated using the Hessian technique. For a detailed explanation of the errors see [38].

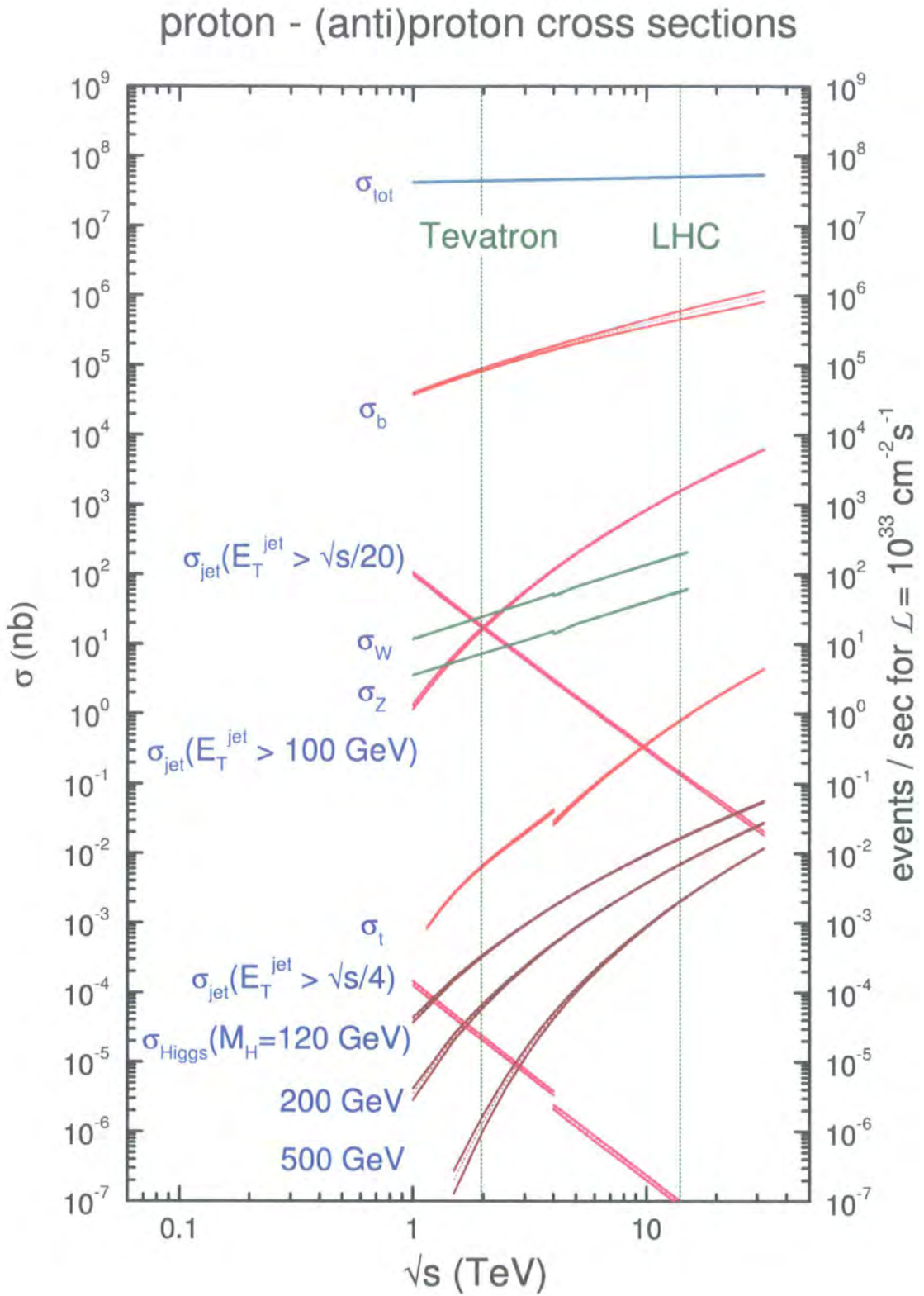


Figure 3.4: Benchmark hadronic cross sections.

3.2.2 Vector Boson Fusion

Assuming a narrow Higgs width in comparison with its mass, this is calculated from the $2 \rightarrow 3$ process $qq \rightarrow qqH$ with W or Z bosons fusing to form the Higgs. The spin summed, squared matrix element for $q(p_1) + q'(p_2) \rightarrow q(p_3) + q'(p_4) + H$ is [39]

$$|\mathcal{M}|^2 = 128\sqrt{2}G_F^3 m_V^8 \frac{C_1^V p_1 \cdot p_2 p_3 \cdot p_4 + C_2^V p_1 \cdot p_4 p_2 \cdot p_3}{(2p_3 \cdot p_1 + m_V^2)^2 (2p_4 \cdot p_2 + m_V^2)^2} \quad (3.5)$$

where

$$\begin{aligned} C_1^W &= 1 \\ C_2^W &= 0 \\ C_1^Z &= \frac{1}{4} [(V_q - A_q)^2 (V_{q'} - A_{q'})^2 + (V_q + A_q)^2 (V_{q'} + A_{q'})^2] \\ C_1^Z &= \frac{1}{4} [(V_q - A_q)^2 (V_{q'} + A_{q'})^2 + (V_q + A_q)^2 (V_{q'} - A_{q'})^2] \end{aligned} \quad (3.6)$$

where V_q and A_q are defined in Eq. (2.2). The inclusive hadron-hadron cross section $\sigma(pp \rightarrow H + X)$ is obtained by convolving with appropriate PDF's, summing over flavours and integrating over three body phase space. Again, NLO QCD corrections have been calculated [40] and give a positive enhancement of about 10%.

Vector boson fusion has the fortuitous property that it has no coloured particles exchanged in the t -channel. Therefore there can be no secondary QCD radiation from the t -channel. We expect the t -channel subprocess to be devoid of soft hadrons generated from secondary radiation. This is a major theme of this thesis and will be fully explored in Chapter 4.

3.2.3 Associated Weak Boson Production

The cross sections are simply related to those for $e^+e^- \rightarrow ZH$ and are at LO [41]

$$\begin{aligned}\hat{\sigma}(q\bar{q}' \rightarrow WH) &= \frac{(G_F m_W^2)^2}{9\pi} |V_{qq'}|^2 \frac{p_W}{\sqrt{\hat{s}}} \frac{3m_W^2 + p_W^2}{(\hat{s} - m_W^2)^2} \\ \hat{\sigma}(q\bar{q} \rightarrow ZH) &= \frac{(G_F m_W^2)^2}{9\pi} (V_q^2 + A_q^2) \frac{p_Z}{\sqrt{\hat{s}}} \frac{3m_Z^2 + p_Z^2}{(\hat{s} - m_Z^2)^2},\end{aligned}\quad (3.7)$$

with

$$p_V^2 = \frac{1}{4\hat{s}} (\hat{s}^2 + m_V^4 + m_H^4 - 2\hat{s}m_V^2 - 2\hat{s}m_H^2 - 2m_V^2 m_H^2) \quad (3.8)$$

for $V = W, Z$. NLO corrections are the same as for Drell-Yan W or Z production and increase both cross sections by around 25%. The residual uncertainty is $\mathcal{O}(12\%)$.

This mode, although small, is important at the $p\bar{p}$ Tevatron due to its quark induced s -channel nature that increases the cross section with respect to a pp collider. The involvement of a final state weak boson enables one to utilise the dominant light Higgs $b\bar{b}$ decay mode as one is able to trigger on the weak bosons presence. The irreducible backgrounds $p\bar{p} \rightarrow Z, W + b\bar{b}$ are under control, being calculated at NLO and even implemented in the MCFM Monte-Carlo event generator [42].

3.2.4 Associated Top Production

This has a very distinctive signal in the detector, four b -jets! These are from $q\bar{q}, gg \rightarrow t\bar{t}H$ with $H \rightarrow b\bar{b}$. With good b -tagging capabilities this becomes an attractive alternative for Higgs masses close to the lower limit. It is for this reason, and for the fact that it enables measurement of the top Yukawa coupling, that it attracts attention despite its small rate. It is sensitive

to the top mass and induced by both gluons and quarks [43]. The NLO QCD corrections have been calculated recently [44–47]. They, unfortunately, *decrease* the cross section at the Tevatron by about 30%, but *increase* it at the LHC by about 20%. Although the calculational details are complex, the basic reason for this can be understood from the colour structure of QCD [48]. At the Tevatron, the dominant induction is from s -channel quark annihilation where the $t\bar{t}H$ system is thus in the colour octet state, whereas at the LHC, gluon induction is dominant and the final state is a mixture of colour octet and colour singlet states. The QCD Coulomb interaction between the top quark pair is repulsive for the octet state and attractive for the singlet. Therefore we expect many of the higher order corrections (caused by gluon exchange between the tops) to be negative for the Tevatron and positive for the LHC. For a complete discussion of this effect see [49].

3.3 Discovery Prospects at the Tevatron

At the time of writing, a pessimistic view is being taken concerning prospects for Higgs discovery at the Tevatron. The accelerator has not performed as well as originally expected and will deliver an integrated luminosity of only $3 - 10 \text{ fb}^{-1}$ before the first LHC results arrive. Figure 3.5 [50] shows why this is a problem. It shows predictions for the luminosity required to exclude, have evidence for and discover a Standard Model Higgs in the low mass range. It is for the associated weak boson production channel with decays to fermions. The errors are statistical only (systematics pushes them up) and the two sets are due to analyses performed in 1999 and 2003. Using the more recent predictions, in order to claim a 5σ discovery for a Higgs mass of 120 GeV, an integrated luminosity of 10 fb^{-1} is needed. However, in order to rule out

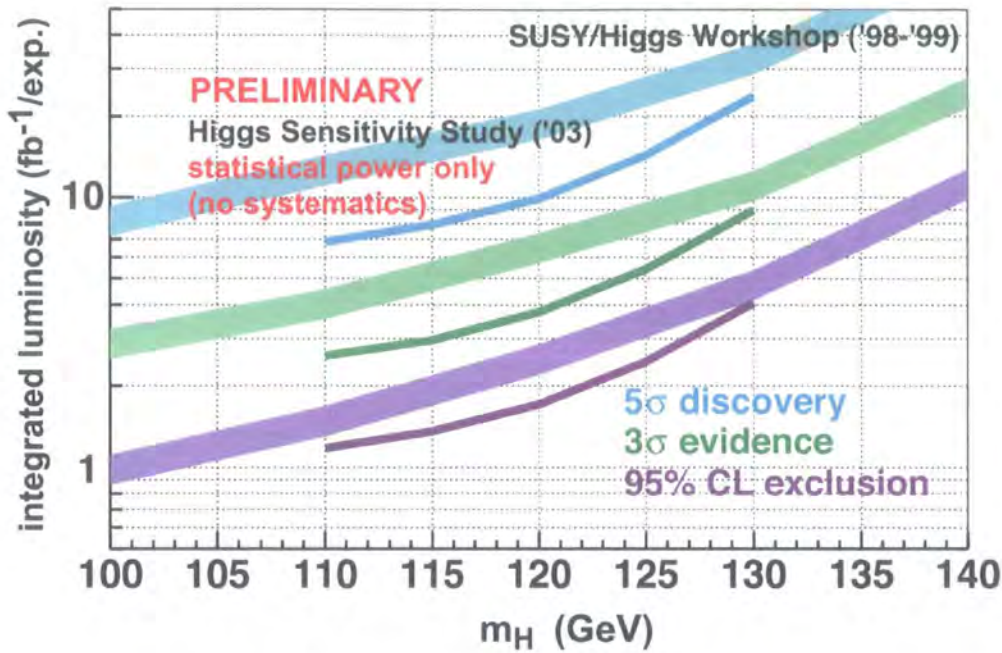


Figure 3.5: Tevatron Higgs discovery potential.

a Higgs at the LEP excess of 115 GeV, one only needs 1.5 fb^{-1} . Clearly the Tevatron will give very useful information, even if no discovery is claimed.

3.4 Discovery Prospects at the LHC

If the Higgs exists, it is most likely to be discovered at the LHC. Paradoxically, the lowest range of possible Higgs masses is a hard range in which to be sensitive. Figure 3.6 [51] shows total signal significance for a range of Higgs masses. It also shows this broken down into a selection of search channels. In the lowest region we see that there is no single channel that will produce adequate rates on its own. There are many assumptions both about the machine and the physics in this plot, however the conclusion can be drawn that the situation is not ‘cut and dried’. There is room for unforeseen eventualities, making the case for exploring other, more unusual channels, compelling.

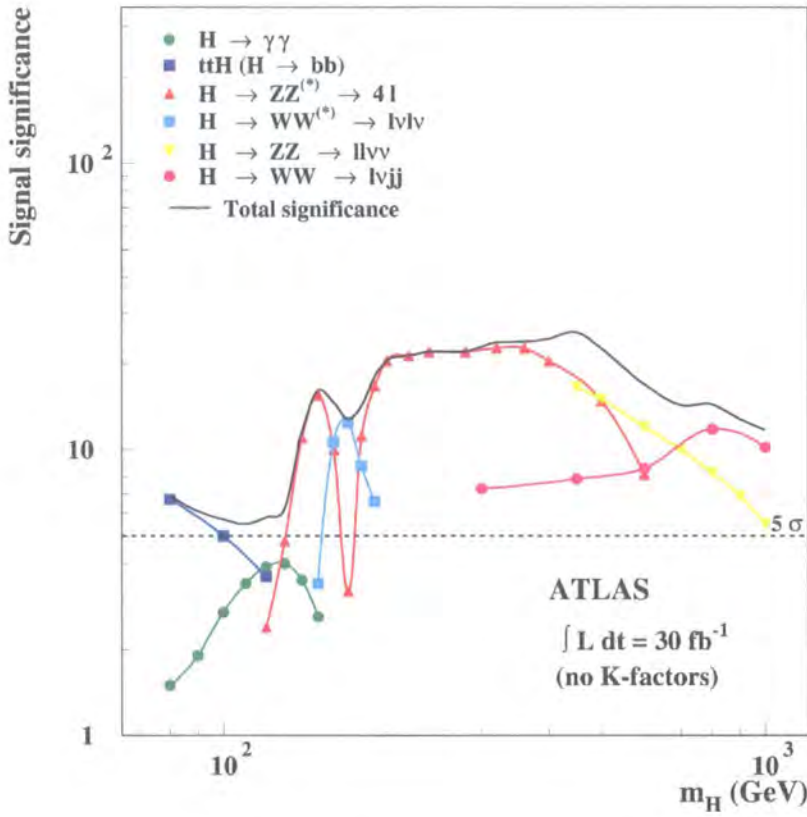


Figure 3.6: LHC Higgs discovery potential.

3.5 Higgs Production with Rapidity Gaps

In the previous sections we summarised the ‘mainstream’ channels for hadronic Higgs discovery. We have seen that all have problems and, especially for a light Higgs just above the LEP limit, detection will be challenging. There is no ‘golden channel’ with a large significance of signal over backgrounds. Rather there is a range of possibilities.

An often overlooked class of potential Higgs discovery channels are those that involve the kinematic phenomenon of a rapidity gap in the detector. These events have special properties and should be thoroughly investigated both in their own right and as a possibly vital Higgs search channel.

Naturally, we can only sketch the main ideas of this active field of study. For a full overview see, for example [52].

The *rapidity* of an object is defined as

$$y \equiv \frac{1}{2} \ln \left(\frac{E + p_z}{E - p_z} \right) \quad (3.9)$$

and is additive under Lorentz boosts. It thus fully describes longitudinal motion. In the case when $m \rightarrow 0$ this becomes equivalent to the experimentally more useful *pseudorapidity*

$$\eta \equiv -\ln \tan(\theta/2), \quad (3.10)$$

where θ is the angle from the beam direction.

In our definition, a *rapidity gap* is a total absence of hadrons within a region of rapidity. In order to display rapidity gaps, an event must have no colour exchanged in the t -channel between the initial state. If this does occur, there is necessarily radiation emitted that fills the gap with secondary

hadrons. Events that exhibit rapidity gaps are often called *diffractive*, although this refers more precisely to those cases when the object(s) exchanged in the t -channel carry no quantum numbers. An object carrying the quantum numbers of the vacuum is called a *Pomeron* - about which we know surprisingly little. There are various models that attempt to describe the Pomeron. Ideas include states composed of multiple perturbative gluons, data derived Pomeron parton density functions and others. Certainly, conventional QCD factorisation is completely unable to describe these events - something our community should be very concerned about as they are not rare, indeed diffractive events accounted for around 40% of scattering events at Tevatron run I!

3.5.1 Diffractive Higgs Production

Table 3.2 shows a particular picture of diffractive Higgs production. In both cases the Higgs is produced centrally in the detector. In the *exclusive* case, the protons scatter elastically and may be detected in the far-forward regions. In the *inclusive* case, the protons are allowed to dissociate, but their remnants are still far-forward and separated from any central decay products by large rapidity gaps. This is termed a jet-gap-jet configuration.

Perturbative QCD does not tell us how to calculate these types of processes, we are thus forced to resort to plausible models. There are four contemporary models - all of which adequately describe diffractive dijet production at the Tevatron [53] (run I)

- *Non-Factorisable Pomeron* [54]: Convolute standard hadron-hadron cross section with gluon distributions of the pomeron measured at HERA. Predictions are scaled to CDF dijet measurement.

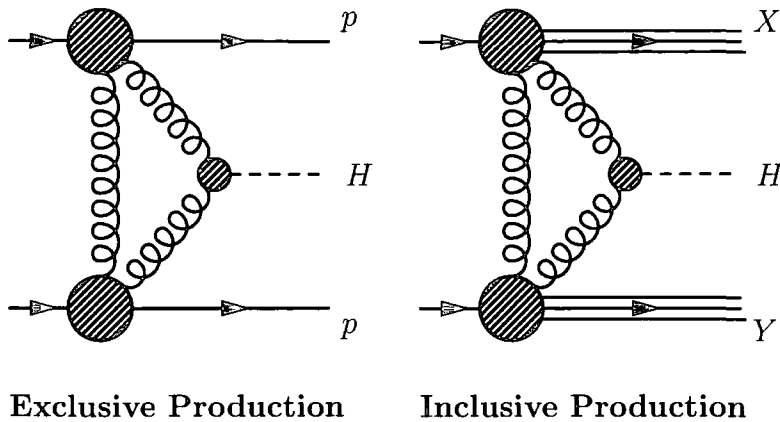


Table 3.2: Diffractive Higgs production.

- *Factorisable Pomeron* [55]: Diffractive gluon density factorises into a pomeron flux factor and a gluon density of the pomeron. Again, predictions are scaled to CDF dijet measurement.
- *Exclusive Proton* [56]: Calculate perturbatively using unintegrated⁴, skewed⁵ gluon distribution in the proton (no Pomeron).
- *Soft Colour* [57]: Colour Strings form and change the hadronisation process such that colour is ‘bleached out’. Uses Monte Carlo simulation (PYTHIA [58]) rather than analytic approach.

The final states considered in the models are not identical. Specifically, in the factorisable and non-factorisable Pomeron models, the centrally located Higgs decay products are accompanied by Pomeron remnants.

In the exclusive case, it is possible to tag the outgoing protons given addi-

⁴In a standard set of parton distribution functions, the transverse momentum of partons is neglected. *Unintegrated* parton distributions redress this and are under study at present.

⁵Looking at Tab. 3.2, the two gluons emitted from a proton do not have the same momentum (as we are creating a massive central system). More generally, when we construct a gluon ladder with unequal momenta flowing up and down each side, the distribution we use (signified by the large blobs) to select this configuration from the proton is called a *skewed* parton distribution.

tional detectors in the far-forward region. These need to be placed 40 – 50 m down the beampipe from the interaction point. Detectors such as these have been constructed and are currently functioning for CDF and DØ at the Tevatron (forward proton spectrometers) and are being actively considered for the CMS detector at the LHC (TOTEM experiment). They both will make extensive studies of all elastic scattering processes and, hopefully, shed some light on this mysterious aspect of strong interaction physics. These *roman pot* detectors will be able to, very accurately, measure the momentum of the scattered protons. This enables one to deduce the mass of the central system to an accuracy of approximately 1 GeV by equating it with any missing mass in the pp system. For our signal, this missing mass will be equal to the mass of the Higgs decay products, for example a central $b\bar{b}$ system. This strongly suppresses backgrounds. Unfortunately though, the cross section for exclusive production is very small. The proton form factors strongly limit the available phase space in the transverse momentum of the produced Higgs, $q_T \sim 1/R_p$, where R_p is the proton radius. Also, the cross section is suppressed at the parton level by QCD Sudakov-like radiative effects. This will be explained in the next Chapter.

The cross section is much higher in the inclusive case, where we let the protons dissociate. In this case there is no proton form factor suppression and the QCD ‘radiation damage’ is weaker. Backgrounds are also larger because we lose the ‘missing mass’ resolution method.

3.5.2 Spectator Effects and the Soft Survival Probability

What are the cross sections for these processes? We wish to trigger on an experimental rapidity gap. This is a delicate phenomenon whose survival not only depends on a calculation of the hard scattering process, but also on the possibility that spectator partons within the proton scatter. This is called *soft rescattering*.

Again we must resort to plausible models to calculate the probability that any gap produced in a hard scatter will survive soft rescattering. The effect can be described in terms of screening or absorptive corrections. This approach is originally due to Björken [59]. We assign an opacity, Ω , to the proton that is a function of the impact parameter, b_t between the two incoming hadrons. Then the probability, \hat{S}^2 , that there is no extra inelastic scattering is

$$\hat{S}^2 \equiv \frac{\int |\mathcal{M}(s, b_t)|^2 e^{-\Omega(b_t)} d^2 b_t}{\int |\mathcal{M}(s, b_t)|^2 N d^2 b_t}. \quad (3.11)$$

$\mathcal{M}(s, b_t)$ is the amplitude of the (elastic) process of interest (in impact parameter space) at a particular centre of mass energy \sqrt{s} . Therefore, the denominator in Eq.(3.11) is the cross section of the (diffractive) process we are considering. The factor $N = e^{-\Omega_0}$, where Ω_0 is the relevant opacity evaluated at $b_t = 0$, ensures \hat{S}^2 is properly normalised. The opacity, $\Omega(b_t)$, reaches a maximum in the centre of the proton and becomes smaller in the periphery. Thus, the exponent under the integral in the numerator accounts for the fact that at very small impact parameters the strong interaction is really strong and the process is practically screened by shadowing effects, while at large impact parameters (at the proton periphery) the screening effects are weak. Therefore, the survival probability depends on the spatial distribution of the

constituents of the relevant subprocess.

In this thesis we use an extension of this model due to Khoze, Martin and Ryskin [60]. This is a *two channel eikonal model*. Having two channels allows us to take into account the possibility that the proton becomes excited as an intermediate state in the scattering. The opacity, $\Omega(b_t)$ becomes a matrix and the relative spacing of the eigenvalues controls the amount of inelastic diffraction. This is because the two diffractive eigenstates have different absorptive cross sections. We are thus allowed us to consider inelastic processes such as all those in this thesis.

This picture, based on parameterisations of soft physics, introduces model dependence into any calculation. However, in certain cases, one is able to identify two processes with the same soft physics, i.e. the constituents of the proton involved in the hard scatter are identical. Such an appropriate monitoring process for the double-diffractive mechanism (where two gaps are observed between forward jets) is central dijet production with a rapidity gap on either side. To date, a check has been the prediction of diffractive dijet production at the Tevatron in terms of the diffractive structure functions measured at HERA [53]. The evaluation of the survival factor, \hat{S}^2 , based on the formalism of [60,61] appears to be in agreement with the CDF data (see also [62,63]) although the run I data is not of high quality. We expect that future measurements in run II of the Tevatron will provide us with further detailed information on \hat{S}^2 .

In the exclusive proton model, for the LHC with $m_H = 120$ GeV, $\sigma(pp \rightarrow p + H + p) \simeq 3$ fb [64]. This translates to a signal rate of 90 events (assuming an integrated luminosity of 30 fb^{-1}) with a signal to QCD background ratio

of

$$\frac{S(H \rightarrow b\bar{b})}{B(b\bar{b})} \geq 15 \left(\frac{250 \text{ MeV}}{\Delta M} \right) \quad (3.12)$$

where ΔM is the experimental missing mass resolution. The rate at the Tevatron is far too low to be measurable.

Table 3.3 shows final predictions from each of the four models outlined above. Again, it should be emphasised that in the factorisable and non-factorisable models the central region is populated not only by Higgs decay products, but also Pomeron remnants. Thus, no direct comparison should be made between these and the other predictions. We merely intend to give the reader an impression of current estimations of the typical rates for rapidity gap processes involving the production of a Higgs.

	SCI	Exclusive Proton	Factorisable Pomeron	Non-Factorisable Pomeron
Tevatron	< 0.01	0.3	0.02	2.7
LHC	0.2	3	6	320

Table 3.3: Diffractive Higgs cross sections predictions for $m_H = 120$ GeV in fb.

3.5.3 Electroweak Production with Rapidity Gaps

A possibility that exploits the advantages of a clean rapidity gap signal, but is not plagued by small cross sections is when the hard subprocess is not mediated by strong processes, but by electroweak ones. This is the subject of the next Chapter. We do not need to resort to models of colour singlet strong interaction physics as perturbative calculations of the electroweak interactions are well defined. As we mentioned earlier, electroweak Higgs production (with or without gaps) is of particular importance as it allows a determination of its coupling to vector bosons.

We will also see that we can calibrate our soft rescattering model to a similar electroweak process, namely Z production - where we know precisely the mass of the central system. Thus we will provide watertight predictions that are completely free of model dependence and able to compete with the mainstream channels.

Our channel enables us to utilise the light Higgs dominant $b\bar{b}$ decay mode [65]. In the light of the LEP excess and the fact that the minimal supersymmetric extension of the Standard Model requires that the Higgs have a mass less than 135 GeV [66], this method could prove to be of crucial importance.

Chapter 4

Higgs Production via Vector Boson Fusion in Rapidity Gap Events and its Calibration

In this Chapter we will calculate Higgs, W and Z production accompanied by two forward jets with rapidity gaps. This will be performed from first principles using the helicity method of calculating matrix elements. To do this we will make use of the automation routines MadGraph and HELAS. We will then use leading logarithm QCD to calculate the probability of keeping parton level rapidity gaps - i.e. suppress QCD radiation from the hard process. Finally, we use the model of [60] to estimate the hadron level gap survival probability. Our results can be viewed in two ways; absolute (but model dependent) cross section predictions for the LHC, or alternatively a Higgs signal and a calibration process that, when used together in an experimental analysis, can eliminate model dependence introduced during the calculation.

We wish to obtain from our field theoretic parton level calculations not

only total cross sections, but also final state kinematic distributions. We thus need to generate final state momenta at random and weight these by the spin summed, squared matrix element for the process being considered. The number of diagrams is large enough to warrant automation of the matrix element evaluation¹. This will become crucial when we consider QCD backgrounds, where the number of diagrams is truly huge. In Chapter 1 we used the trace technique to sum and square amplitudes in order to obtain a cross section. We will now outline another, computationally advantageous method that involves squaring amplitudes then summing them - the helicity method.

4.1 Helicity Amplitude Techniques

The helicity method [67–69] is an elegant and efficient means of calculating amplitudes in field theory particularly in situations where all external states are massless. A full introduction can be found in [70].

As a result of their external masslessness, amplitudes can be split into separate expressions for each definite final and initial state helicity. Massless spinors of helicity $\lambda = \pm 1$ are thus expressed in a Weyl basis

$$\begin{aligned} |p\pm\rangle &= \frac{1}{2}(1 \pm \gamma_5)u(p) = \frac{1}{2}(1 \mp \gamma_5)v(p) \\ \langle p\pm| &= \bar{u}(p)\frac{1}{2}(1 \mp \gamma_5) = \bar{v}(p)\frac{1}{2}(1 \pm \gamma_5). \end{aligned} \quad (4.1)$$

Note that we choose positive and negative energy solutions of the massless Dirac equation to be equal. This can be done for definite helicity solutions because the projection operators, $\Lambda_+(p) \sim u(p) \otimes \bar{u}(p)$ and $\Lambda_-(p) \sim v(p) \otimes$

¹Apart from Higgs production where there is only one diagram and thus a simple analytic expression.

$\bar{v}(p)$, are both proportional to \not{p} in the massless limit.

4.1.1 Colour Decomposition

The splitting into simpler *partial amplitudes* is achieved by the *colour decomposition* of the full amplitude. In order to show this, we express all QCD colour factors in terms of the generators, T^a . For notational convenience, we change the normalisation of these with respect to those presented in Section 1.2.1 by now requiring $\text{Tr}(T^a T^b) = \delta^{ab}$. Then we re-express the structure constants as

$$f^{abc} = -\frac{i}{\sqrt{2}} [\text{Tr}(T^a T^b T^c) - \text{Tr}(T^a T^c T^b)]. \quad (4.2)$$

If any external quarks are present, then in addition to these traces there will be some strings of T^a 's terminated by fundamental indices, of the form $(T^{a_1} \dots T^{a_m})_{i_2}^{\bar{i}_1}$. To reduce the number of traces and strings we Fierz rearrange the contracted T^a 's using

$$(T^a)_{i_1}^{\bar{j}_1} (T^a)_{i_2}^{\bar{j}_2} = \delta_{i_1}^{\bar{j}_2} \delta_{i_2}^{\bar{j}_1} - \frac{1}{N_c} \delta_{i_1}^{\bar{j}_1} \delta_{i_2}^{\bar{j}_2}. \quad (4.3)$$

For example, applying equation (4.2) to the amplitude for tree level n -gluon scattering we colour decompose it into a sum of single trace terms

$$\mathcal{A}_n^{\text{tree}}(\{k_i, \lambda_i, a_i\}) = g^{n-2} \sum_{\sigma \in S_n/Z_n} \text{Tr}(T^{a_{\sigma(1)}} \dots T^{a_{\sigma(n)}}) A_n^{\text{tree}}(\sigma(1^{\lambda_1}), \dots, \sigma(n^{\lambda_n})), \quad (4.4)$$

where $A_n^{\text{tree}}(1^{\lambda_1}, \dots, n^{\lambda_n})$ are the *partial amplitudes* which contain all kinematic information and are separately gauge invariant. S_n is the set of all permutations of n objects and Z_n is the subset of all cyclic permutations (which preserves the trace). Thus we sum over non-cyclic permutations of

the external gluons.

Similarly, applying equations (4.2) and (4.3), tree amplitudes with two external quarks can be reduced to single strings of T^a matrices,

$$A_n^{\text{tree}} = g^{n-2} \sum_{\sigma \in S_{n-2}} (T^{a_{\sigma(3)}} \dots T^{a_{\sigma(n)}})_{i_2}^{\bar{j}_1} A_n^{\text{tree}}(1^{\lambda_1}, 2^{\lambda_2}, \sigma(3^{\lambda_3}), \dots, \sigma(n^{\lambda_n})), \quad (4.5)$$

where numbers without subscripts refer to gluons. The extension of this colour decomposition to loop level is straightforward. At the one-loop level both single and *double* trace structures are generated.

It turns out that we do not need to compute every partial amplitude as they are related to each other by symmetries such as parity (which allows one to simultaneously reverse all helicities) and charge conjugation (which allows one to exchange a quark and antiquark, or equivalently flip the helicity on a quark line). For example, the five-gluon amplitude has only four independent tree-level partial amplitudes, two of which vanish, and there is a group theory relation between the last two. It is worth explaining this relation. It derives from the fact that the tree colour decomposition, Eq. (4.4), is equally valid for $U(N_c)$ as it is for $SU(N_c)$, but any amplitude containing the extra $U(1)$ photon must vanish. Hence if we substitute the $U(1)$ generator (the identity matrix) into the right hand side of Eq. (4.4), and collect the terms with the same remaining colour structure, that linear combination of partial amplitudes must vanish. This gives

$$0 = A_n^{\text{tree}}(1, 2, 3, \dots, n) + A_n^{\text{tree}}(2, 1, 3, \dots, n) + A_n^{\text{tree}}(2, 3, 1, \dots, n) + \dots + A_n^{\text{tree}}(2, 3, \dots, 1, n), \quad (4.6)$$

often called a *photon decoupling equation* or *dual Ward identity*².

4.1.2 Spinor Product Formalism

We use the spinor product formalism to calculate the colour decomposed partial amplitude. This is an entirely kinematic object. We introduce a shorthand for the spinors of Eq. (4.1)

$$|i^\pm\rangle \equiv |p_i \pm\rangle, \quad \langle i^\pm| \equiv \langle p_i \pm|. \quad (4.7)$$

Each partial amplitude can be expressed in terms of products of these spinors

$$\begin{aligned} \langle ij\rangle &\equiv \langle i^-|j^+\rangle = -\langle j^-|i^+\rangle \\ [ij] &\equiv \langle i^+|j^-\rangle = -\langle j^+|i^-\rangle \\ 0 = \langle ii\rangle &= [ii] = \langle i^-|j^-\rangle = -\langle i^+|j^+\rangle \end{aligned} \quad (4.8)$$

Note the antisymmetry of the products. They are, up to a phase, square roots of Lorentz products

$$\langle ij\rangle [ji] = s_{ij} \equiv (p_i + p_j)^2. \quad (4.9)$$

We also have the following useful identities:

Gordan identity and projection operator:

$$\langle i^\pm|\gamma_\mu|i^\pm\rangle = 2p_i^\mu, \quad |i^\pm\rangle\langle i^\pm| = \frac{1}{2}(1 \pm \gamma_5)\not{p}_i \quad (4.10)$$

²Because it can be derived from string theory, a.k.a. dual theory.

Fierz rearrangement:

$$\langle i^+ | \gamma^\mu | j^+ \rangle \langle k^+ | \gamma_\mu | l^+ \rangle = 2 [ik] \langle lj \rangle \quad (4.11)$$

charge conjugation of current:

$$\langle i^+ | \gamma^\mu | j^+ \rangle = \langle i^- | \gamma^\mu | j^- \rangle \quad (4.12)$$

Schouten identity:

$$\langle ij \rangle \langle kl \rangle = \langle ik \rangle \langle jl \rangle + \langle il \rangle \langle kj \rangle. \quad (4.13)$$

In an n -point amplitude, momentum conservation provides one more identity,

$$\sum_{\substack{i=1 \\ i \neq j, k}}^n [ji] \langle ik \rangle = 0. \quad (4.14)$$

Our final ingredient is a spinor representation for the polarisation vector for a massless gauge boson of definite helicity

$$\varepsilon_\mu^\pm \equiv \pm \frac{\langle q^\mp | \gamma_\mu | k^\mp \rangle}{\sqrt{2} \langle q^\mp k^\pm \rangle}, \quad (4.15)$$

where k is the vector boson momentum and q is an auxiliary vector called the reference momentum, reflecting the freedom of on-shell gauge transformations. A judicious choice of the q_i can simplify a calculation substantially

by making many terms and diagrams vanish, due to the following identities

$$\begin{aligned}
 \varepsilon_i^\pm(q) \cdot q &= 0 \\
 \varepsilon_i^+(q) \cdot \varepsilon_j^+(q) &= \varepsilon_i^-(q) \cdot \varepsilon_j^-(q) = 0 \\
 \varepsilon_i^+(k_j) \cdot \varepsilon_j^-(q) &= \varepsilon_i^+(q) \cdot \varepsilon_j^-(k_i) = 0 \\
 \not{\varepsilon}_i^+(k_j)|j^+ \rangle &= \not{\varepsilon}_i^-(k_j)|j^- \rangle = 0 \\
 \langle j^+|\not{\varepsilon}_i^-(k_j) &= \langle j^-|\not{\varepsilon}_i^+(k_j) = 0.
 \end{aligned} \tag{4.16}$$

We can now express any partial amplitude with massless external fermions and vector bosons in terms of spinor products. Since these products are defined for both positive and negative energy four momenta, we can use crossing symmetry to extract a number of scattering amplitudes from the same expression, by exchanging which momenta are outgoing and which incoming. However, because the helicity of a positive energy (negative energy) massless spinor has the same (opposite) sign as its chirality, the helicities assigned to the particles - bosons as well as fermions - depend on whether they are incoming or outgoing. Our convention is to label particles with their helicity when they are considered outgoing (positive energy); if they are incoming the helicity is reversed.

4.1.3 MadGraph / HELAS

HELAS (HELicity Amplitude Subroutines) [71] is a set of FORTRAN77 routines which automate the various parts of a tree level partial amplitude calculation. There are three classes of routine: wave-functions, propagators and vertex factors.

An example of a wave-function routine is IXXXXX which is called as follows

`call IXXXXX(p1, fmass, nhf, nsf, fi)`

and takes as input a four-momentum, $\mathbf{p1}$, a mass, \mathbf{fmass} , a helicity, $\mathbf{nhf} = \pm 1$ and a particle-antiparticle switch, $\mathbf{nsf} = \pm 1$ and returns a complex 6-vector, \mathbf{fi} , representing the wave function of a flowing-in fermion. The first (second) two components contain the chirality left (right) part of the spinor

$$\begin{pmatrix} \mathbf{fi}(1) \\ \mathbf{fi}(2) \end{pmatrix} = |i^-\rangle, \quad \begin{pmatrix} \mathbf{fi}(3) \\ \mathbf{fi}(4) \end{pmatrix} = |i^+\rangle. \quad (4.17)$$

The last two components contain the four-momentum along the fermion number flow,

$$\begin{pmatrix} \mathbf{fi}(5) \\ \mathbf{fi}(6) \end{pmatrix} = \mathbf{nsf} \begin{pmatrix} \mathbf{p}(0) + i\mathbf{p}(3) \\ \mathbf{p}(1) + i\mathbf{p}(2) \end{pmatrix}. \quad (4.18)$$

Similarly, the routines `OXXXXX` calculates an outgoing fermion wave function, `VXXXXX` calculates the wavefunction of an external vector boson and `SXXXXX` calculates that of an external scalar.

An example of a propagator routine is `FVOXXX`, which is invoked as

`call FVOXXX(fo, vc, g, fmass, fwidth, fvo)`

and computes a complex six-vector representing an off-shell fermion, \mathbf{fvo} , from the interaction of a vector boson, \mathbf{vc} , with a flowing-out fermion, \mathbf{fo} .

An example of a vertex factor routine is `IOVXXX`, called as

`call IOVXXX(fi, fo, vc, g, vertex)`

and takes as input a complex six-vector, \mathbf{fi} , representing a flowing-in fermion, a complex six-vector, \mathbf{fo} , representing a flowing-out fermion, a complex six-vector, \mathbf{vc} , representing a vector boson and a real two-vector, \mathbf{g} , containing

the fermion-boson coupling³. It returns a complex number, `vertex`, which is the amplitude of the fermion-fermion-vector vertex including the coupling.

A complete description of all the routines and conventions can be found in [71].

MadGraph [72, 73] knits these routines together to form helicity amplitudes and hence matrix elements. The user gives MadGraph a $2 \rightarrow n$ process. MadGraph then divides the problem of generating helicity amplitudes into four main parts. Firstly, all distinct tree level topologies are generated. Secondly, particles are inserted into these topologies to produce all Feynman diagrams for the specified process. Thirdly, the colour and symmetry factors associated with each diagram are calculated. Finally, the HELAS code is generated.

The topologies are generated using a simple recursive formula. The program begins with the one possible topology for a process with three external legs. By adding an additional leg in turn to the legs of the three topology, and to the three point vertex, the four topologies for four external particles are generated. The twenty-five topologies for five external particles are generated by adding one external leg to each of the lines and three vertices of the four particle topologies. This process is continued to generate topologies for up to ten external particles.

Once the topologies have been generated, the external legs are assigned to particles requested by the user. From here, each vertex which has only one unspecified line is checked to determine if the current model allows such a vertex, and if so what particle the unspecified line must correspond to. If more than one particle is possible, this is noted and the other choices tried later. The process is continued until either all of the lines are specified and the

³ $g(1)$ ($g(2)$) contains the coupling of a chirality left (right) fermion.

graph is stored, or a vertex is reached for which there is no possible coupling in the model and the graph is discarded. All of the graphs which are stored are then checked to assure they are of the correct order in the appropriate couplings. The advantage of this scheme is twofold. First it is extremely fast. Hundreds of diagrams can be generated in a fraction of a second. Second, it is amenable to extension to models other than the Standard Model, one just needs to specify the vertices. We will do this in Chapter 6.

The symmetry factor for the interchange of two identical fermions is determined by following all of the fermion lines and seeing which external particles are attached by a line. Then one combination is assigned to be the positive orientation. All other graphs will be compared to this positive orientation to determine how many permutations are required to get from one configuration to the other. Each permutation results in a factor of -1 . The colour factors are determined by first assigning the appropriate colour matrix at each vertex and then applying the completeness relations as colour lines are summed over. This is the part of the program that is most costly in computer time.

Generating the HELAS code for each diagram completes the process. External wave functions are generated first and then the vertices with only one leg left uncalculated are used to calculate the wave function for that leg. The process is continued until all of the legs are calculated and the last vertex gives the amplitude for the graph. MadGraph simply looks at the vertices and depending on what type of particles are in the vertex writes out an appropriate HELAS call. The code is optimised by making sure no redundant calls are made.

An ancillary, but extremely useful feature of MadGraph is that it generates in addition to the HELAS routine a PostScript™ file containing all stored diagrams and the number of the amplitude they correspond to.

The FORTRAN function containing the HELAS calls is embedded in a function that calls it for every set of external helicities (even ones that are zero) and sums over them. Thus a call to this summed function, for example

```
me2 = SUD_UDZ(p1,p2,p3,p4,p5)
```

will return, for an input of external four momenta p_1, p_2, p_3, p_4, p_5 , a double precision float representing the spin summed, squared matrix element for that point in phase space.

4.2 Phase Space Integration

In order to produce total and differential cross sections we need, in addition to the matrix element for the process, a weight for each point in phase space and a method of integrating over it. As we wish to produce results for the LHC, we must also integrate over the parton distributions. Put more succinctly, we must numerically integrate a multi-dimensional function.

The differential cross section for $2 \rightarrow n$ scattering is

$$d\sigma = (2\pi)^4 \delta^{(4)}(P_f - P_i) \frac{1}{2E_1 2E_2 |\mathbf{v}|} \times \left(\prod_f \frac{d^3 p_f}{(2\pi)^3 2E_{p_f}} \right) |\mathcal{M}_{fi}|^2 f_{p_1}(x_1, Q^2) dx_1 f_{p_2}(x_2, Q^2) dx_2, \quad (4.19)$$

where the terms before the fraction enforce momentum conservation, the fraction is the flux factor, the terms in large brackets each represent differential phase space for each final state particle and the matrix element is followed by differential parton distributions. One momentum integration can be eliminated using the delta function. In order to perform the other integrations we change variables - eliminating the four momenta in favour of final

state parton energies, E_{p_f} and the polar and azimuthal angles for each final state parton, θ_{p_f} and ϕ_{p_f} . They are then rescaled such that the integration limits are 0 and 1. A little thought is needed to realise an efficient rescaling of the differential parton distributions.

In the processes of interest to us, we wish to create a massive boson from our partons. Therefore

$$x_1 x_2 > \epsilon = \frac{M^2}{s}. \quad (4.20)$$

We choose our new variables y_i to satisfy this condition

$$x_1 = \epsilon^{y_1 y_2}, \quad x_2 = \epsilon^{(1-y_1)y_2}. \quad (4.21)$$

Then the integral over parton momentum fractions becomes

$$\int_0^1 dx_1 dx_2 \rightarrow A \int_0^1 dy_1 dy_2, \quad (4.22)$$

where

$$A \equiv y_2 \epsilon^{y_2} \ln^2 \epsilon \quad (4.23)$$

is the contribution to the phase space weight from the variable change. This procedure ensures that every part of the integration domain contributes to the integral.

4.2.1 Monte Carlo Integration and Importance Sampling

There are many algorithms for numerically evaluating one dimensional integrals, for instance the trapezoidal rule, Simpson's rule and Gaussian quadrature (a comprehensive discussion can be found in [74]). However, these are

highly inefficient (if they work at all) in estimating higher dimensional integrals. It is in this regime that the Monte Carlo method succeeds. Like the other routines, it relies on the fact that the average value of a function is given by the integral over a domain divided by its volume (area in 1-d)

$$\langle f(x) \rangle_{x \in [a,b]} = \frac{\int_a^b dx f(x)}{b-a}. \quad (4.24)$$

Thus we evaluate the integral at pseudo-random points in the interval. As long as the distribution of random numbers is flat, the central limit theorem guarantees convergence to the integral

$$\int_a^b f(x) dx = l \langle f \rangle \pm l \sqrt{\frac{\langle f^2 \rangle - \langle f \rangle^2}{N}}, \quad (4.25)$$

where $l \equiv b - a$ the length of the interval, and

$$\langle f \rangle = \frac{1}{N} \sum_{i=1}^N f(x_i), \quad \langle f^2 \rangle = \frac{1}{N} \sum_{i=1}^N f^2(x_i). \quad (4.26)$$

So we see that the error estimate behaves as $N^{-1/2}$ in one dimension. This is slower than other methods. If we now consider a multidimensional integral, the error estimate using the trapezoidal method behaves as $\mathcal{O}(N^{-2/D})$ and that of Simpson's rule is slightly faster at $\mathcal{O}(N^{-4/D})$. However the Monte Carlo method still behaves according to the central limit theorem and its error estimate goes as $N^{-1/2}$ for any value of D . The generalisation of Eq. (4.25) to D -dimensions is straightforward

$$\int_V d\Omega f = V \langle f \rangle \pm V \sqrt{\frac{\langle f^2 \rangle - \langle f \rangle^2}{N}}. \quad (4.27)$$

The convergence of the method can be improved by reducing the variance

of the function, $\sigma^2 = \langle f^2 \rangle - \langle f \rangle^2$. This can be achieved by transformations of the coordinates in which f is expressed and is called *importance sampling*. The name is indicative of the fact that doing this corresponds to sampling the integrand where it contributes most to the integral. To illustrate how this works, let us return to one dimension and rewrite the integral

$$\int_a^b dx f(x) = \int_a^b dx g(x) \left(\frac{f(x)}{g(x)} \right) \equiv \int_a^b dx g(x) h(x) \quad (4.28)$$

where the aim is to find an $h(x)$ that is more slowly varying than $f(x)$ and thus reduce the variance. In order to effect the improvement, one changes the integration variable

$$\int_a^b dx g(x) h(x) = \int_{G(a)}^{G(b)} dy h[G^{-1}(y)] \quad (4.29)$$

where $dG(x)/dx = g(x)$. Now if we evaluate this integral by pseudo-randomly sampling in the variable y , our result will converge faster. It can now be shown that an optimal choice for $g(x)$ is one that is proportional to $|f(x)|$, for details see [75]. We will make use of a standard package for performing the integrals, **VEGAS** [76]. This is an *adaptive Monte Carlo* algorithm that seeks out the parts of the integrand that contribute most and samples these more often - effectively importance sampling the integral, but numerically rather than finding an analytic function $g(x)$. For longevity and sheer value per code line, **VEGAS** is pretty much unbeatable, however it cannot deal with certain integrand structures. For example, if the integrand is localised along the main diagonal of an D -dimensional hypercube, $[0, \dots, 0]$ - $[1, \dots, 1]$, **VEGAS** will not converge. This is because it relies on a fixed coordinate system to slice the hypercube domain by subdividing the hypercube axes. Also one

must be careful to avoid any poles in the integrand. With these caveats most problems are amenable to solution using VEGAS.

Random Number Generators

We need a source of random numbers in order to sample our integrand. We are not able to rely on a truly random natural process, such as radioactive decays, as the following criteria must be satisfied. Firstly, speed; we must be able to produce of the order of 10^{12} numbers per second. There are few natural processes that have this rate of output. Secondly, reproducibility; a truly random process will never repeat the same sequence of numbers. This is actually a liability as the debugging process benefits greatly from being able to input exactly the same sequence. We therefore use a pseudo-random number generating algorithm that is able to provide the sequence on-the-fly. There are many algorithms of this type that produce sequences of numbers uniformly distributed in the interval $[0, 1]$. Typically, they use integers internally, are cyclic with period 2^n and only produce a real number at the end by dividing by the period size. A modern generator has a period of at least 2^{64} . The particular generator used in this work is a Marsaglia shift register [77]. This is very fast as it only uses logical bit operations to manipulate the integers.

4.3 Parton Level Calculation of Higgs, Z and W production

In the remainder of this Chapter, we perform the explicit calculations. These were executed using code written by the author that utilise matrix ele-

ments generated by MadGraph in the manner described in the previous two Sections. The IPPP 80-node Intel Pentium IVTM cluster, running under RedHatTM Linux 7.3 provided the necessary computational power.

We begin by considering the fundamental signal process, $\mathcal{O}(\alpha_W^3)$ Higgs production by WW , ZZ fusion: $qq \rightarrow qqH$ (Fig. 4.1). We assume that the Higgs is light, so that the dominant decay is into the $b\bar{b}$ final state. Because the momentum transfer is much smaller than the energy of the struck quark jets ($\langle p_T \rangle \sim M_{W/Z}$), the jets are produced predominantly at small angle (i.e. large rapidity). Note that there is no exchange of colour in the t -channel, which leads to a suppression of hadronic radiation in the central region between the forward jets as discussed in Chapter 3.

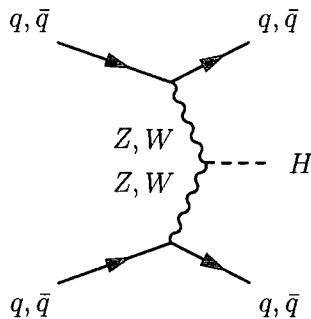


Figure 4.1: Higgs production via electroweak vector boson fusion.

Representative Feynman diagrams for the analogous $\mathcal{O}(\alpha_W^3)$ Z production process, $qq \rightarrow qqZ$ and $q\bar{q} \rightarrow q\bar{q}Z$ are shown in Fig. 4.2. They were first analysed in [78, 79]. Note that in addition to the WW fusion diagram, Fig. 4.2(a), the Z can also be radiated off either of the incoming or outgoing quark lines, Figs. 4.2(b) and (c). The characteristic topology of (b) is of a Z preferentially produced in the forward or backward region close in rapidity to one of the final-state quark jets. Requiring *centrally* produced Z decay products tends to suppress this contribution. Process (c) corresponds to s -channel production of the final-state $q\bar{q}$ pair, with the Z boson emitted

off the incoming quark lines. It does not correspond to t -channel colour singlet exchange and is heavily kinematically suppressed by requiring a large rapidity separation between the jets.

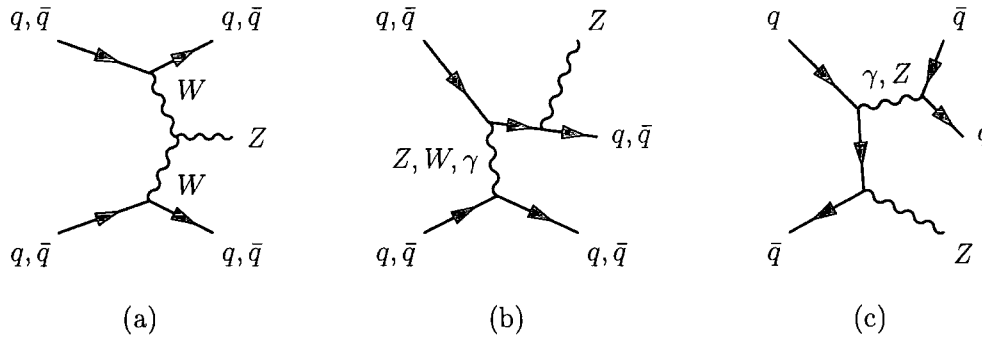


Figure 4.2: The three topologies for Zqq production via electroweak vector boson exchanges.

Similar remarks apply to W production. Representative Feynman diagrams for $qq \rightarrow Wqq$ are shown in Fig. 4.3. Note that the central W -production via γ exchange corresponding to Fig. 4.3a was recently discussed in [56]. The above $\mathcal{O}(\alpha_W^3)$ H and Z production processes both therefore

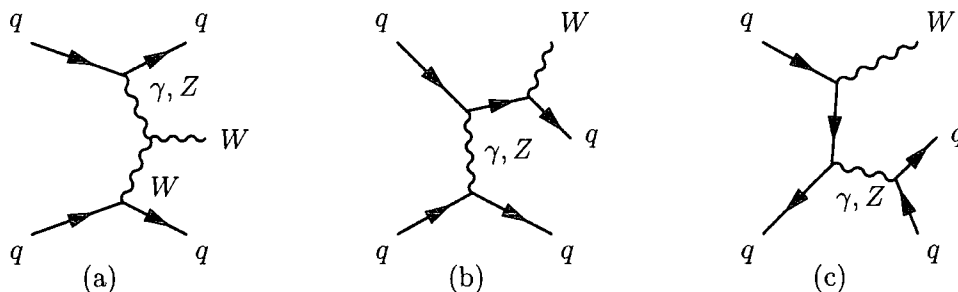


Figure 4.3: The three topologies for Wqq production via electroweak vector boson exchanges.

give rise to rapidity gap signatures between the forward jets and the central H and Z decay products. However there is a potentially important QCD $\mathcal{O}(\alpha_s^2 \alpha_W)$ background contribution to $Z + 2$ jet production where the internal electroweak gauge boson is replaced by a *gluon*. More generally, at this order indistinguishable background contributions can arise from any $2 \rightarrow 2$

scattering process (other than $gg \rightarrow gg$) where the Z is radiated off a quark line. Representative Feynman diagrams are shown in Fig. 4.4. By selecting forward jets and central Z bosons, in order to mimic the dominant Higgs configuration, the t -channel momentum transfer is minimised, and these QCD processes split into two types: t -channel quark (Figs. 4.4(a,b,c)) and gluon exchange (Figs. 4.4(d)). Requiring rapidity gaps therefore suppresses both type of contribution, as will be discussed in Section 4.4. Finally, given that we

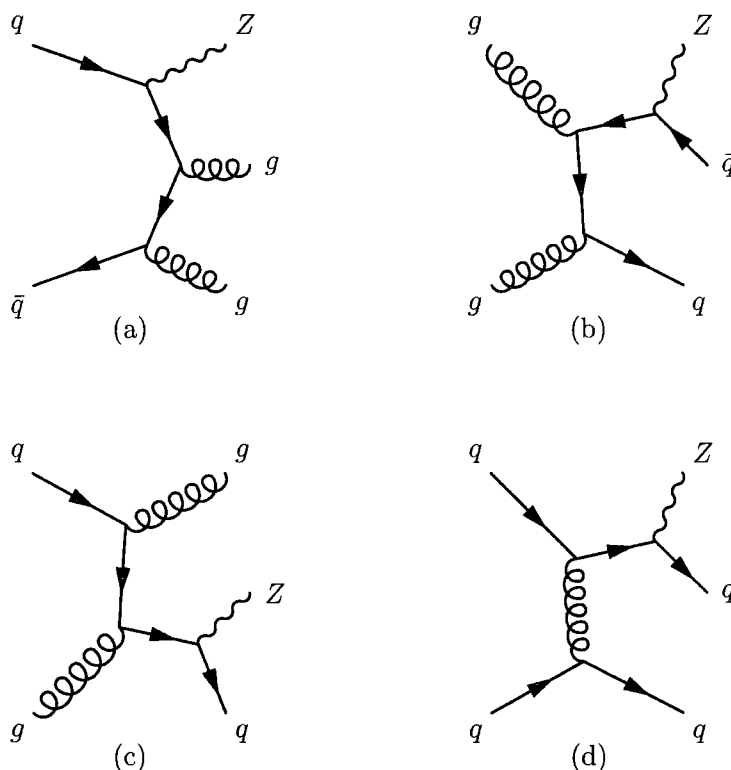


Figure 4.4: QCD background $Z + 2$ jet production processes.

are interested in the $b\bar{b}$ decay modes of both the Higgs and Z bosons, with two additional jets in the final state, there is a class of $\mathcal{O}(\alpha_s^4)$ pure-QCD background processes of the form $ab \rightarrow cd + b\bar{b}$ with $a\dots d = q, g$, examples of which are shown in Fig. 4.5. We will consider their corresponding cross sections, with the additional requirement that $m_{b\bar{b}} \simeq m_Z$.

We have in mind final states with a jet registered in a forward detector

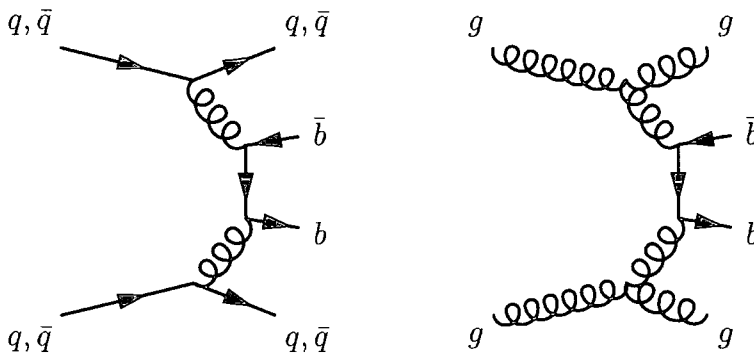


Figure 4.5: Continuum QCD backgrounds to $qq \rightarrow qq(H, Z)$, $(H, Z) \rightarrow b\bar{b}$.

with pseudorapidity $\eta_1 > \eta_{\min}$, another produced backwards with $\eta_2 < -\eta_{\min}$, and the H , Z and W decay products produced centrally, with rapidity $|y_{H,Z,W}| < y_{\max}$. We impose a minimum transverse momentum cut $p_{T\min}$ on *both* final-state jets (we do not yet include $b\bar{b}$ decay of the Higgs).

4.3.1 Total cross sections

Figure 4.6 shows the total cross section for Higgs, electroweak Z and W , and QCD Z production (with no branching ratios included) as a function of a cut on the minimum transverse jet momentum $p_{T\min}$. The Higgs mass is $m_H = 115$ GeV and the leading-order MRST98LO [80] parton distribution set is used, as we are performing a leading order calculation. Note that only for H production is the cross section finite in the limit $p_{T\min} \rightarrow 0^4$. In addition, the possibility that the final state jets in Z and W production originate in the splitting process $g^*, \gamma^* \rightarrow q\bar{q}$ (for example, see Fig. 4.2(c)) requires a jet separation cut. The minimal way to do this is simply to require that one of the jets is produced in the forward hemisphere and the other in the backward hemisphere, i.e. $\eta_1 \cdot \eta_2 < 0$. When we come to consider

⁴The possibility of exchanging a massless photon or gluon in the t channel gives rise to an infrared singularity in the electroweak and QCD $Z + 2$ jet production processes as $p_{T\min} \rightarrow 0$, see Figs. 4.2 and 4.4.

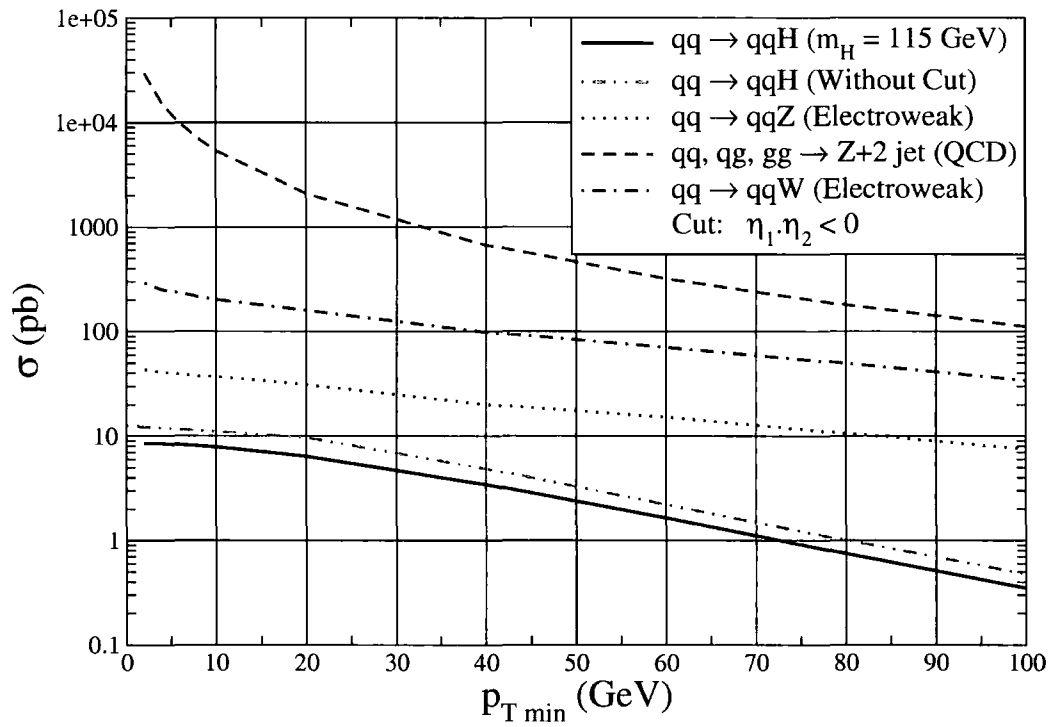


Figure 4.6: Total cross sections for (H , Z , W) +2 jet production at the LHC.

‘realistic’ cuts, in particular to isolate the jets from each other and the H and Z decay products, we will impose a large rapidity separation cut in which one jet is produced far forward and one far backward: $|\eta_1|, |\eta_2| > \eta_{\min}$, $\eta_1 \cdot \eta_2 < 0$. For the Higgs production process, which has no infrared or collinear singularities, the imposition of $p_{T\min}$ and $\eta_1 \cdot \eta_2 < 0$ acceptance cuts simply reduces the cross section slightly (by approximately 25% for a broad range of $p_{T\min}$ values), see Fig. 4.6.

Figure 4.6 shows that there is a strong ordering of the cross sections $\sigma(Z, QCD) \gg \sigma(Z, EW) \gg \sigma(H)$, with $\sigma(Z, QCD)$ exhibiting the strongest dependence on $p_{T\min}$. The W cross section has a stronger infra-red singularity as $p_{T\min} \rightarrow 0$ than the corresponding Z cross section, due to the soft photon singularity present in the extra diagram with respect to the Z production process involving the triple gauge boson vertex (Fig. 4.3(a)). This is shown more clearly in W/Z cross section ratio plot, Fig. 4.7. The Higgs cross section is only weakly dependent on the mass m_H , decreasing by a factor of two as m_H increases from 100 GeV to 200 GeV, see Fig. 4.8.

Note that all the cross sections are evaluated in the zero Z/W width approximation and at leading order in perturbation theory. In particular, in the QCD $Z + 2$ jet calculation the scale of the strong coupling α_S is not determined, and there is a non-negligible scale dependence uncertainty as a result. We use $\alpha_S \equiv \alpha_S(m_Z^2)$ throughout. One could argue for a smaller scale, characteristic of the transverse momenta of the forward jets, e.g. $\alpha_S \equiv \alpha_S(p_{T\min}^2)$. We will discuss the impact of such a choice on our predicted event rates in Section 4.5.

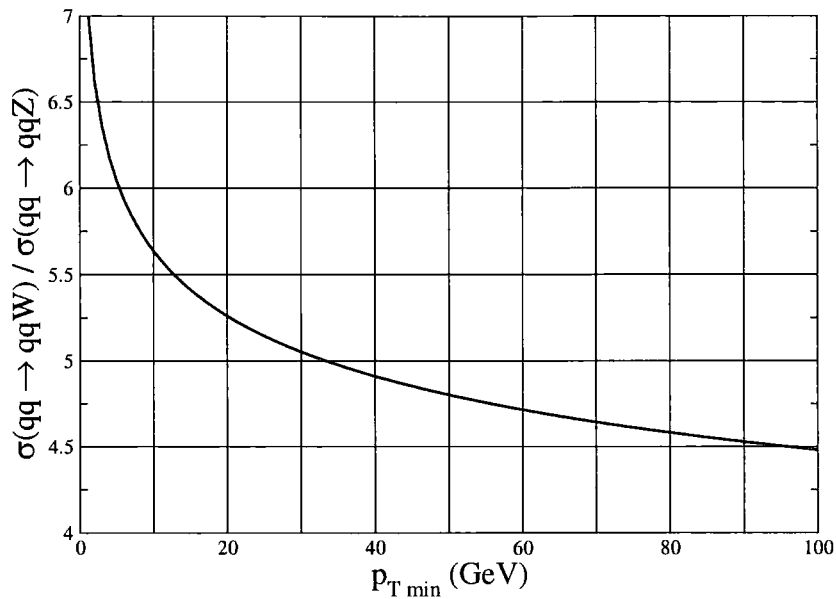


Figure 4.7: Ratio between total cross sections of the W and Z electroweak production processes as a function of $p_{T \min}$ of the forward jets.

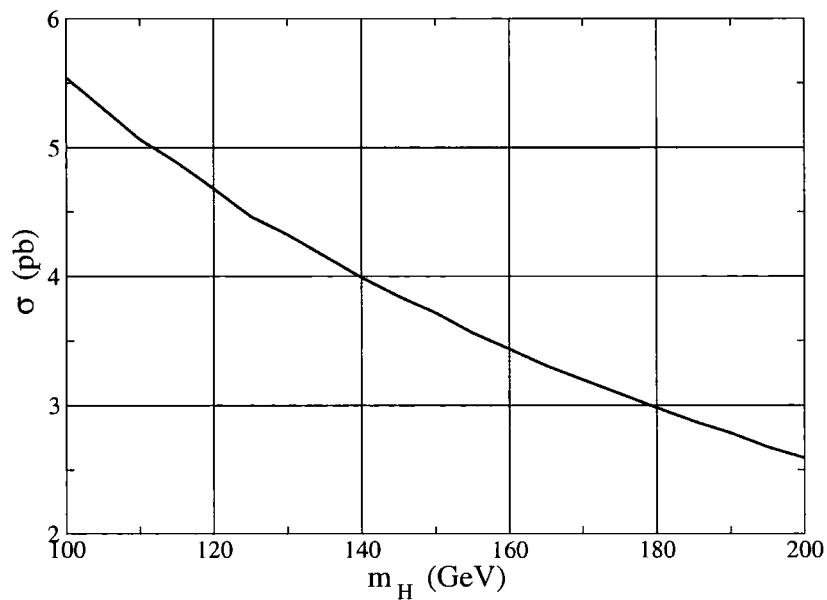


Figure 4.8: LHC $qq \rightarrow qqH$ cross section as a function of the Higgs mass.

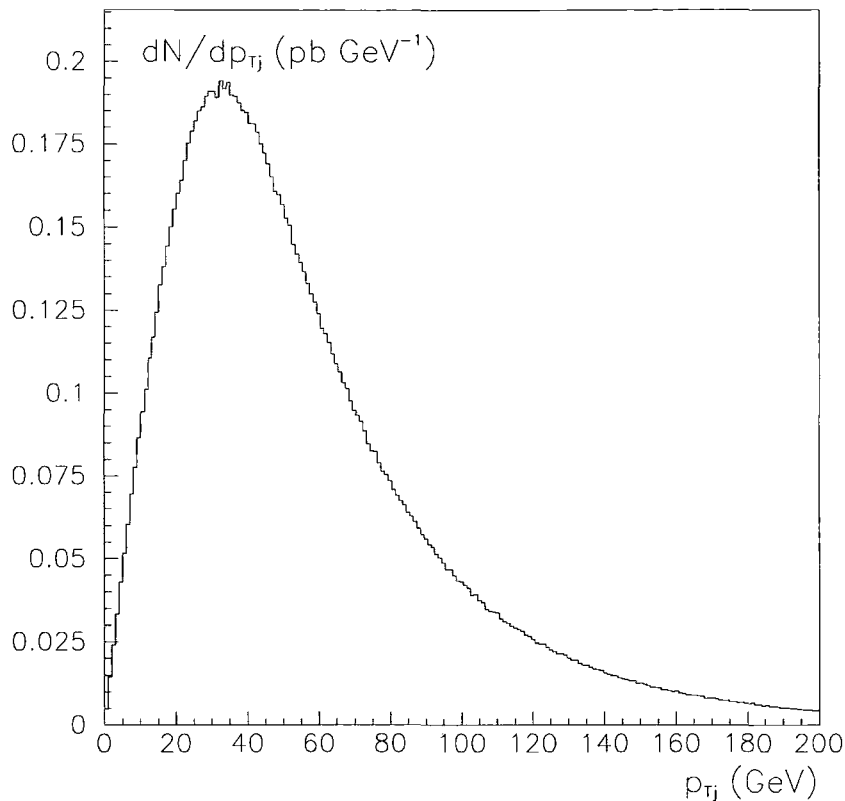


Figure 4.9: Jet transverse momentum distribution for $qq \rightarrow qqH$.

4.3.2 Distributions

Our objective here is to explore in detail the parton level kinematic distribution and thus find a set of selection cuts that minimises the background while not affecting drastically the Higgs, Z and W rapidity gap signal.

Higgs Production

We begin by calculating the transverse momentum distributions of the forward tagging jets, Figs. 4.9. Evidently the jets are predominantly produced with transverse momenta of order $m_W/2 \sim 40$ GeV. This agrees nicely with the parton sampling distribution shown in Fig. 4.10. It peaks at a value of $-\ln(x) \simeq 2$, i.e. $x \simeq 0.01$. Then $m_{\text{central}} = \sqrt{\hat{s}} = \sqrt{x_1 x_2 s} \sim \mathcal{O}(100)$ GeV.

Turning to the jet rapidity distribution of Fig. 4.11, we see that, as sus-

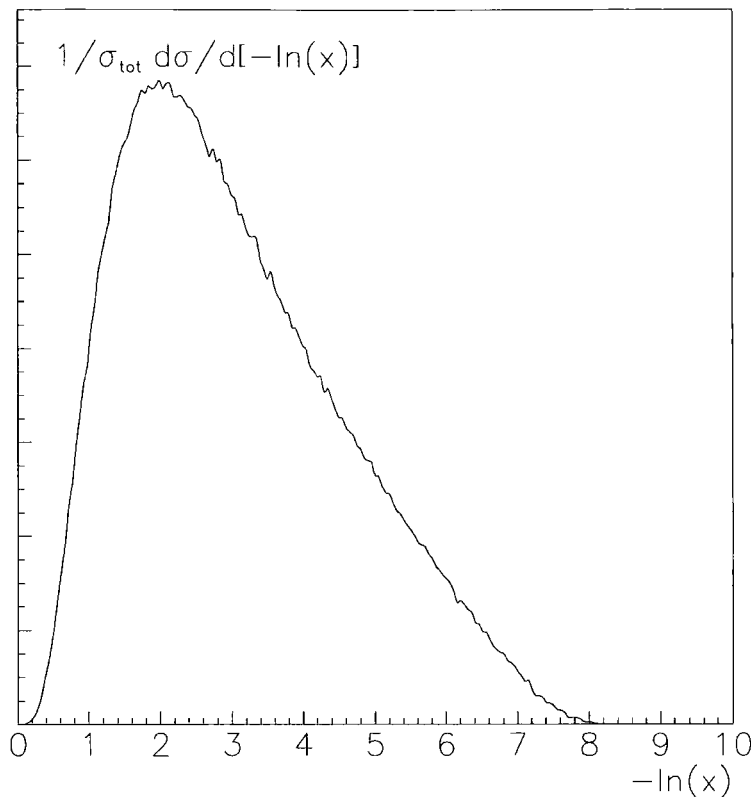


Figure 4.10: Parton sampling distribution

pected, it shows a strong peaking structure and has maxima at $|\eta_{\text{jet}}| = 3$. The fact that events are predisposed to a large separation in rapidity of the jets is shown in Fig. 4.12. For $p_{T\text{jet}} > 40$ GeV we see that the average jet separation $\Delta\eta_{\text{jet}} = 4.4$. As we relax the restriction on the jet transverse momentum the peak moves to larger values of separation. This is because we are allowing more forward jets to contribute. Notice the small excess around $\Delta\eta_{\text{jet}} \sim 1/2$. This is caused by the contributing process $q\bar{q} \rightarrow Hq\bar{q}$ in which $m_{jj} \sim m_Z$, i.e. the Higgs is produced in association with a Z (or W) boson which subsequently decays into a $q\bar{q}$ pair, see Fig. 4.13. This is more clearly seen in the dijet mass distribution, Fig. 4.14.

Requiring the jets to be well-separated in rapidity forces m_{jj} to be large and this resonant contribution is strongly suppressed. For example, Fig. 4.14

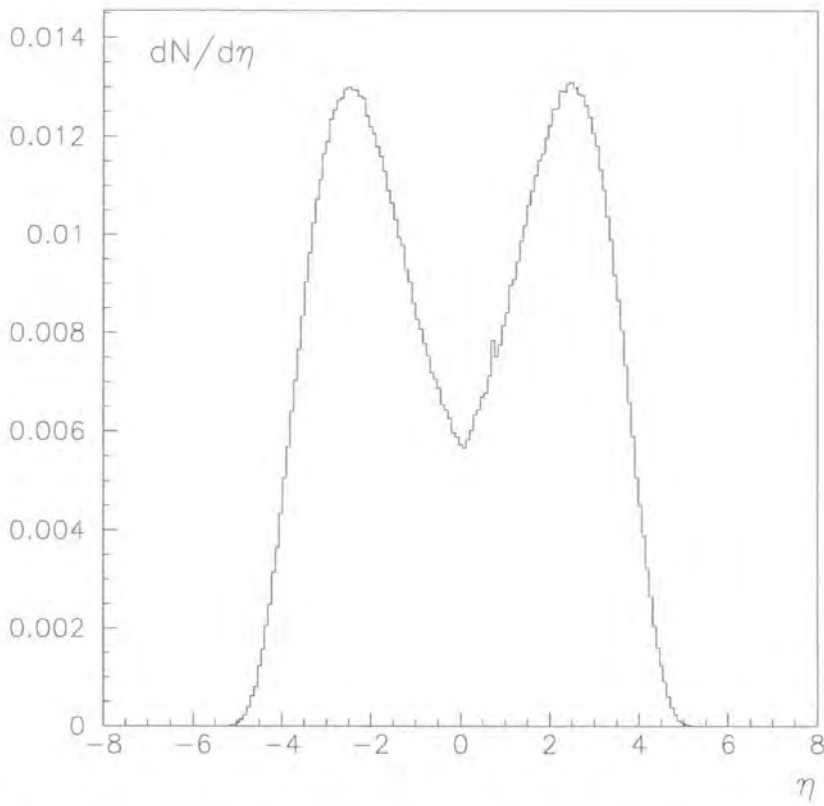


Figure 4.11: Jet rapidity distribution for $qq \rightarrow qqH$ with $p_{T\min} = 40$ GeV and $\eta_1 \cdot \eta_2 < 0$.

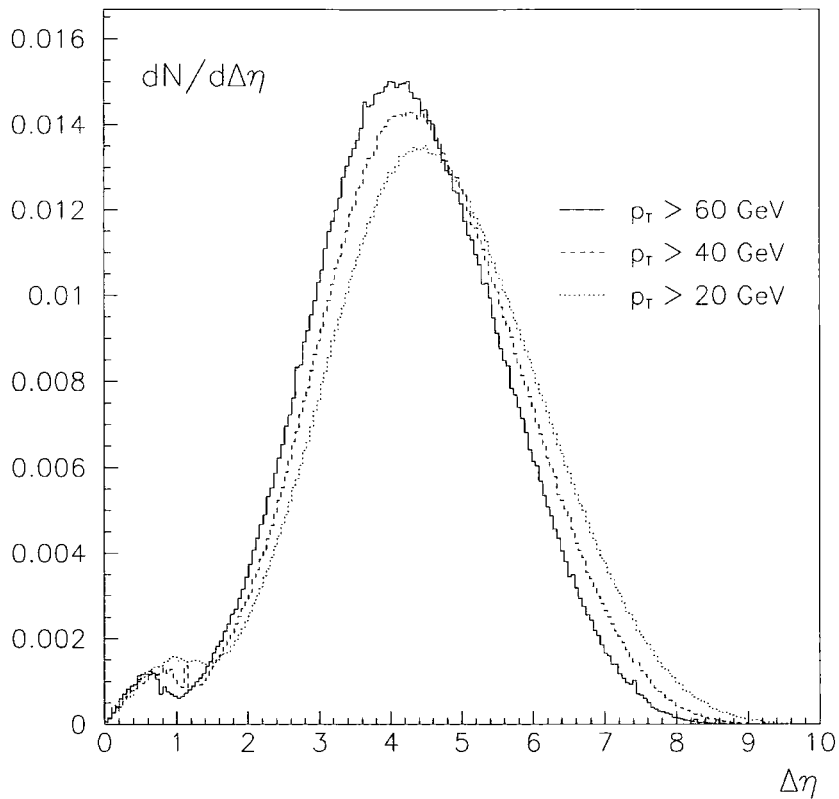


Figure 4.12: Dijet rapidity difference for $qq \rightarrow qqH$.

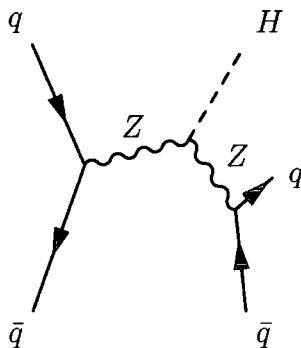


Figure 4.13: Contribution to the $\mathcal{O}(\alpha_W^3)$ electroweak $q\bar{q} \rightarrow q\bar{q}H$ that resonates when $m_{jj} \sim m_Z$.

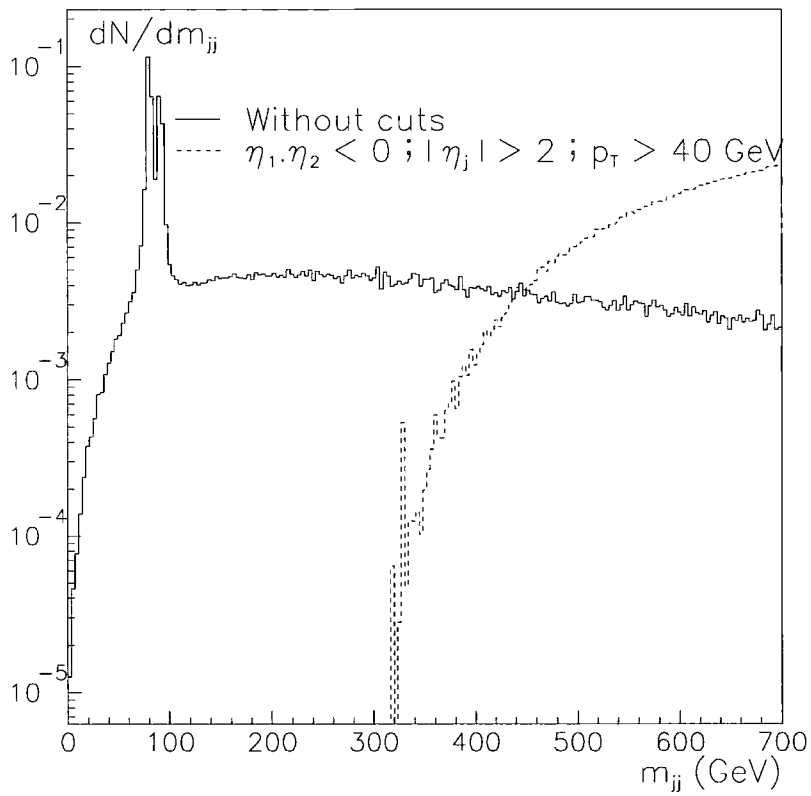


Figure 4.14: Dijet invariant mass for $qq \rightarrow qqH$ showing a double resonance around m_Z and m_W .

also shows the dijet mass distribution for $|\eta_{1,2}| > \eta_{\min} = 2$. Note that in this plot both rates are normalised to their respective total cross sections.

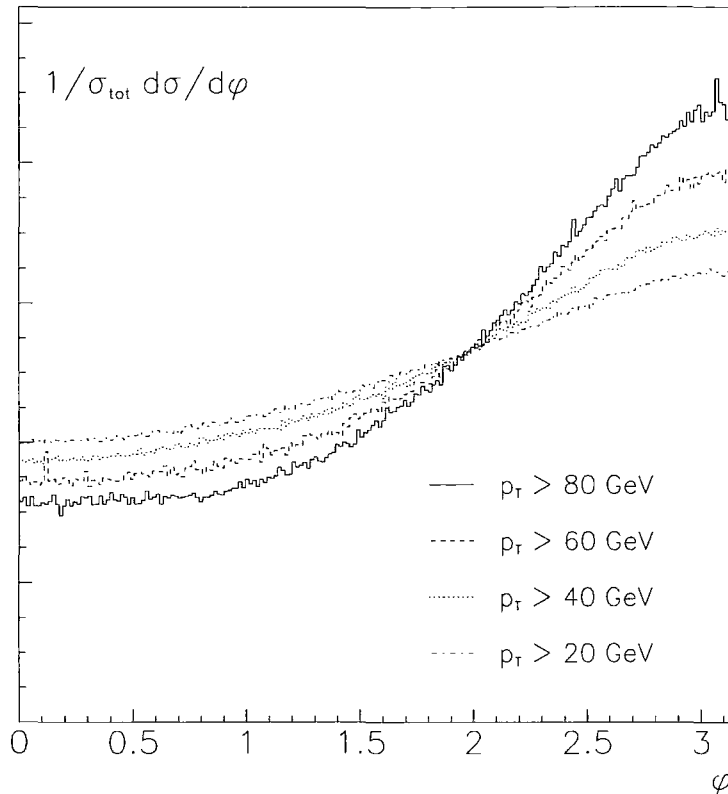


Figure 4.15: Jet azimuthal distribution for $qq \rightarrow qqH$.

The azimuthal distribution of the forward jets is shown in Fig. 4.15. We see that there is a slight preference for the jets to be back-to-back that increases as we raise $p_{T\min}$ from 20 GeV to 80 GeV. The central system is able to compensate for the jets not being back-to-back, but this ability decreases as we require the jets to have a higher transverse momentum.

Electroweak Z and W Production

The jet rapidity distribution for electroweak qqZ production is shown in Fig. 4.16. Comparing with Fig. 4.11 for qqH , we see that the jets produced with a Z are more uniform in rapidity. The ‘ WW -fusion’ diagrams of

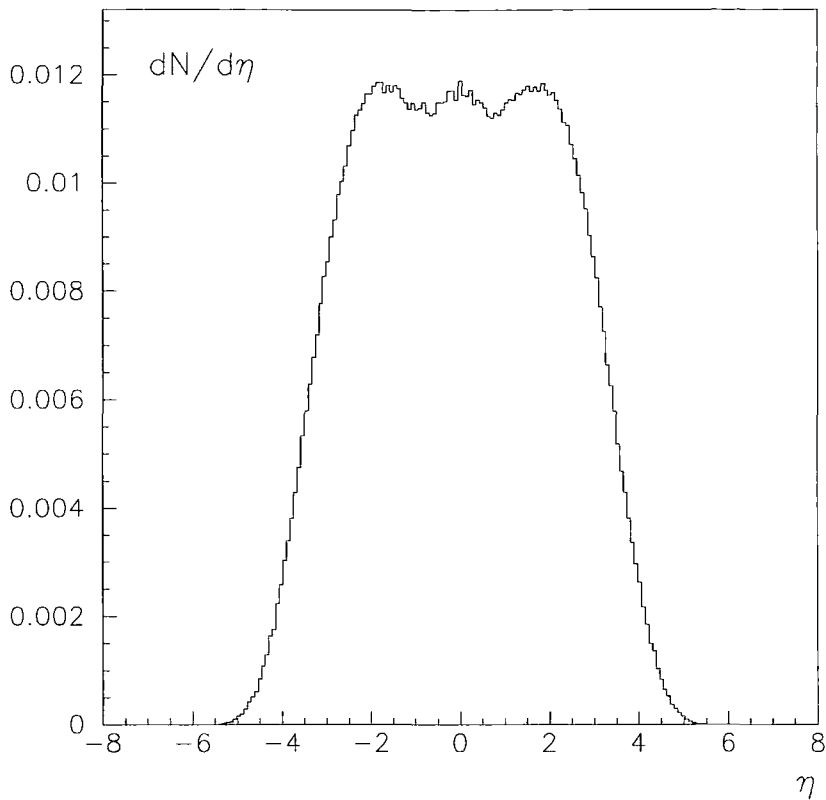


Figure 4.16: Jet rapidity distribution for electroweak Z production.

Fig. 4.2(a) still produce jets with a large separation, but the central region is now filled in by contributions from the other non-fusion ‘ Z -bremßstrahlung’ processes, Figs. 4.2(b,c). Electroweak W production has very similar characteristics to electroweak Z production.

The azimuthal distribution of the jets is shown in Fig. 4.17. We see that it is more back-to-back than in Higgs production. This is again the effect of the Z -bremßstrahlung diagrams where the Z system is less able to compensate for any azimuthal imbalance within the dijet system. Obviously, as we increase the minimum jet transverse momentum, this becomes more pronounced.

Fig. 4.18 shows the azimuthal angle separating the Higgs or electroweak Z from the nearest forward jet. The Z ‘follows’ the jet more than the Higgs. The Z -bremßstrahlung diagrams have this effect as the configuration min-

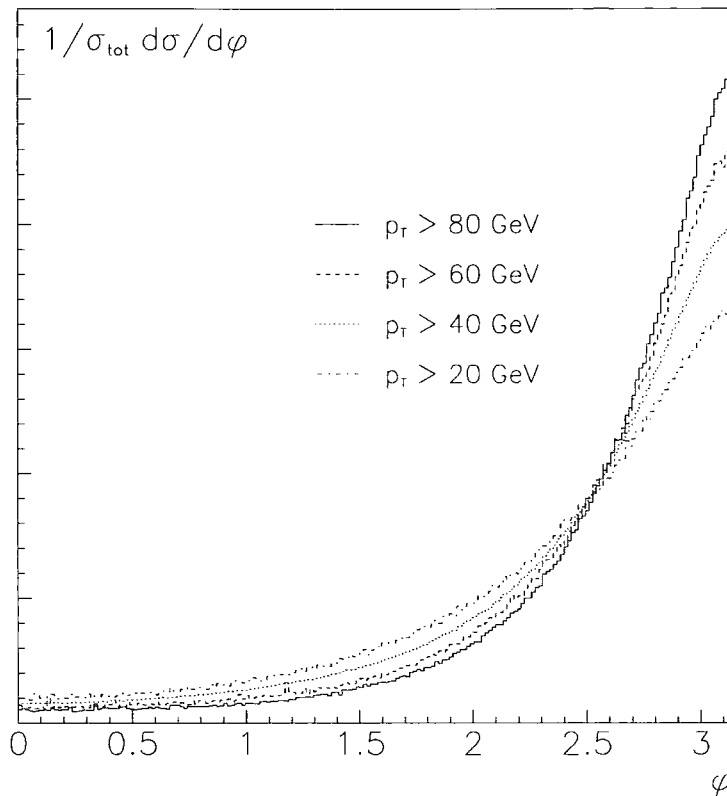


Figure 4.17: Jet azimuthal distribution for electroweak $qq \rightarrow qqZ$.

imises the quark propagator between the t -channel vector boson and the qqZ vertex.

Fig. 4.19 compares the rapidity distribution of the Higgs and electroweak Z when the jet $p_{T\min} = 40$ GeV. It confirms our assertion at the start of this section that the Z will have a broader rapidity profile.

In Fig. 4.20 the jet $p_{T\min}$ is lowered and rapidities of electroweak W and Z are compared. The W is seen to be more central, this is due to the extra t -channel γ diagram of Fig. 4.3a. The closer we take $p_{T\min}$ to the stronger IR pole for W production (see Fig. 4.7), the bigger this effect.

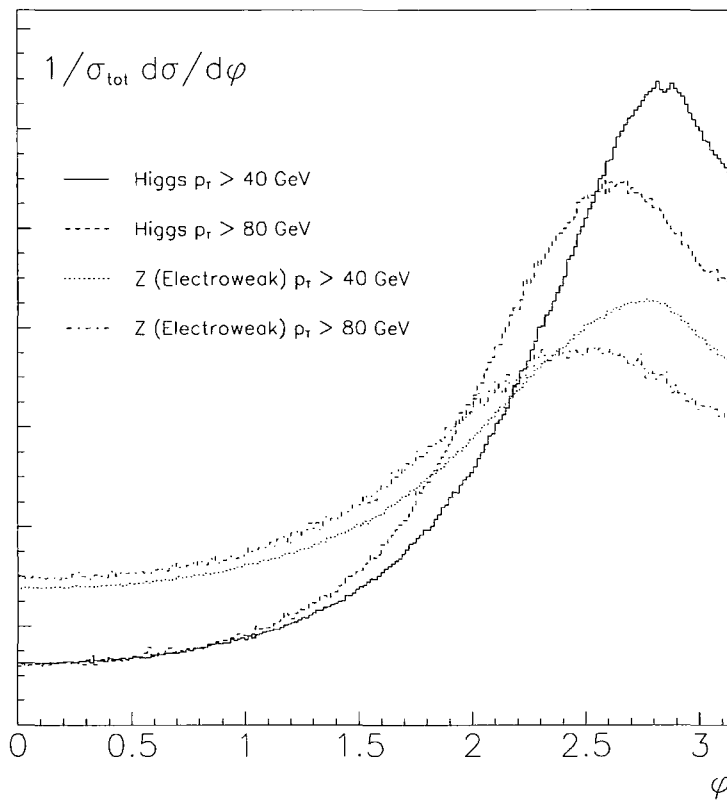


Figure 4.18: Azimuthal angle distribution of Higgs or electroweak Z from the forward jets.

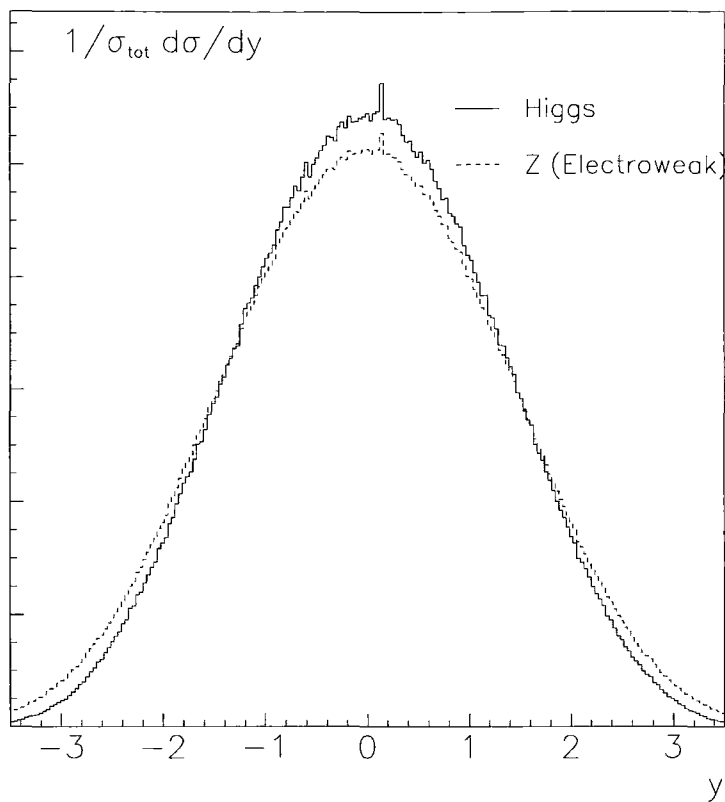


Figure 4.19: Higgs and electroweak Z rapidity distribution for $p_{T\min} = 40$ GeV.

QCD Z Production

For the QCD background to electroweak Z production, the jets are produced much more centrally, see Fig. 4.21. Requiring a jet in each forward/backward hemisphere leads to a typical rapidity separation of about 3, as shown in Fig. 4.22, which is significantly less than for either H or electroweak Z production. There is no natural rapidity gap, as for the t -channel colour-singlet exchange processes. The jet azimuthal distribution is shown in Fig. 4.23. It is more peaked than the Higgs signal for the same reason as that of the electroweak case. However it is less peaked than electroweak Z production, this is due to the fact that, since the gluon is massless, $t \rightarrow 0$ and $p_1 \cdot p_3 \rightarrow m_Z^2$, a non-zero value.

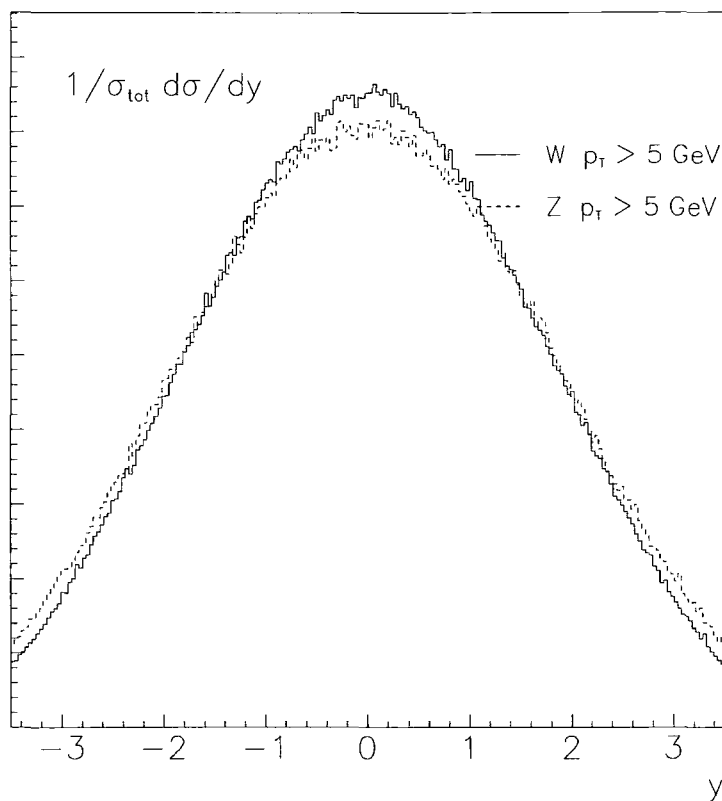


Figure 4.20: Electroweak Z and W rapidities at low jet $p_{T\min}$

4.3.3 Selection cuts

We can now proceed to define a set of selection cuts that leads to a sample of H , Z and W events with the potential to exhibit rapidity gaps. Since our primary goal is to calibrate the gap survival for Higgs production, we will concentrate first on the $b\bar{b}$ decays of H and Z , the latter produced either via electroweak or QCD processes.

When considering the $b\bar{b}$ decay modes of both the Higgs and Z bosons, we must include also the important irreducible background from QCD $\mathcal{O}(\alpha_S^4)$ $b\bar{b} + 2$ jet production, see Fig. 4.5. Such processes give a continuous distribution of $b\bar{b}$ masses, and in what follows we impose a cut of $|m_{b\bar{b}} - m_Z| < 10$ GeV to select those background events that mimic $Z \rightarrow b\bar{b}$ decay.

The configuration we have in mind has one jet registered in a forward

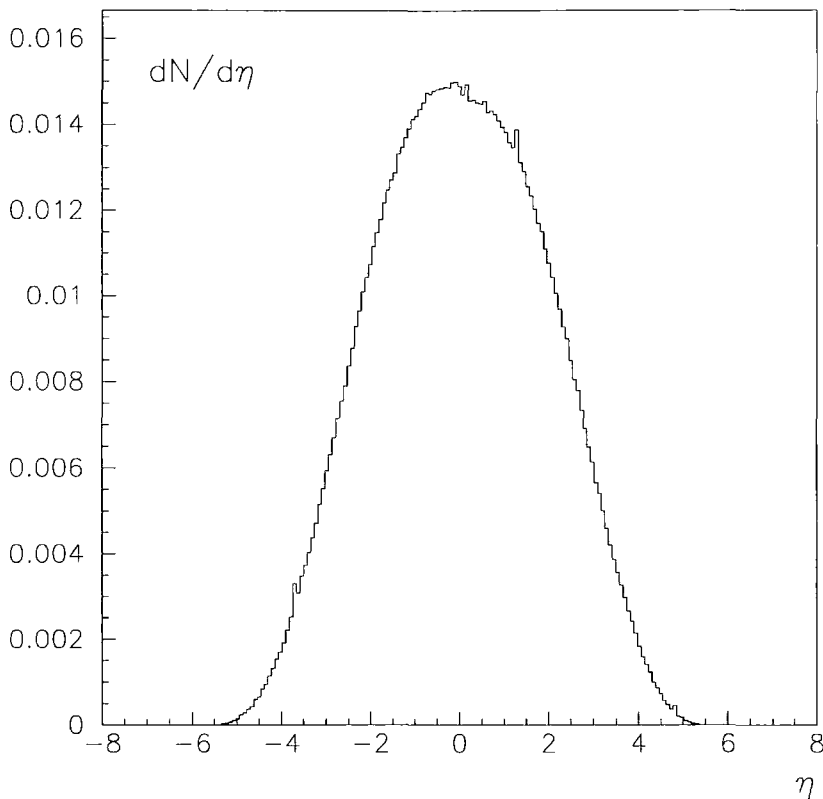


Figure 4.21: Jet rapidity distribution for QCD $Z + 2$ jet production.

detector with $\eta > \eta_{\min}$, another produced backwards with $\eta < -\eta_{\min}$, and the two b jets from H and Z decay produced centrally. From the results of the previous section, such a selection will in principle preserve the bulk of the Higgs signal while suppressing the (non-gap) QCD Z and $b\bar{b} + 2$ jet production.

For both ATLAS [51] and CMS [81], the forward hadron calorimeters cover approximately $3 < |\eta| < 5$, and so we will require our forward dijets to be produced in this region of rapidity, with $p_T > p_{T\min} = 40$ GeV. In order to separate the H , Z decay jets from the forward jets, we require $|\eta_b| < 1.5$, and $p_{Tb} > 10$ GeV⁵.

⁵The typical transverse momentum of the jets in both the signal and Z -induced background processes is $\sim m_Z/2$, and this cut does not have any significant effect on the event rates, see for example Table 4.1.

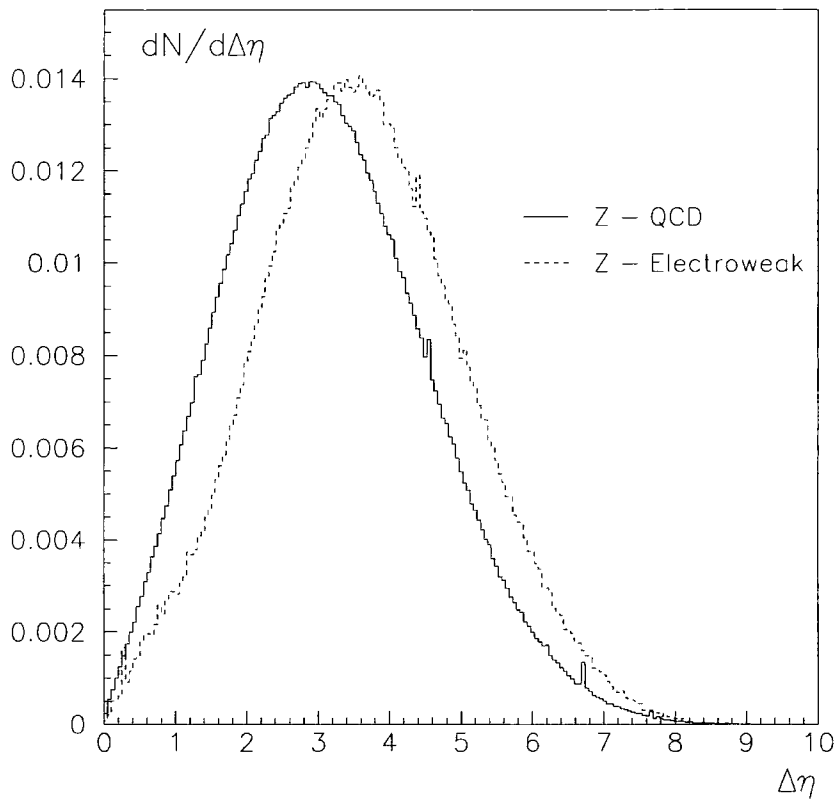


Figure 4.22: Comparison of dijet rapidity differences for electroweak and QCD Z production.



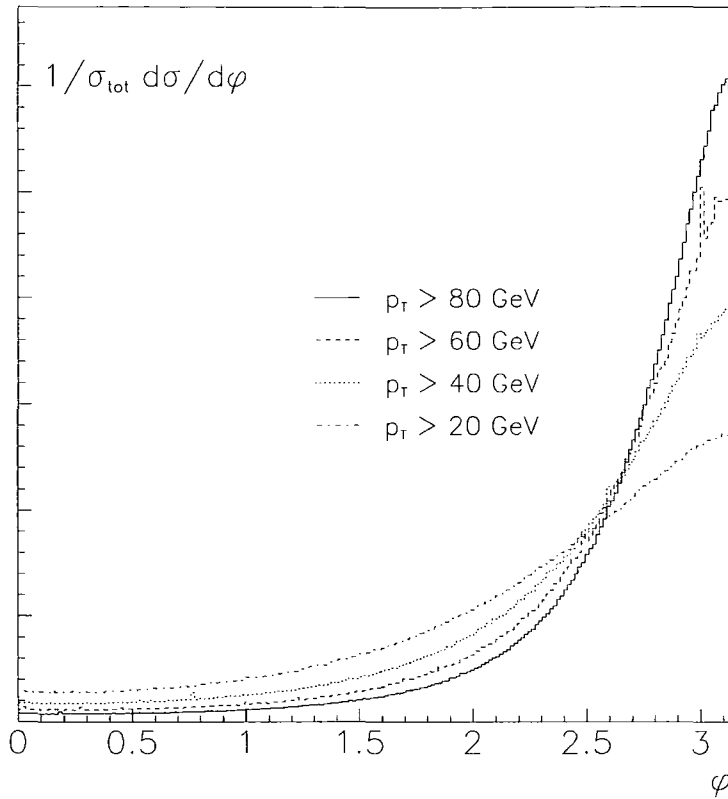


Figure 4.23: Jet azimuthal distribution for $qq \rightarrow qqZ$ (QCD).

Although these cuts are designed to reflect the ‘natural’ characteristics of qqH production, they do result in a non-negligible loss of signal rate, even before b -tagging efficiencies etc. are taken into account. This is illustrated in Table 4.1, which quantifies the effect on the cross section of applying the cuts sequentially. One can see that imposing forward jet cuts has the largest impact on the cross section, and indeed this is the case for all the processes considered. It should be noted that we do not include experimental sources of signal loss such as the b -tagging efficiencies. These would give a slight reduction as the typical efficiency is 80% [82].

In Fig. 4.24 we show the transverse momentum distribution for the QCD processes $qq' \rightarrow qq'b\bar{b}$ and $gg \rightarrow ggb\bar{b}$ together with that for Higgs production with subsequent decay to $b\bar{b}$. We see that the backgrounds are more strongly

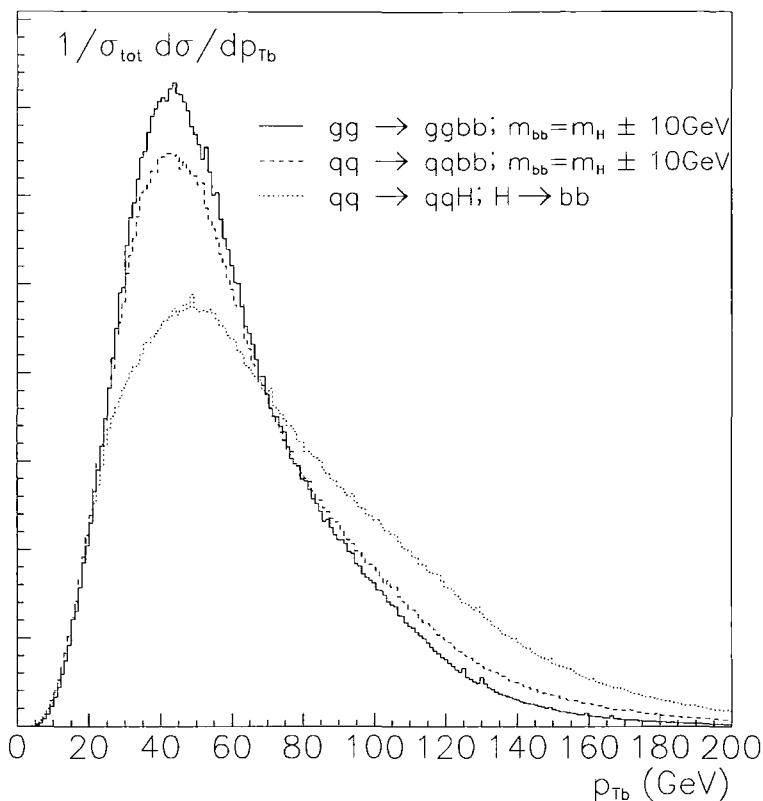


Figure 4.24: Transverse momentum of b jets.

Cut Imposed	$qq \rightarrow qqH$ Cross Section for $p_{T\text{jet}} > 40$ GeV (pb)	% of Initial Cross Section
	4.86	100
$\text{Br}(H \rightarrow bb)$	3.49	71.9
$\eta_1 \cdot \eta_2 < 0$	2.47	50.8
$\Delta\eta_j > 6$	0.495	10.2
$ \eta_j > 3$	0.0990	2.04
$ \eta_b < 1.5$	0.0465	0.957
$p_{Tb} > 10$ GeV	0.0463	0.953

Table 4.1: Loss of $qq \rightarrow qqH$ LHC cross section with $m_H = 115$ GeV when applying selection cuts.

peaked at $m_H/2$. This is because we are cutting off an IR singularity at $p_{Tb} = 0$ with the imposed rapidity cuts.

Figures 4.25 and 4.26 show the cross sections at $\sqrt{s} = 14$ TeV as a function of $p_{T\text{min}}$ for all processes. The Higgs production cross section is reduced

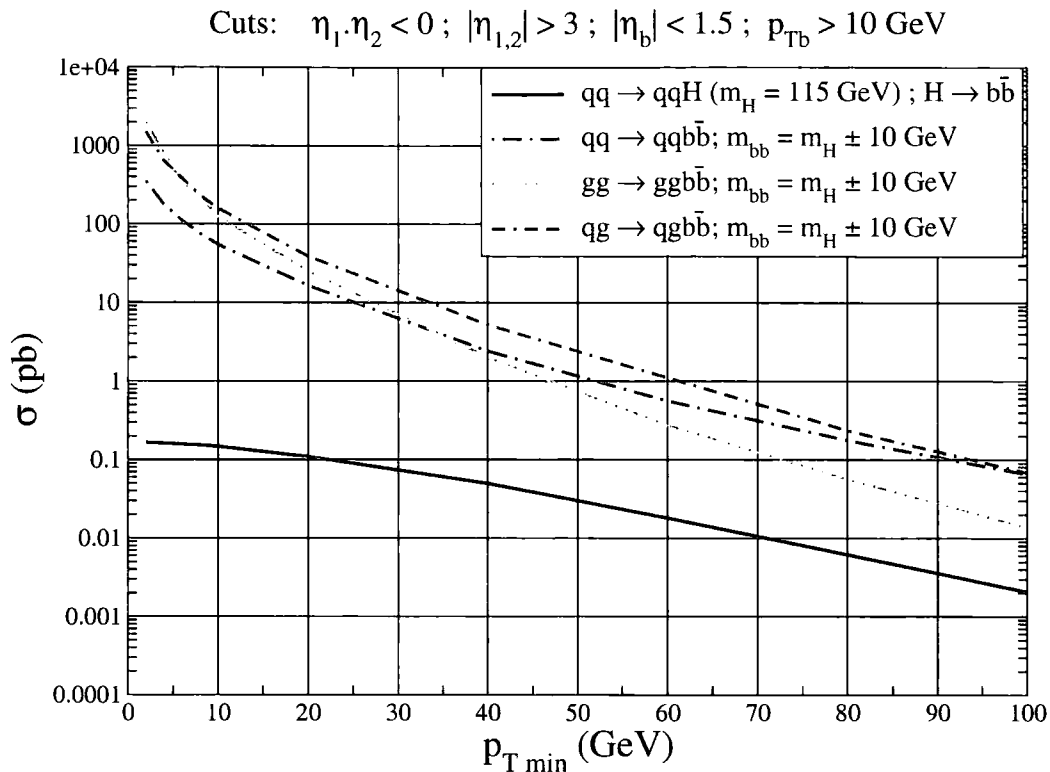


Figure 4.25: Parton level LHC cross sections for Higgs production processes after application of cuts.

by a factor of ~ 100 and the electroweak Z production by ~ 1000 in comparison with Fig. 4.6⁶. The cuts reduce the Z production QCD background by a factor of ~ 10000 . As already mentioned, in evaluating the pure QCD $b\bar{b}$ production cross sections we further impose the restriction that the dijet invariant mass be within 10 GeV of m_Z .

⁶This is because of the difference in rapidity distributions in the H (Figs. 4.11,4.12) and Z (Figs. 4.16,4.22) cases which is caused by the process shown in Figs. 4.2(b),(c) and 4.4(d) where the quark jets are closer to each other.

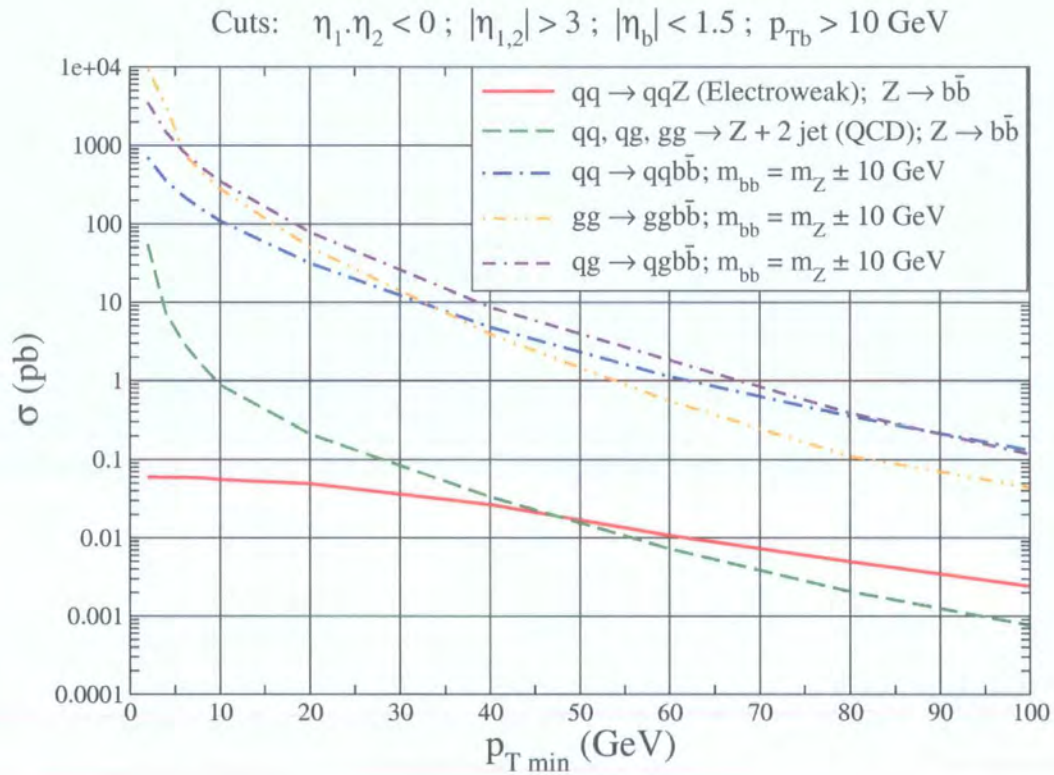


Figure 4.26: Parton level LHC cross Sections for Z production processes after application of cuts.

4.3.4 Properties of the QCD $b\bar{b} + 2$ jet Backgrounds

The continuum $b\bar{b} + 2$ jet backgrounds are interesting in their own right. In the phase space regime into which we restrict them, they display a property of simpler QCD dijet production. Namely, they obey the *single effective subprocess approximation* [83].

In dijet production, some of the leading order matrix elements for the massless quark and gluon subprocesses are

$$\begin{aligned}
\overline{\sum} |\mathcal{M}(gg \rightarrow gg)|^2/g^4 &= \frac{9}{2} \left(3 - \frac{\hat{t}\hat{u}}{\hat{s}^2} - \frac{\hat{s}\hat{u}}{\hat{t}^2} - \frac{\hat{s}\hat{t}}{\hat{u}^2} \right) \\
\overline{\sum} |\mathcal{M}(qq \rightarrow qq)|^2/g^4 &= -\frac{4}{9} \frac{\hat{s}^2 + \hat{u}^2}{\hat{s}\hat{u}} + \frac{\hat{s}^2 + \hat{u}^2}{\hat{t}^2} \\
\overline{\sum} |\mathcal{M}(qq' \rightarrow qq')|^2/g^4 &= \frac{4}{9} \frac{\hat{s}^2 + \hat{u}^2}{\hat{t}^2}.
\end{aligned} \tag{4.30}$$

where the Mandelstam variables $\hat{s} \equiv (p_1 + p_2)^2$, $\hat{t} \equiv (p_1 - p_3)^2$, $\hat{u} \equiv (p_2 - p_3)^2$ and the hatted variables emphasise that we are considering parton level scattering. In terms of the dijet rapidity difference $\Delta\eta$ the invariants are⁷

$$\begin{aligned}
\hat{s} &= 4E_T^2 \cosh^2(\Delta\eta/2) \\
-\hat{t} &= 2E_T^2 \cosh(\Delta\eta/2) \exp(-\Delta\eta/2) \\
-\hat{u} &= 2E_T^2 \cosh(\Delta\eta/2) \exp(+\Delta\eta/2)
\end{aligned} \tag{4.31}$$

In the limit where we require a large rapidity gap they become

$$\begin{aligned}
\hat{s} &\simeq -\hat{u} \simeq E_T^2 \exp(\Delta\eta) \\
-\hat{t} &\simeq E_T^2
\end{aligned} \tag{4.32}$$

⁷Note that the rapidity of the parton centre of mass is equal to the mean rapidity as it is additive.

and the dijet rapidity difference

$$\Delta\eta \simeq \ln(-\hat{s}/\hat{t}). \quad (4.33)$$

Applying this to our example full matrix elements,

$$\begin{aligned} \overline{\sum} |\mathcal{M}(gg \rightarrow gg)|^2/g^4 &\xrightarrow{\Delta\eta \rightarrow \infty} \frac{9}{2} \frac{\hat{s}^2}{\hat{t}^2} \\ \overline{\sum} |\mathcal{M}(qg \rightarrow qg)|^2/g^4 &\xrightarrow{\Delta\eta \rightarrow \infty} 2 \frac{\hat{s}^2}{\hat{t}^2} \\ \overline{\sum} |\mathcal{M}(qq' \rightarrow qq')|^2/g^4 &\xrightarrow{\Delta\eta \rightarrow \infty} \frac{8}{9} \frac{\hat{s}^2}{\hat{t}^2}. \end{aligned} \quad (4.34)$$

Interestingly, processes where there can be no t -channel gluon do not contribute at leading order in \hat{s}/\hat{t} . The only difference between the t -channel mediated subprocesses in this limit is the difference in quark-gluon and gluon-gluon couplings, thus C_F/C_A appears as the constant of proportionality i.e. $|\mathcal{M}_{qg}|^2 = (4/9)|\mathcal{M}_{gg}|^2$ and $|\mathcal{M}_{qq'}|^2 = (4/9)^2|\mathcal{M}_{gg}|^2$. We can view this as there being only one fundamental matrix element and the cross section can be calculated by convoluting this with a single effective structure function

$$S(x, \mu^2) = g(x, \mu^2) + \frac{4}{9} [q(x, \mu^2) + \bar{q}(x, \mu^2)]. \quad (4.35)$$

This is entirely analogous with the situation we are studying where in addition to forward dijets there is also a central $b\bar{b}$ system. Although we can no longer analytically prove the relations, they should still be valid as we are forcing the diagrams of the examples in Fig. 4.5 to dominate over any others, i.e. we are selecting \hat{s}/\hat{t} large. The hard subprocess cross sections are shown in Fig. 4.27. Indeed they obey the single effective subprocess approximation as they are, to a very close approximation, proportional to each other.

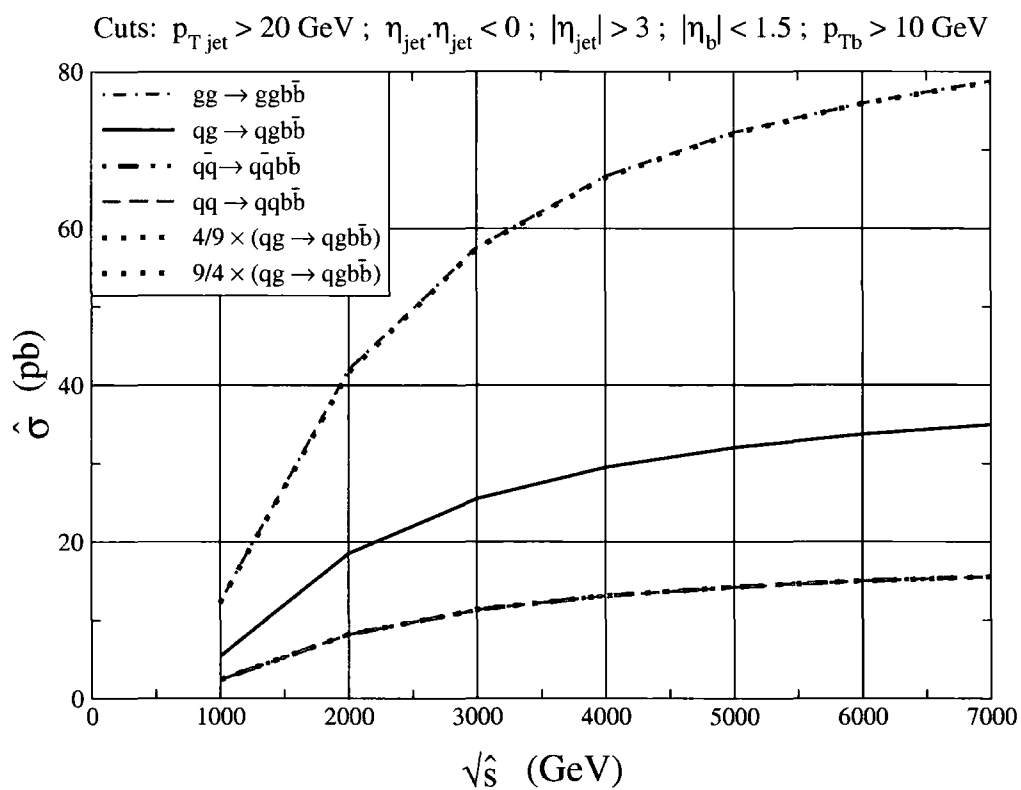


Figure 4.27: Hard subprocess cross sections for QCD continuum $b\bar{b} + 2$ jet backgrounds.

In Figs. 4.25 and 4.26 we see that the gluon-gluon induced cross section is dominant when the cut on $p_{T\min}$ is small but drops below the quark induced subprocesses as the cut is raised. This is because we sample higher x as we raise our cut, we are seeing the fall of the high x gluon distribution.

4.4 Gap Survival Probabilities

Our parton level cross sections for signals and backgrounds will be reduced (hopefully more so in the latter case) by probabilities for the gap to *not* be populated by secondaries arising from two separate processes. Firstly, perturbative gluon radiation from the hard subprocesses; we will denote this probability T^2 . Secondly, soft rescattering of spectator partons in the proton; this is a non-perturbative mechanism which we will denote \hat{S}^2 .

4.4.1 Parton Level Gap Survival

As seen in Figs. 4.25, 4.26, the QCD-induced $b\bar{b}$ background is still large. It exceeds by two orders of magnitude the Z/H cross sections and it is therefore necessary to impose a stringent discriminatory condition. Therefore we take our definition of rapidity gap to mean that it is *completely clean*, i.e. without any soft hadrons. All the QCD processes we consider are characterised by gluon (or quark) t -channel exchange, which unavoidably produces a colour flow along the gap. During hadronisation this colour flow, in turn, creates plenty of soft secondaries which fill the gap. On the other hand, there is no such effect for the electroweak graphs (Figs. 4.1, 4.2a, 4.2b) since the vector boson exchange is colourless. This means that if we wish to observe clean hadron-level gaps we can immediately discard the diagrams of Fig. 4.5. The only way to create a gap in a QCD induced event is to screen the colour

flow (across the gap) by an additional gluon (or quark) exchange; that is, to consider graphs of the type shown in Fig. 4.28.

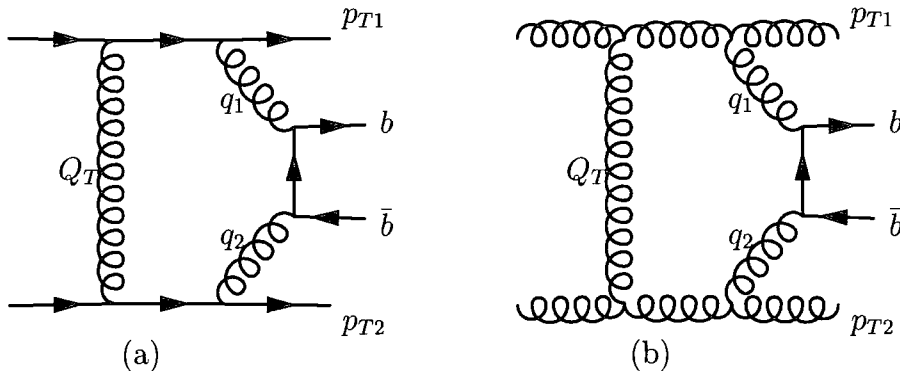


Figure 4.28: Screening of QCD dijet + $b\bar{b}$ production via gluon exchange.

Gluon Exchange

Note that in leading order we can screen the colour flow in both gaps (above and below the $b\bar{b}$ -pair) with only one additional t -channel gluon, with momentum Q_T say. The price we pay for this screening is a factor of α_S supplemented by the dQ_T^2 loop integration in each amplitude; that is $(\int \alpha_S \dots d^2Q_T)^2$ in the cross section. At first sight, the major contribution comes from the small Q_T region where the QCD coupling α_S is larger. Moreover, the integral takes the form

$$\int \alpha_s \frac{dQ_T^2}{Q_T^2} \quad (4.36)$$

and has infra-red logarithmic divergence at $Q_T \ll p_{T1,2}$. However, this divergence is cut off by the effects of higher order double logarithmic QCD radiation, see for example [84–86]. The point is that a small Q_T gluon screens the hard gluon at rather large distances $r \sim 1/Q_T$ only. Thus a ‘hard’ gluon $q_{i=1,2}$ may emit a new ‘semihard’ gluon jet, with transverse energy E_T ranging from Q_T up to $q_{iT} = |\vec{p}_{Ti} - \vec{Q}_T|$ in the whole rapidity gap interval $\Delta\eta_i$. The

leading (double) logarithms come from the $Q_T \ll E_T \ll p_{T,jet}$ domain where the expected mean number of these secondary gluons is

$$\bar{n}_i \simeq \frac{N_c \alpha_S}{\pi} \Delta\eta_i \ln \frac{p_{Ti}^2}{Q_T^2}. \quad (4.37)$$

where one of the logs is expressed as the $\Delta\eta$ term. This expression is the analogue of the n soft photon emission probability in QED, a derivation of which is sketched in Appendix A. At the amplitude level, the corresponding suppression factor describing the probability for *not* having such an emission (which otherwise destroys the gap) has the Sudakov-like form

$$\exp(-\bar{n}_i/2) = \left(\frac{Q_T}{p_{Ti}} \right)^{\frac{N_c \alpha_S}{2\pi} \Delta\eta}. \quad (4.38)$$

Including this factor in the loop integral, we eliminate the infrared divergence and obtain the probability, P_a ($a = qq, qg, gg$ depending on the initial state), to screen out the octet (gluon-like) colour flow in qq (gg or qg) interactions,

$$\begin{aligned} P_a &= C_a \left(\int_{Q_0}^{p_{T,\min}} \alpha_S(Q_T^2) \frac{dQ_T^2}{Q_T^2} \exp \left\{ -\frac{N_c \Delta\eta}{2\pi} \int_{Q_T}^{p_{T,\min}} \alpha_S(Q'^2) \frac{dQ'^2}{Q'^2} \right\} \right)^2 \\ &= C_a \left(\frac{2\pi}{N_c \Delta\eta} \right)^2 \end{aligned} \quad (4.39)$$

Here $\Delta\eta = \Delta\eta_1 + \Delta\eta_2$ is the overall length of the gaps and, within leading logarithm accuracy, we have put the upper limits in the Q_T (Q') integration equal to the minimum p_T of the jets. In order to arrive at the right-hand side of Eq. 4.39 it is convenient to recast the integral in Eq. 4.39 as

$$\left(\frac{2\pi}{N_c \Delta\eta} \right) d\mathcal{J} \exp(-\mathcal{J}(p_{T,\min}, Q_T)), \quad (4.40)$$

with

$$\mathcal{J} = \frac{N_c \Delta\eta}{2\pi} \int_{Q_T}^{p_{T\min}} \alpha_s(Q'^2) \frac{dQ'^2}{Q'^2}. \quad (4.41)$$

Performing the integration, we neglect the term $\exp(-\mathcal{J}(p_{T\min}, Q_0))$ corresponding to the lower limit of integration. This can always be done safely if we can continue the perturbative calculation down to the (rather low) scale where the quantity $\alpha_s(Q_0^2) \cdot \Delta\eta$ becomes large. Instead of the conventional double logarithm expressions (Eqs. 4.37,4.38) with a fixed coupling α_s , in Eq. 4.39 we have used the running coupling in order to demonstrate that the result does not depend on whether one accounts for the running α_s or not. The colour factors C_a are

$$\begin{aligned} C_{qq} &= \frac{C_F^2}{(N_c^2 - 1)} = \frac{C_F}{2N_c} = \frac{2}{9} \\ C_{gg} &= \frac{N_c^2}{N_c^2 - 1} = \frac{9}{8} \\ C_{qg} &= \frac{C_F N_c}{N_c^2 - 1} = \frac{1}{2}. \end{aligned} \quad (4.42)$$

A more precise way to calculate the contributions of Fig. 4.28 including QCD radiative effects is to replace the two gluon t -channel exchange by the skewed BFKL amplitude [87]. For the asymmetric ($Q_T \ll q_{ti}$) configuration, the skewed amplitude contains the double logarithmic factor of Eq. 4.38, while the single logarithmic ($\sim \mathcal{O}(\alpha_s \Delta\eta)$) contribution in this asymmetric kinematical situation is suppressed, giving a less than 10% correction to the amplitude (see [86, 88] for a more detailed discussion). Thus we come back to the result of Eq. 4.39. Strictly speaking, besides the suppression factor Eq. 4.38 hidden in the BFKL amplitude, there should be another Sudakov-like double logarithmic form factor which reflects the absence of QCD radiation in the interval of gluon transverse momentum between $p_{T\text{jet}}$

and half of the boson (or $b\bar{b}$) mass, $M/2$. However, in our case, the transverse momentum of the jets is $p_T > p_{T\min} = 40$ GeV, which is close to half the boson mass $m_{Z,H}/2$. Therefore the form factor becomes close to one and we can neglect it.

Another point we have to take into account is the fact that now the $b\bar{b}$ -pair may be produced in a colour singlet state only, and the ordinary $gg \rightarrow b\bar{b}$ hard subprocess cross section (which includes both colour singlet and octet contributions)

$$\frac{d\hat{\sigma}}{dt}(gg \rightarrow q\bar{q}) = \frac{\pi\alpha_s}{6E_T^2 M^2} \quad (4.43)$$

should be replaced by the pure colour singlet cross section [64]

$$\begin{aligned} \frac{1}{N_c^2 - 1} \frac{d\hat{\sigma}^{\text{incl}}}{dt}(gg^{PP} \rightarrow q\bar{q}) = \\ \frac{\pi\alpha_s^2}{(N_c^2 - 1)E_T^2 M^2} \frac{1}{6} \left[\left(1 - \frac{2E_T^2}{M^2}\right) \left(1 - \frac{2m_q^2}{E_T^2}\right) + \frac{m_q^2}{E_T^2}(1 + \beta^2) \right], \end{aligned} \quad (4.44)$$

where $\beta = \sqrt{1 - \frac{4m_q^2}{M^2}}$ and m_q is the quark mass that we set to zero. The PP superscript merely denotes that the gluons are in the colour singlet state. Note that for the colour singlet production case there is an additional colour factor, $1/(N_c^2 - 1)$, which suppresses the QCD background, as the two colliding gluons are forced to have the same colour. We implement this by simply dividing out the octet contribution to the subprocess.

Thus the parton level gap survival probability

$$\hat{T}^2 = \frac{1}{N_c^2 - 1} \frac{d\hat{\sigma}^{\text{incl}}}{dt}(gg^{PP} \rightarrow q\bar{q}) \Big/ \frac{d\hat{\sigma}}{dt}(gg \rightarrow q\bar{q}) \times P_a \times \sum_a \hat{\sigma}_a \quad (4.45)$$

where $\hat{\sigma}_a$ are the cut parton level cross sections calculated in the previous section.

Quark Exchange

It is more difficult to screen the colour triplet flow originated by the quark exchange which we deal with in the electroweak and QCD $Z + 2$ jet processes shown in Figs. 4.2c, 4.3c or 4.4a,b,c. For example, to screen the quark colour in Fig. 4.4 we have to replace the graphs Figs. 4.4a,b,c by those of Fig. 4.29. Due to the spin 1/2 nature of a quark, the large rapidity gaps

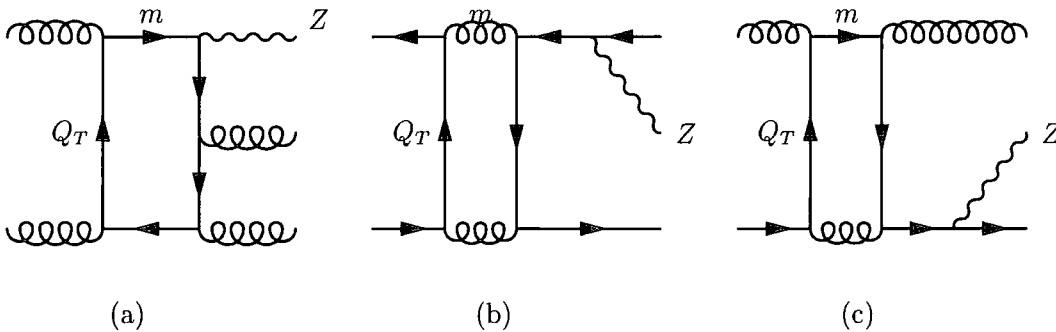


Figure 4.29: Screening of QCD dijet + Z production via quark exchange.

are suppressed at the *amplitude* level (in comparison with the corresponding Figs. 4.4a,b,c amplitude contribution) by the factor $e^{-\Delta\eta/2}$ (i.e. a factor $e^{-\Delta\eta}$ in the cross section). On the other hand, it is known that the loop with two t -channel fermions may contain a double logarithm (see [89, 90]). One logarithm comes from the transverse (Q_T) integration, while another logarithm (in the real part of the amplitude) originates from the dm^2/m^2 integral over the (virtual) mass of the upper s -channel particle in the loop (assuming that the contour of the Feynman integral is closed on the pole corresponding to the lower s -channel particle). In our kinematics, where a Z boson is emitted in the centre of the rapidity gap interval, we obtain a logarithm when the mass, m , runs from $m^2 = \max\{Q_T^2, \sqrt{\hat{s}m_{ZT}^2}\}$ up to $m^2 = \hat{s}$

(here \hat{s} is the incoming parton energy squared and $m_{ZT}^2 = m_Z^2 + |p_{TZ}|^2$). That is, the mass integral gives $\int \frac{dm^2}{m^2} \lesssim \frac{\Delta\eta}{2}$. The Q_T integration does not give a logarithm in the case of Fig. 4.29a, but for the amplitudes corresponding to Fig. 4.29b,c, a logarithmic integral appears in the domain $p_{T\text{jet}}^2 \ll Q_T^2 \ll \hat{s}^2/4$. Thus from the Fig. 4.29b,c loop integrals we may expect a $\frac{3}{8}(\Delta\eta)^2$ enhancement. However, with our large rapidity gap ($\Delta\eta \simeq 6$) the whole factor, $[\frac{\alpha_s}{\pi} \frac{3}{8}(\Delta\eta)^2 e^{-\Delta\eta/2}]^2 = 0.45(\frac{\alpha_s}{\pi})^2 \sim 10^{-3}$ is very small. Besides this, after the parton-level cuts described in Section 4.3.2 are applied, the original parton-level contribution of the diagrams with a (t -channel) quark exchange is strongly suppressed. Therefore we neglect these contributions. This is the reason why we have omitted to calculate the processes $q\bar{q} \rightarrow gg\bar{b}\bar{b}$ and $gg \rightarrow q\bar{q}\bar{b}\bar{b}$.

4.4.2 Soft Survival Probability

Having considered the survival of the gaps at the hadron level, we now move on to consider any soft interactions of the spectator partons.

We use the two-channel eikonal formalism mentioned in Section 3.5.2. This reproduces all the main features of the soft ($\sigma_{tot}, d\sigma_{el}/dt$) cross section data in the ISR–Tevatron energy range. The two channels of the eikonal correspond to two eigenstates which have different absorptive cross sections (i.e. different rescattering probabilities). Assuming the same (momentum and spatial) distributions of quarks and gluons in both components of the incoming proton wavefunction (that is, in both eigenstates of the eikonal) the model predicts for all our processes $\hat{S}^2 = 0.1$ at the LHC. In other words, by requiring gaps at the hadron level we decrease the cross section by an order of magnitude. At first sight, the gap survival probability $\hat{S}^2 = 0.1$ reflects

the rescattering of soft spectator partons and should, therefore, be universal for any process which has a gap⁸. However, this is not completely true. First, the value of \hat{S}^2 depends on the spatial distribution of parton spectators and therefore on the characteristic impact parameter, b_T , difference between the two colliding protons [60, 61]. For example, in the case of exclusive Higgs boson production, $pp \rightarrow p + H + p$ via photon-photon fusion, the transverse momenta of the photons are very small. Hence the impact parameter, b_T , is very large. The probability of soft rescattering in such a highly peripheral collision is small, and the value of \hat{S}^2 is close to one [64, 85]. Secondly, there is a difference in the momentum distributions of partons in a different (diffractive eigenstate) component of the incoming proton wavefunction; it is reasonable to expect that the component with a smaller cross section contains more valence quarks (and ‘hard’ large- x partons), whereas the component with a larger cross section has more low- x gluons. This possibility is discussed in [61]. In such an approach, the model describes the breakdown of factorisation, in that there is about a factor of ten difference between the ‘effective’ Pomeron structure functions measured in diffractive deeply inelastic interactions at HERA and diffractive high- E_T dijet hadroproduction at the Tevatron [53]⁹.

In our considerations, as the background $b\bar{b}$ -pairs are produced predominantly in gluon-gluon collisions, the gap survival probability for the QCD background is a little smaller than for $Z(H)$ -boson production via vector boson fusion where we deal with incoming quark-quark interactions (see Figs. 4.1, 4.2). Using the formalism of [61] a collaborator of the author (M.

⁸The only difference may be caused by the Sudakov-like form factor that accounts for the absence of QCD gluon bremsstrahlung in a specific hard subprocess.

⁹The difference is explained simply by the fact that the gap survival factor is $\hat{S}^2 \sim 0.1$ for proton-antiproton collisions, whereas $\hat{S}^2 \simeq 1$ in deep inelastic scattering.

G. Ryskin) obtains for the kinematics (cuts) described in Section 4.3,

$$\hat{S}_Z^2 = 0.31; \quad \hat{S}_H^2 = 0.31; \quad \hat{S}_{QCDb\bar{b}}^2 = 0.27. \quad (4.46)$$

These survival factors are much larger than in the original model [60] because for the case considered here, of large rapidity gaps and large jet transverse momenta, we select mainly fast incoming partons and valence quarks which belong to the second component of the proton wavefunction. This component has a smaller absorptive cross section¹⁰. In this case, the QCD background is additionally suppressed 2.5 times. Note that both versions of the model [61] describe the diffractive dijet CDF data [53] well enough. On the other hand, in processes with large rapidity gaps at the LHC, the uncertainty in the soft survival factor \hat{S}^2 may be rather large. It will therefore be important to study such a process experimentally. A promising way to study the survival probability \hat{S}^2 in different components of the incoming proton wave function (i.e. the dependence of \hat{S}^2 on the $p_{T\text{jet}}$ and rapidity cuts) is to measure QCD dijet production with rapidity gaps on either side of the dijet pair. Here the cross section is much larger (especially for gluon-gluon induced dijets) and it is easy to study the gap survival factor \hat{S}^2 under the various kinematic conditions: p_T of the fast (large η) jets, size of the rapidity gaps, dijet mass, etc. In this way we can emphasise the rôle of the incoming valence quarks, sea quarks or gluons in different x and scale $\mu^2 \sim p_T^2$ domains, and hence choose the configuration where one or other component of the wavefunction

¹⁰Under the extreme hypothesis that all valence quarks belong to the second (low σ_{abs}) component while gluons and sea quarks are concentrated in the first component (with a larger cross section) Ryskin obtains

$$\hat{S}_H^2 = \hat{S}_Z^2 = 0.26 \quad \text{and} \quad \hat{S}_{QCDb\bar{b}}^2 = 0.10.$$

dominates.

Note that, depending on the jet-finding algorithm, some soft hadrons may or may not be attributed to a particular b -jet. Therefore, one has to be more specific in the definition of the rapidity gap on the hadronic level in the presence of the high- p_T jets. It looks plausible to select the gap by the requirement not to have hadrons within the gap range, apart from the cones of a fixed size $\Delta R \equiv \sqrt{\Delta\eta^2 + \Delta\phi^2} \sim 1$ around the jet directions. In a real life experiment, jet-finding algorithms such as those mentioned in Section 1.5.3 should be utilised in optimising the value of ΔR . Soft survival factors, \hat{S}^2 , are practically independent of the ΔR value at $\Delta R \leq 2$ [82].

4.5 LHC Predictions

Fig. 4.30 shows the cross sections after hadronisation for central production of Higgs or Z with rapidity gaps and subsequent decay to $b\bar{b}$ as a function of $p_{T\min}$ of the proton remnant jets. It also shows the expected background of QCD $b\bar{b}$ events that display the same kinematical configuration. These are calculated using as a starting point the parton level cross sections after application of cuts, namely Figure 4.25 for Higgs production and Figure 4.26 for Z production. The QCD-induced cross sections (both the QCD Z production of Fig. 4.4d and the direct QCD $b\bar{b}$ production of Fig. 4.5) are then multiplied by the probability to screen out the colour octet contribution for the relevant initial state of either qq , qg or gg (Eq. 4.39). To take into account the fact that the $b\bar{b}$ pair in the background processes can only be produced in the colour singlet state the ordinary $gg \rightarrow b\bar{b}$ cross section is replaced by the pure singlet cross section, Eq. 4.44. Finally both the signals and backgrounds are multiplied by the relevant soft survival probability of Eq. 4.46.

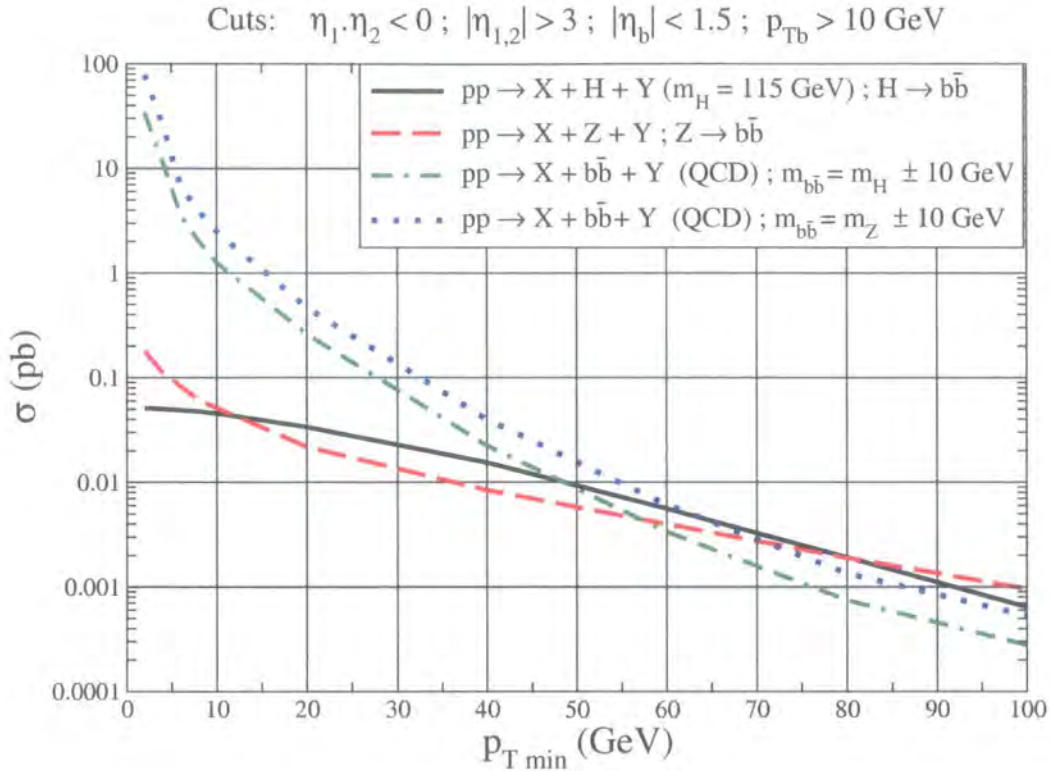


Figure 4.30: Hadron level cross sections for the LHC.

We see that, as long as we stay away from the low $p_{T \min}$ region, the signal for Higgs production is comparable with the QCD background, even exceeding it above $p_{T \min} = 50$ GeV. The cross section for Z production with rapidity gaps is less than that for Higgs production over most of the plot. This is because the branching fraction to $b\bar{b}$ is much lower than for the Higgs. Exceptions to this occur at low $p_{T \min}$ where the effect of the infrared singularity makes its presence felt and at very high $p_{T \min}$, explained by the fact that the parton-level Higgs cross section falls more rapidly, as shown in Fig. 4.6. The backgrounds show an extremely strong dependence on $p_{T \min}$, falling by five orders of magnitude as one varies $p_{T \min}$ from 2 GeV to 100 GeV. The QCD $b\bar{b}$ background with the invariant mass of the $b\bar{b}$ pair

taken around the Z mass is approximately 80% higher than that evaluated around the Higgs mass.

It should be noted that in these calculations we have taken $\alpha_S \equiv \alpha_S(M_Z^2)$. An argument could also be made that the characteristic scale should be that of the transverse momenta of the forward jets, i.e. $\alpha_S \equiv \alpha_S(p_{T\min}^2)$. This would affect the $\mathcal{O}(\alpha_S^4)$ backgrounds in such a way as to increase them by approximately 30% if we take the typical p_T to be 40 GeV.

4.5.1 Experimental Issues

The LHC is planned to operate at two luminosities during its running. The medium luminosity phase will occur for the first two years and will average $10^{33} \text{ cm}^{-2}\text{s}^{-1}$. This equates to an average of 2.3 inelastic interactions per bunch crossing. Hence the rapidity gaps will often be destroyed by these pile-up effects. During the high luminosity run ($10^{34} \text{ cm}^{-2}\text{s}^{-1}$) there will be, on average, 22 scatters per bunch crossing.

However, certainly in the medium luminosity phase, it is possible to use the detector information to reconstruct the gaps from the hard scatter [91]. The vertices of the individual collisions will be (non-uniformly) distributed along the beam axis in the interaction region over a distance of 10 – 20 cm. The precise tracking subdetectors of the experiments will, however, allow the reconstruction of vertex positions with a precision of a few tens of microns, and even soft tracks can be associated to their corresponding vertex with a precision of a fraction of a millimetre. Thus one can imagine an event selection that checks for rapidity gaps based on the charged particles associated with the proper vertex. Furthermore, the transverse energy of particles from the soft overlap events is generally low and, for example, considering only

particles with an E_T value larger than of order $1 - 2$ GeV may reveal the underlying rapidity gap of the hard scattering event [92]. Events thus selected will need to be subject to further scrutiny as this method ignores the possibility that these gaps in charged particle distributions may be destroyed by neutral particles.

Rapidity gaps in the events could thus be detectable by vertex and/or soft energy cuts for the data taken at medium luminosity. However, it is unlikely that these techniques can be used for the high luminosity phase or a SLHC type of luminosity of 10^{35} cm⁻²s⁻¹.

The predictions given in Fig. 4.30 should be modified to account for the b -tagging efficiency ε_b . This, in turn, is correlated with the probability $\mathcal{P}(g, q/b)$ to misidentify a gluon (or a light quark) jet as a b -jet. The rate of the gg -dijets exceeds the $b\bar{b}$ -yield by two orders of magnitude [64]. As discussed in [82], it is feasible to expect for the two b -jets $(\varepsilon_b)^2 = 0.6$ with $\mathcal{P}(g, q/b) = 0.01$.

In many previous studies of processes involving the identification of a rapidity gap at hadron colliders [93–95] a “minijet veto” has been used. In this study, we have been more stringent in our kinematical constraints and chosen to impose *hadron* free gaps rather than minijet free gaps.

4.6 Conclusions

The weak boson fusion mechanism can provide a promising way to detect a light Higgs boson at the LHC, see for example [65, 96, 97]. The selection of events with large rapidity gaps and energetic large p_T (quark) jets in the forward and backward directions allows the suppression of the QCD $b\bar{b}$ background down to a level comparable to the signal. Therefore, it becomes

feasible to observe a light Higgs boson via its main $H \rightarrow b\bar{b}$ decay mode in addition to the usually discussed $\tau\tau$ and WW^* channels, see for example [82].

The cross section for the production of a 115 GeV Higgs boson in association with rapidity gaps at the LHC is expected to be about 15 fb (for $p_T > 40$ GeV). Therefore, for an integrated luminosity of 30 fb^{-1} planned for the first two or three years of LHC running, about 400 events can be observed.

Note that our cuts were not finally optimised for the particular ATLAS/CMS conditions. Thus, the significance of the signal may be improved by allowing asymmetric configurations with some minimal $\Delta\eta$ between the high- p_T jets instead of the requirement $|\eta_{1,2}| \geq 3$, $\eta_1 \cdot \eta_2 \leq 0$. Such a kinematical choice was considered, for instance, in [65]. It is shown that this will noticeably improve the significance of the signal.

An important ingredient in the evaluation of both the signal and the background in the $b\bar{b} + 2$ forward jet events is the soft survival factor, \hat{S}^2 , defining the probability that the gaps survive the soft pp -scattering. As discussed in Chapter 3, though this factor can be computed within the framework of existing models for soft rescattering, it is always unwise to rely on the precision of models based on soft physics. Fortunately, the soft survival factor for the gaps surrounding $WW \rightarrow H$ fusion can be monitored experimentally by observing the closely related central production of a Z boson with the same rapidity gap and jet configuration [78, 79].

As was emphasised in [79, 93, 97], the $\tau\tau$ and WW^* decay channels with rapidity gap kinematics can give a rather high significance for the observation of a light Higgs. In the $\tau\tau$ case, the main background results from the tail in the $\tau\tau$ mass distribution generated by the $Z \rightarrow \tau^+\tau^-$ decay. Again, the experimental observation of Z boson central production allows one to control

and monitor such a background.

It is worthwhile to mention that the experimental determination of the gap survival factor in the processes under consideration is interesting in its own right, since it provides important information on the incoming proton wavefunction. Note that since the incoming partons in the subprocess $qq \rightarrow q + (b\bar{b}) + q$ are rather hard, the factor, \hat{S}^2 , depends on the model assumptions more sensitively than, for example, in the exclusive diffractive production case $pp \rightarrow p + b\bar{b} + p$, see [60,64]. As was demonstrated in Section 4.4.2 (see footnote 10) the results strongly depend on how the partons in the proton are distributed between the different diffractive eigenstates. Currently our information on these distributions is rather limited.

This Chapter concentrated on the detailed analysis of central Z boson production accompanied by rapidity gaps on either side and two forward jets at the LHC. The QCD background processes for $Z + 2$ jet production in the rapidity gap environment have been addressed in detail. We evaluated the soft survival factors \hat{S}^2 for various processes under consideration.

Finally, we note that it will be important to extend our work by incorporating a realistic Monte Carlo simulation, which will allow detector simulation to be included. We believe that the results presented here make such an effort worthwhile.

Chapter 5

Soft QCD Radiation as a Discriminator in Higgs Searches

In this Chapter we look at the vector boson fusion mode of Higgs production from an entirely different viewpoint. Rather than imposing a rapidity gap, restricting our considerations to those events where there is no hadronic activity in the gap region, we now relax our approach. We allow hadronic radiation from the jets and consider the probable distribution of leading order inter-jet QCD radiation. This allows us to quantify how ‘quiet’ the signal events are compared to the otherwise irreducible background events.

The distribution of soft hadrons or jets accompanying energetic final-state particles in hard scattering processes is governed by the underlying colour dynamics at short distances [98–103]. This phenomenon is known as Local Parton Hadron Duality (LPHD). The soft hadrons paint the colour portrait of the parton hard scattering, and can therefore act as a ‘partonometer’ [92, 98–113].

Since signal and background processes at hadron colliders can have very different colour structures (compare for example the s -channel colour singlet

process $gg \rightarrow H \rightarrow b\bar{b}$ with the colour octet process $q\bar{q} \rightarrow g^* \rightarrow b\bar{b}$, the distribution of accompanying soft hadronic radiation in the events provides a powerful additional diagnostic tool for identifying new physics processes.

Examples that have been studied in the literature in this way include Higgs production via gluon fusion [114], Z' production [107] and leptoquark [115] production. In each case, the new particle production process was shown to have its own particular colour footprint, distinctively different from the corresponding background process.

Quite remarkably, because of the property of LPHD (see for example [99, 103, 116]) the distribution of soft hadrons can be well described by the amplitudes for producing a single additional soft gluon. The angular distribution of soft particles typically takes the form of an ‘antenna pattern’ multiplying the leading order hard scattering matrix element squared. We will show this in detail later.

Thus we have in mind the following type of scenario. Suppose an invariant mass peak is observed in a sample of (tagged) $b\bar{b}$ events in which there are energetic forward jets, typical of the vector boson fusion production process. If such events do indeed correspond to Higgs production, then the distribution of accompanying soft radiation in the event, which we take to mean the angular distribution of hadrons or ‘minijets’ with energies of at most a few GeV, well separated from the beam and final state energetic jet directions, will look very different from that expected in background QCD production of $b\bar{b} + 2$ jet events. Again, the analogous process of $Z(\rightarrow b\bar{b}) + 2$ jet production can be used to calibrate the analysis, since these events are, as we shall see, also generally quieter than the QCD backgrounds.

Thus in this study we will consider the hadronic radiation patterns for the generic process of $b\bar{b} + 2$ forward jet production, where the (central)

$b\bar{b}$ originate either from a Higgs, a Z or from standard QCD production processes. We will again choose configurations (i.e. cuts on the rapidities and transverse momenta of the final-state particles) that maximise the Higgs signal to background ratio. These were specified in the previous Chapter.

This Chapter has the following structure. Firstly, we set out the general theoretical structure for leading order inter-jet soft QCD radiation and present an example calculation. Then we will consider the specific antenna patterns for Higgs and Z production accompanied by two forward jets. We will see that, for these colour singlet production processes, simple analytic expressions can be derived. We will also see that this is not the case for the more complicated QCD background processes. In Section 5.4 we will introduce a more general numerical technique that is capable of calculating these, and indeed arbitrarily complicated, processes. Section 5.5 summarises our results and presents our conclusions.

5.1 Amplitudes for Soft Gluon (and Photon) Emission

The amplitudes for soft gluon emission are almost identical to those for soft photon emission from charged fermions. The only differences being the coupling and the fact that we have a colour matrix in the former. Let us consider as an example emission from an initial state quark as in Fig. 5.1. Writing down the Feynman rules for a particular gluon polarisation, μ , and formally

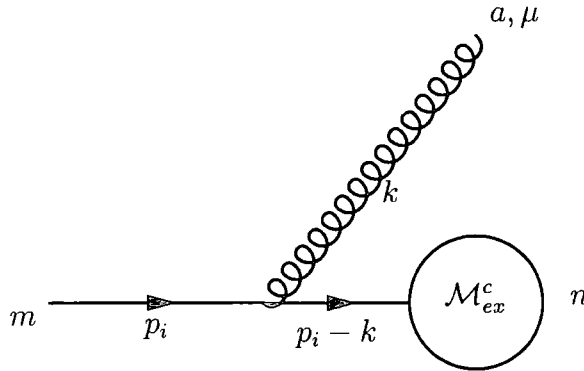


Figure 5.1: Soft gluon emission from an initial state quark.

taking the limit $k \rightarrow 0$ yields

$$\left[i \frac{\not{p}_i - \not{k} + m_i}{(p_i - k)^2 - m_i^2} \right] [-i g_s T_{mn}^a \gamma^\mu] u(p_i) \times \mathcal{M}_{ex}^c \xrightarrow{k \rightarrow 0} g_s T_{mn}^a \boxed{-\frac{p_i^\mu}{p_i \cdot k}} u(p_i) \times \mathcal{M}_{ex}^c, \quad (5.1)$$

where we denote the original amplitude without any radiation \mathcal{M}_{ex}^c . In taking the soft limit we have made use of the following facts

$$\begin{aligned} (\not{p}_i + m_i) \gamma^\mu u_i(p_i) &= [2p^\mu + \gamma^\mu (-\not{p}_i + m_i)] u(p_i) \\ &= 2p^\mu u(p_i) \quad \text{by virtue of the Dirac equation} \\ \text{and } \gamma^\mu \gamma^\nu &= 2g^{\mu\nu} - \gamma^\nu \gamma^\mu \text{ - the Clifford algebra.} \end{aligned} \quad (5.2)$$

Eq. (5.1) must be multiplied by the polarisation vector $\epsilon^\mu(\lambda)$ where λ denotes the gluon helicity such that the full amplitude for gluon emission off an incoming external line is

$$\mathcal{M}_i^g = -g_s T_{mn}^a \frac{p_i^\mu}{p_i \cdot k} \epsilon_\mu^*(\lambda) \times \mathcal{M}_i^0. \quad (5.3)$$

The boxed term in Eq. (5.1) is called the *eikonal factor*. It is easy to show that there is a relative change of sign if the emission occurs off an outgoing external line and also for emission off antiparticles.

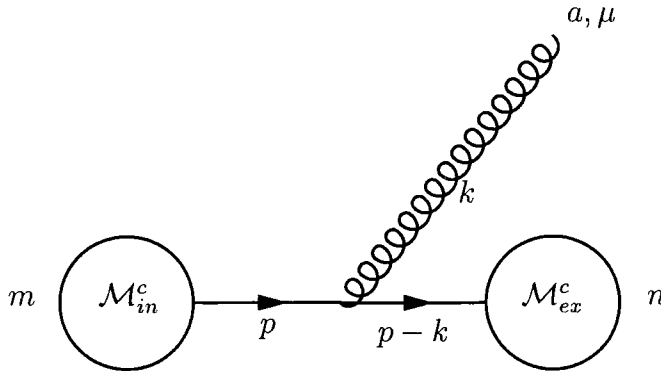


Figure 5.2: Soft gluon emission from an internal quark.

For emission off internal legs, shown in Fig. 5.2, the argument is slightly more subtle. The polarised amplitude reads

$$\mathcal{M}_{ex}^c i \frac{\not{p} - \not{k} + m}{(p-k)^2 - m^2} (-ig_s T_{mn}^a \gamma^\mu) i \frac{\not{p} + m}{p^2 - m^2} \mathcal{M}_{in}^c. \quad (5.4)$$

Defining the propagator denominators as¹

$$\mathcal{D}(q) \equiv \frac{1}{q^2 - m^2}, \quad (5.5)$$

the soft limit is

$$ig_s T_{mn}^a \mathcal{M}_{ex}^c (\not{p} - \not{k} + m) \gamma^\mu (\not{p} + m) \mathcal{M}_{in}^c \mathcal{D}(p) \mathcal{D}(p-k). \quad (5.6)$$

Now we note the fact that

$$\mathcal{D}(p) \mathcal{D}(p-k) = \frac{1}{2p \cdot k} \{ \mathcal{D}(p-k) - \mathcal{D}(p) \} \quad (5.7)$$

and deduce that this is finite in the soft gluon limit as long as the $\mathcal{D}(p)$ are finite, i.e. the internal lines are off-shell. Thus emission off internal lines does not contribute to the leading order QCD radiation pattern.

¹As before we omit Feynman $i\epsilon$ prescription.

In general, one can show that the complete matrix element can be written

$$\mathcal{M}^g(1, 2, \dots, l \rightarrow (l+1, l+2, \dots, n) + g(k)) = g_s \sum_{i=1}^n T_{mn}^a J_i^\mu \epsilon_\mu^{*a}(\lambda_i) \mathcal{M}^0, \quad (5.8)$$

with the current

$$J_i^\mu \equiv \eta_i g_s \frac{p_i^\mu}{p_i \cdot k}, \quad (5.9)$$

where $\eta_i = +(-)1$ for outgoing (incoming) external lines. The *antenna pattern* is then defined

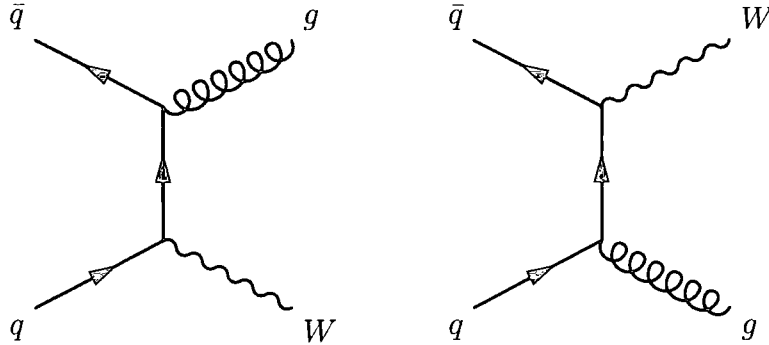
$$\mathcal{R} \equiv - \sum_{i,j} T_{mn}^a J_i^\mu T_{nm}^b J_{\mu j} \delta^{ab}, \quad (5.10)$$

where the minus sign arises from the fact that the polarisation vectors are normalised to negative unity, $\epsilon_\mu^* \epsilon^\mu = -1$. Therefore the radiation pattern is defined as the ratio of the $2 \rightarrow n+1$ and $2 \rightarrow n$ matrix elements using the soft gluon approximation in the former. As we work always in the massless quark limit, only cross terms in i, j contribute and we thus introduce the following shorthand [103]

$$[ij] \equiv \frac{p_i \cdot p_j}{(p_i \cdot k)(p_j \cdot k)}. \quad (5.11)$$

These antennae are the only ways that the soft gluon momentum enters the expressions.

It should be added that it is not hard to add masses into the method, see for example [115]. When one does this the ‘dead cone’ effect is observed where the mass cuts off the (otherwise formally divergent) radiation in close angular proximity to the external quark direction.

The Antenna Pattern for $q\bar{q} \rightarrow Wg$ Figure 5.3: Diagrams for $q\bar{q} \rightarrow Wg$.

As an example, we present the hadronic antenna pattern for $q\bar{q} \rightarrow Wg$. The leading order matrix element is

$$\overline{\sum} |\mathcal{M}|^2 (q(p_1)\bar{q}(p_2) \rightarrow W(p_3)g(p_4)) = \frac{g_s^2 g_W^2}{4} \left(1 - \frac{1}{N_c^2}\right) \frac{t^2 + u^2 + 2sm_W^2}{tu}, \quad (5.12)$$

where the Mandelstam variables are defined as usual. In the soft gluon approximation, the corresponding $2 \rightarrow 3$ matrix element is [99]

$$\overline{\sum} |\mathcal{M}|^2 (q\bar{q} \rightarrow Wg + g(k)) = g_s^2 N_c \left([14] + [24] - \frac{1}{N_c^2} [12] \right) \overline{\sum} |\mathcal{M}|^2 (q\bar{q} \rightarrow Wg). \quad (5.13)$$

Emission from the internal propagator does not contribute so there are three $2 \rightarrow 3$ diagrams for each $2 \rightarrow 2$ diagram - where the soft gluon attaches to a coloured external state. As the external particles are the same, the soft factor for each diagram is identical. There are three antennae - two which connect the gluon to the initial state and a $1/N_c^2$ suppressed antenna connecting the initial state quarks. We can see that the antennas factor out of the $2 \rightarrow 2$ matrix element in this case

5.2 Experimental Verification

Confirmation of the validity of this approach comes from studies of the production of soft hadrons and jets accompanying large E_T jet and W +jet production by the CDF [117] and D0 collaborations [118] at the Fermilab Tevatron. The latter results are shown in Fig. 5.4. The abscissa is the ratio of multiplicities in back-to-back calorimeter towers around the jet and W . The mantissa, $\beta = \sin \theta$, where θ is the angle with respect to the event plane, thus we rotate from $\beta = 0$ which is collinear to the jets, to $\beta = \pi/2$, perpendicular to the jets and the initial state. The maximum occurs in the event plane, this is because of the colour string connecting the jet with the initial state. The ratio recedes to unity perpendicular to the event plane where no colour strings exist. The fourth quadrant shows the LPHD prediction. This is obtained by taking the ratio of the antenna pattern defined in Eq. (5.13) at back-to-back phase space points as one rotates in β . The effect is entirely analogous to that for $e^+e^- \rightarrow q\bar{q}g$ where colour flow dynamics, known as the *string* or *drag* effect in that case, lead to a depletion of soft radiation between the quark and antiquark.

5.3 Hadronic Antenna Patterns for Higgs and $Z + 2$ Jet Production

5.3.1 Higgs and Electroweak Z Production

The signal process we are interested in is Higgs production via vector boson fusion, shown in Fig. 4.1, with subsequent decay of the Higgs to $b\bar{b}$. Furthermore, we restrict our considerations to the case where the outgoing quark

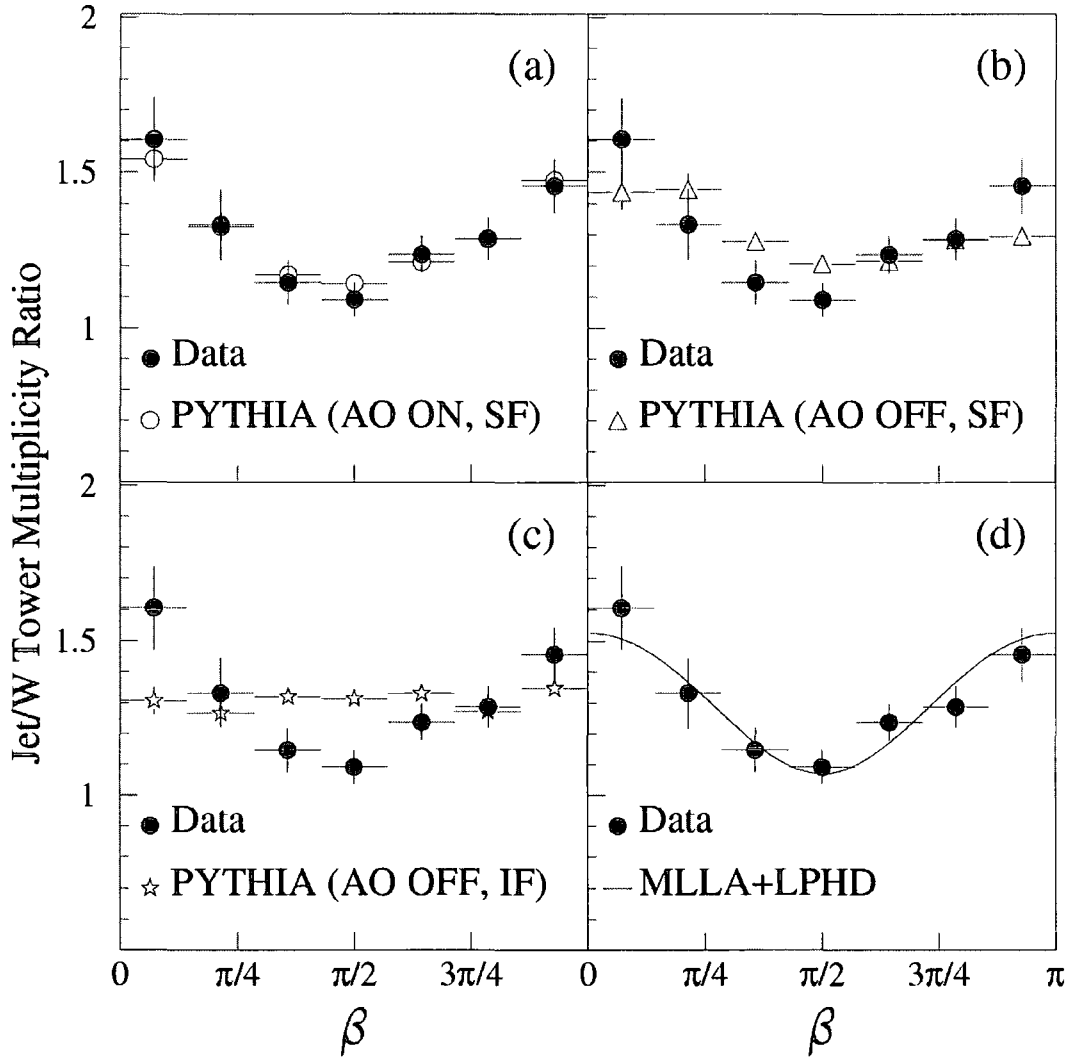


Figure 5.4: LPHD prediction and data compared for $W + \text{jet}$ events at $D\bar{O}$.

jets are forward in rapidity and the Higgs decay products are central in the detector. Again, we work in the zero width approximation for the Higgs and Z . As vector boson fusion involves no colour flow in the t -channel, the radiation pattern is simply that of the $2 \rightarrow 2$ process $qq' \rightarrow qq'$, with an additional colour disconnected $b\bar{b}$. These were calculated in [107]. For the signal $q(p_1) q'(p_2) \rightarrow q(p_3) q'(p_4) + g(k)$ we have

$$\overline{\sum} |\mathcal{M}|^2 = \frac{g_s^6 C_F}{N_c} \left(\frac{s^2 + u^2}{t^2} \right) 2C_F([13] + [24]), \quad (5.14)$$

with $s \equiv (p_1 + p_2)^2$, $t \equiv (p_1 - p_3)^2$, $u \equiv (p_1 - p_4)^2$.

We then normalise this by the matrix element for the leading order process $q(p_1) q'(p_2) \rightarrow q(p_3) q'(p_4)$:

$$\overline{\sum} |\mathcal{M}|^2 = \frac{g_s^4 C_F}{N_c} \left(\frac{s^2 + u^2}{t^2} \right). \quad (5.15)$$

Note that in this particular case, the $2 \rightarrow 3$ matrix element in the soft gluon limit factorises into the form $(2 \rightarrow n \text{ matrix element}) \times (\text{antenna factor})$. This feature is *not* universal, being restricted to only very simple cases such as this. The antenna pattern is then

$$\mathcal{R}(qq' \rightarrow qq') = g_s^{-2} \frac{|\overline{\mathcal{M}}_3|^2(qq' \rightarrow qq' + g)}{|\overline{\mathcal{M}}_2|^2(qq' \rightarrow qq')} = 2C_F([13] + [24]). \quad (5.16)$$

As we are working in the zero width approximation² we can include the decay of the Higgs into (massless) $b\bar{b}$ by simply adding the antenna for this colour disconnected part. The hadronic radiation pattern for $q(p_1) q'(p_2) \rightarrow$

²Actually our analysis is formally correct provided that $\Gamma_H \ll E_g$ where E_g is the typical soft gluon/hadron energy, i.e. the Higgs lives long enough to prevent any interference between gluon emission before and after the Higgs decays. In any case, such interference would occur only in higher orders in α_s and is colour suppressed.

$q(p_3) q'(p_4) H ; H \rightarrow b(p_5) \bar{b}(p_6)$ is then

$$\mathcal{R}(H) = 2C_F([13] + [24] + [56]). \quad (5.17)$$

In order to visualise the pattern, we must specify the kinematics and pick a relevant configuration for the incoming and outgoing particles. We label the four-momenta by

$$a(p_1) + b(p_2) \rightarrow c(p_3) + d(p_4) + \cdots + g(k), \quad (5.18)$$

where the gluon is soft relative to the other large- E_T final state partons, i.e. $k \ll E_T$. We ignore the gluon momentum in the energy-momentum constraints, work in the overall parton centre of momentum frame, fix the Higgs to be at rest in that frame and its decay products at $(\eta_b, \phi_b) = (0, \pi/2)$ and $(0, 3\pi/2)$. With the notation $p^\mu = (E, p_x, p_y, p_z)$, the momenta are then

$$\begin{aligned} p_1^\mu &= (m_H/2 + E_T \cosh \eta_{\text{jet}}, 0, 0, m_H/2 + E_T \cosh \eta_{\text{jet}}), \\ p_2^\mu &= (m_H/2 + E_T \cosh \eta_{\text{jet}}, 0, 0, -m_H/2 - E_T \cosh \eta_{\text{jet}}), \\ p_3^\mu &= (E_T \cosh \eta_{\text{jet}}, 0, E_T, E_T \sinh \eta_{\text{jet}}), \\ p_4^\mu &= (E_T \cosh \eta_{\text{jet}}, 0, -E_T, -E_T \sinh \eta_{\text{jet}}), \\ p_H^\mu &= (m_H, 0, 0, 0), \\ p_b^\mu &= (m_H/2, m_H/2, 0, 0), \\ p_{\bar{b}}^\mu &= (m_H/2, -m_H/2, 0, 0), \\ k^\mu &= (k_T \cosh \eta_g, k_T \sin \phi_g, k_T \cos \phi_g, k_T \sinh \eta_g). \end{aligned} \quad (5.19)$$

This is the appropriate form for studying the angular distribution of the soft gluon, parametrised by η_g and ϕ_g . Using the kinematics of Eq. (5.19) with

Eq. (5.17) gives

$$\begin{aligned} \mathcal{R}(H) = & \frac{2C_F}{k_T^2} \left\{ \frac{\cosh \eta_{\text{jet}} - \sinh \eta_{\text{jet}}}{(\cosh \eta_g - \sinh \eta_g)(\cosh \eta_{\text{jet}} \cosh \eta_g - \cos \phi_g - \sinh \eta_{\text{jet}} \sinh \eta_g)} \right. \\ & + \frac{\cosh \eta_{\text{jet}} - \sinh \eta_{\text{jet}}}{(\cosh \eta_g + \sinh \eta_g)(\cosh \eta_{\text{jet}} \cosh \eta_g + \cos \phi_g + \sinh \eta_{\text{jet}} \sinh \eta_g)} \\ & \left. + \frac{2}{(\cosh \eta_g - \sin(\phi_g + \pi))(\cosh \eta_g + \sin(\phi_g + \pi))} \right\} \end{aligned} \quad (5.20)$$

Note that the result is independent of E_T and m_H and that collinear singularities are situated at $(\eta_g, \phi_g) = (\eta_{\text{jet}}, \pi)$, $(-\eta_{\text{jet}}, 0)$, $(0, \pi/2)$ and $(0, 3\pi/2)$.

As an illustration, Figure 5.5 shows $k_T^2 \mathcal{R}(H)$ with $\eta_{\text{jet}} = 3.5$.

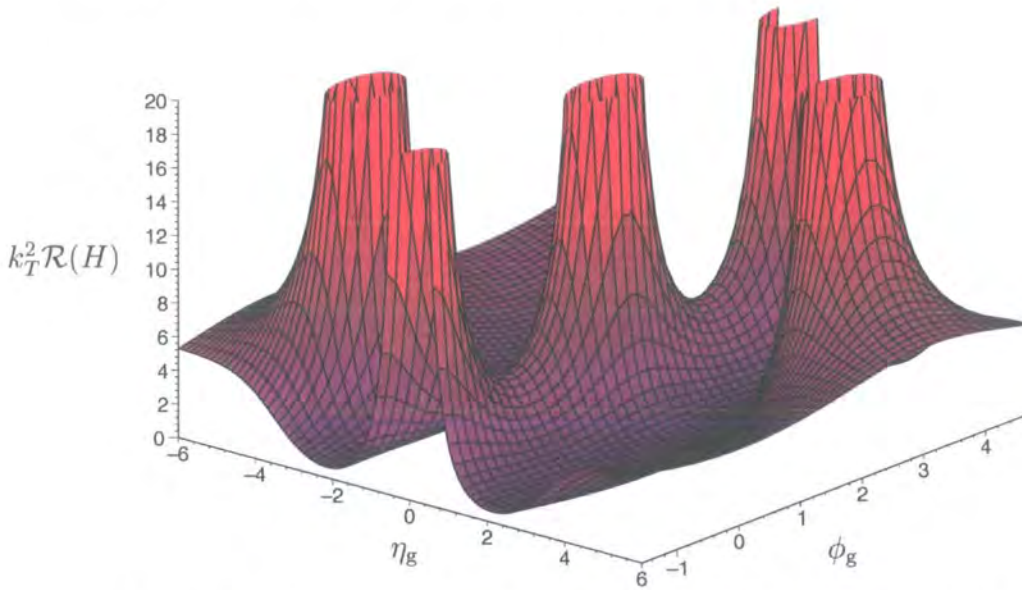


Figure 5.5: Antenna pattern for $qq' \rightarrow qq'H$; $H \rightarrow b\bar{b}$ with $\eta_{\text{jet}} = 3.5$.

One can clearly see that a colour connection exists between the initial state parton p_1 and final state jet p_3 , similarly with p_2 and p_4 , and also between the b -quark jets. The antenna pattern is small between the jets and the b 's as there is no colour connection between these. The emission of soft gluons in the 'rapidity gaps' decreases as the gap widens. This is illustrated in the case without the b -quark antenna (Fig. 5.6), which shows the antenna

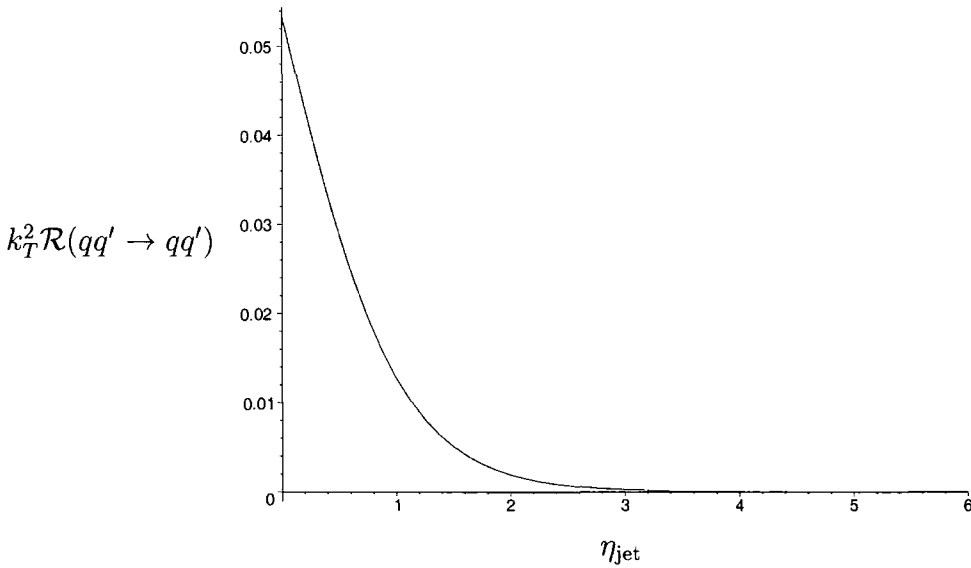


Figure 5.6: The point $(\eta_g, \phi_g) = (0, \pi/2)$ in $\mathcal{R}(qq' \rightarrow qq')$ as one varies η_{jet} .

pattern at $(\eta_g, \phi_g) = (0, \pi/2)$ as a function of η_{jet} .

Next we consider the analogous electroweak Z production process (Fig. 4.2), which, as we showed earlier, can be used to calibrate the Higgs production process. In this case the variety of diagrams at leading order means that there is no exact eikonal factorisation. However in the kinematic limit we are interested in — forward jets and central Z production — the dominant amplitude is again the one involving t -channel W exchange, i.e. $WW \rightarrow Z$, and the antenna pattern is trivially identical to that for Higgs production. We will prove this result, and consider its implications, when we discuss how to calculate antenna patterns numerically below.

5.3.2 QCD Z Production

In practice, $Z+2$ jet production can also occur by $\mathcal{O}(\alpha_s^2 \alpha_W)$ QCD production involving t -channel gluon exchange, see Fig. 4.4d. Because of the different colour structure of such diagrams we would expect a very different antenna pattern. Once again there is no exact factorisation of an overall soft gluon

form factor and therefore no simple expression for the radiation pattern. However, as for electroweak Z production the factorisation is restored in the forward jet – central Z limit, in which case the antenna pattern is identical to that for the QCD $\mathcal{O}(\alpha_s^2)$ $qq' \rightarrow qq'$ production process [107], i.e.

$$\mathcal{R}(QCD Z) \rightarrow 2C_F([14] + [23]) + \frac{1}{N_c}[12; 34] + 2C_F[56], \quad (5.21)$$

where

$$[ij; kl] \equiv 2[ij] + 2[kl] - [ik] - [il] - [jk] - [jl]. \quad (5.22)$$

Substituting the kinematics of Eq. (5.19) and plotting the resulting analytic expression with $\eta_{\text{jet}} = 3.5$, one obtains Figure 5.7.

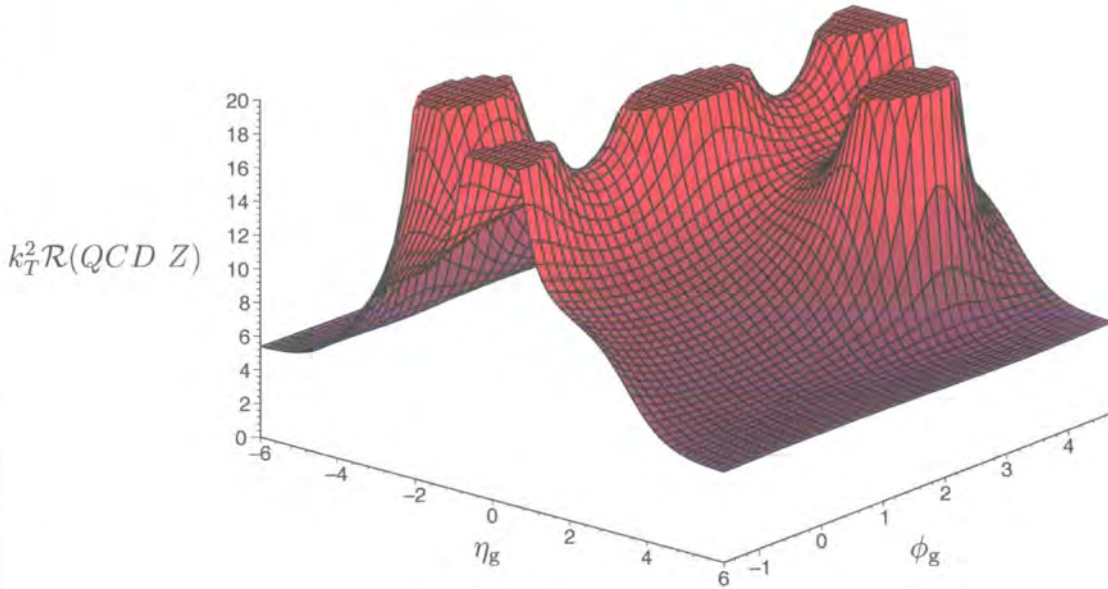


Figure 5.7: Antenna pattern for $qq' \rightarrow qq' Z$ (QCD); $Z \rightarrow b\bar{b}$ with $\eta_{\text{jet}} = 3.5$.

Before commenting on the differences, we note that both Figures 5.5 and 5.7 exhibit the same limiting behaviour

$$\lim_{|\eta_g| \rightarrow \infty} k_T^2 \mathcal{R}(H, QCD Z) = 4C_F, \quad (5.23)$$

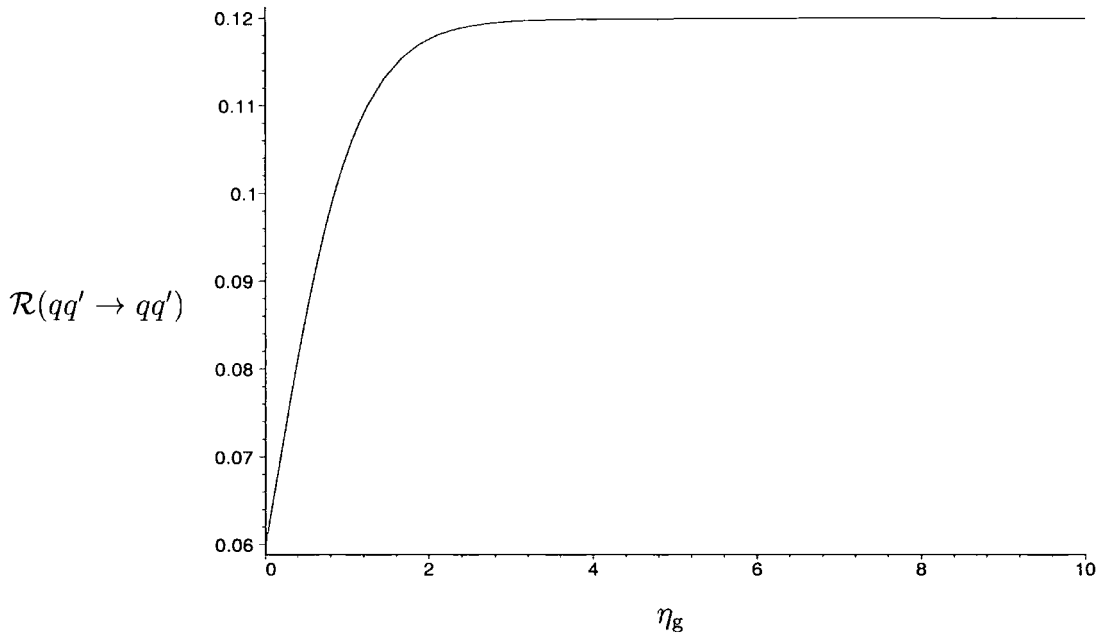


Figure 5.8: The point $(\eta_g, \phi_g) = (0, 0)$ in $\mathcal{O}(\alpha_s^2)$ $qq' \rightarrow qq'$ as the rapidity of the forward jets is varied.

as a consequence of both processes having initial state quarks. Of course $gg \rightarrow ggZ$ also contributes to $Z + 2$ jet production, and this will have a different colour structure from $qq \rightarrow qqZ$. For purposes of comparison with the Higgs case, we only consider quark induced production in this Section. Figures 5.5 and 5.7 are also identical as one approaches the collinear singularities corresponding to the final state b -jets:

$$\lim_{(\eta_g, \phi_g) \rightarrow (\eta_{\text{jet}}, \phi_{\text{jet}})} k_T^2 \mathcal{R}(H, QCD Z) \rightarrow 4C_F \frac{1}{\cosh^2(\eta_g - \eta_{\text{jet}}) - \cos^2(\phi_g - \phi_{\text{jet}})}. \quad (5.24)$$

The difference in the colour flow shows up in the region between the two final state forward quark jets, as expected. Figure 5.8 shows this to be the case for simple QCD dijet production, as the jets become more forward, the antenna flattens out in the centre of the detector to a constant value. Taking the ratio of the two central boson production patterns makes the colour flow difference plain (Fig. 5.9). The maximum difference occurs at

$(\eta_g, \phi_g) = (-4.4, 0)$ and $(\eta_g, \phi_g) = (4.4, \pi)$ when the ratio attains the value 2.3. This shows the colour connection between the initial state (at $\eta_g = \pm\infty$) and the forward jets in the Higgs production case that is suppressed by a factor $\mathcal{O}(\frac{1}{N_c^2})$ in the QCD Z -production case. Another interesting phase space point is at $(\eta_g, \phi_g) = (0, 0)$, i.e. the central region transverse to the $b\bar{b}$ axis. Here the radiation pattern increases by a factor of three going from Higgs to QCD Z production, indicating the presence of an additional underlying colour connection in the latter case.

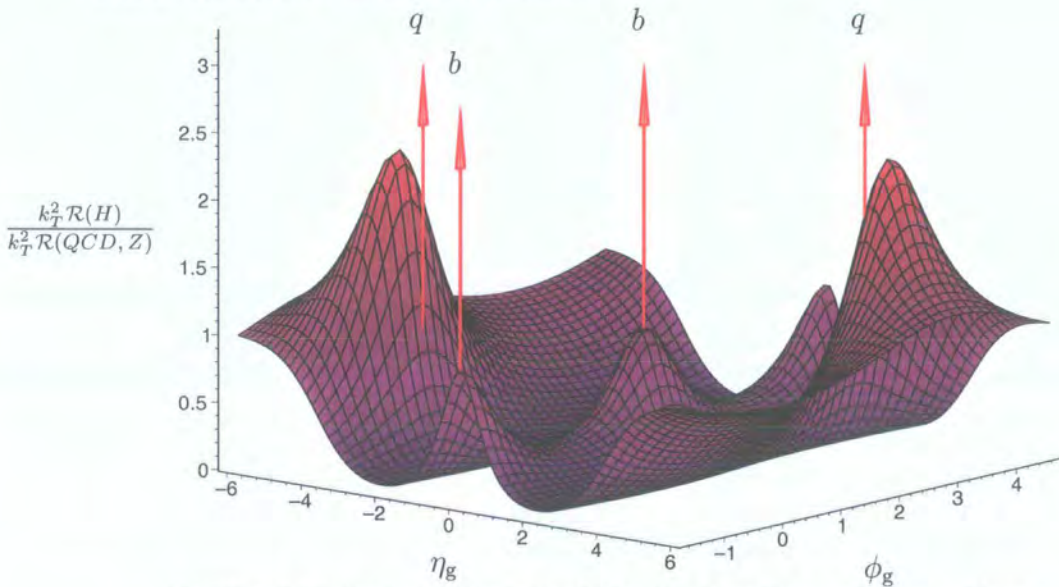


Figure 5.9: Ratio of Higgs to QCD Z production antenna patterns.

5.4 Numerical Hadronic Antenna Patterns

The dominant backgrounds considered in Chapter 4 to the signal processes explored in the previous section comes from QCD $\mathcal{O}(\alpha_s^4) b\bar{b} + 2$ jet production when $m_{b\bar{b}} \sim m_{H,Z}$ ³. Sample diagrams of which are shown in Fig. 4.5. There is clearly no unique and simple colour flow associated with these di-

³We are not discussing here the background caused by a possible misidentification of the gluons as b jets. For a recent treatment of this see [82].

agrams, and hence no compact analytic antenna pattern can be derived. This is an example of a situation where there is no factorisation of the form $(2 \rightarrow 4 \text{ matrix element}) \times (\text{antenna factor})$. However we can instead use a purely numerical method in which we compare the values of the $2 \rightarrow n$ and $2 \rightarrow n + 1$ matrix elements at each point in phase space, their ratio in the soft gluon limit defining the antenna pattern. In order to verify that this methodology works, and in particular to establish how soft the gluon has to be before the limiting pattern is reached to some level of precision, we first make a numerical evaluation of the analytic radiation patterns discussed in the previous section.

5.4.1 Comparison of Numerical and Analytic Antenna Patterns for Signal Processes

Unlike the analytic case, where we can simply ignore the momentum of the soft gluon in assigning a kinematic configuration that respects momentum conservation, we must account for the numerically finite gluon momentum in evaluating the matrix elements. Thus there is a degree of arbitrariness introduced. We choose to assign the momenta such that the central boson or $b\bar{b}$ system cancels the 3-momentum of the soft gluon. In other words

$$p_{Z,H,b\bar{b}}^\mu = \left(\sqrt{m_{Z,H}^2 + k^2}, -\underline{k} \right). \quad (5.25)$$

Therefore the value of the antenna pattern depends on the specific k_T that we choose for the soft gluon, but in such a way that $k_T^2 \mathcal{R}$ tends to a finite limit as $k_T \rightarrow 0$. Figure 5.10 illustrates this by taking the ratio of the numerical $qq' \rightarrow qq'H$ antenna pattern with the analytic $qq' \rightarrow qq'$ antenna

pattern for $k_{Tg} = 1$ GeV. The ratio is close to unity, except when the gluon rapidity is very large. In this region the ‘soft’ gluon carries a significant amount of energy and begins to distort the overall kinematics. For numerical purposes only, as a formal check that this effect is under control, we can set k_{Tg} to be sufficiently (and artificially) small to make sure the analytic result is recovered everywhere. Thus Fig. 5.11 shows the same ratio for $k_{Tg} = 10^{-5}$ GeV – no deviation from unity is now discernible. Note that we will always use $k_{Tg} = 1$ GeV in making predictions for the antenna patterns using the numerical treatment. Since our ultimate aim is to compare *two* numerically generated antenna patterns in signal to background studies, the discrepancies at large gluon rapidity visible in Fig. 5.10 will exactly cancel in the comparison.

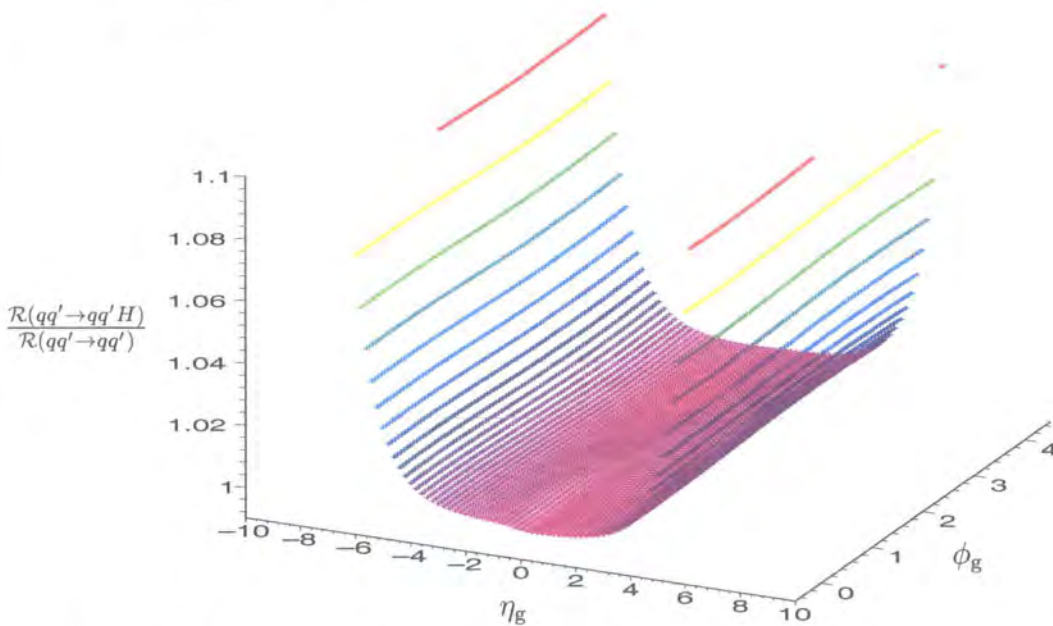


Figure 5.10: Ratio of numerical $qq' \rightarrow qq'H$ to analytic $qq' \rightarrow qq'$ antenna patterns with $|\eta_{\text{jet}}| = 2$ and $k_{Tg} = 1$ GeV.

As already pointed out, the antenna pattern for the full electroweak $qq' \rightarrow qq'Z$ process is *not* given by the simple analytic approximation, except when the jets are far forward. We can now illustrate this using the numerical

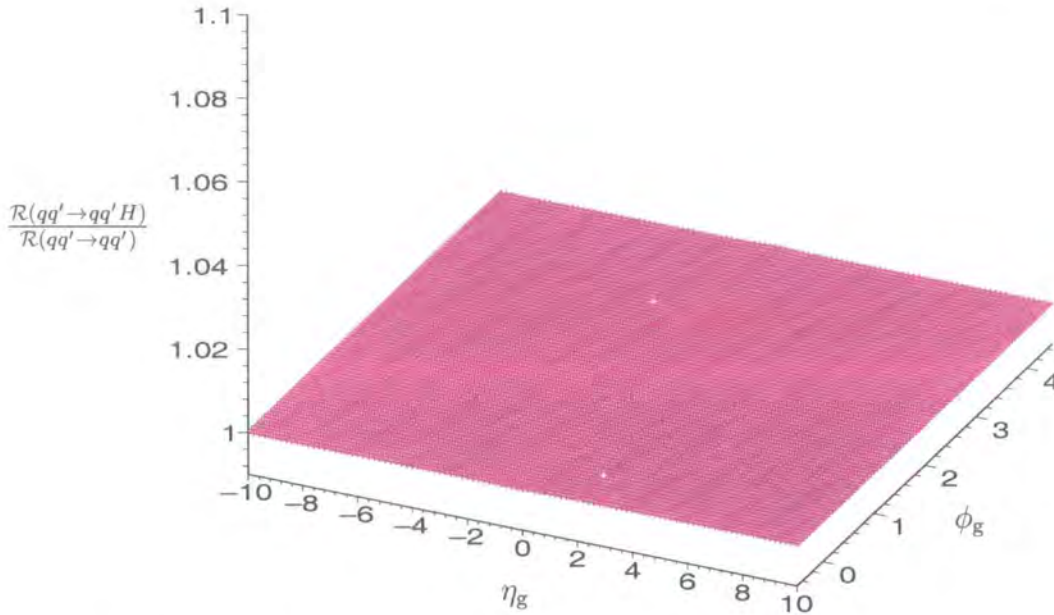


Figure 5.11: Ratio of numerical $qq' \rightarrow qq'H$ to analytic $qq' \rightarrow qq'$ antenna patterns with $|\eta_{\text{jet}}| = 2$ and $k_{Tg} = 10^{-5}$ GeV.

method. Thus Figs. 5.12 and 5.13 show the ratio of the numerical electroweak $qq' \rightarrow qq'Z$ antenna pattern with the analytic electroweak $qq' \rightarrow qq'$ antenna pattern for the choice of $|\eta_{\text{jet}}| = 2$ and $|\eta_{\text{jet}}| = 4$ with $k_T = 10^{-5}$ GeV. In the former case, the agreement with the analytic antenna pattern is only at the 10% level. The discrepancy is due to the contribution of the Z bremsstrahlung diagrams (Fig. 4.2b) in the numerical case. However, as one forces the quark jets to be more forward the discrepancy decreases. Therefore, as long as we require the jets to be forward (i.e. $|t| \ll \sqrt{s}$), the analytic approximation is valid.

Figures 5.14 and 5.15 show the same qualitative effect in the QCD mediated Z production case. The deviation from our approximation that $|t| \ll \sqrt{s}$ is noticeably less than in the electroweak case. The reason for this is that in the electroweak case we are kinematically disturbing a delicate interplay between the numerator and the denominator in the term describing the colour

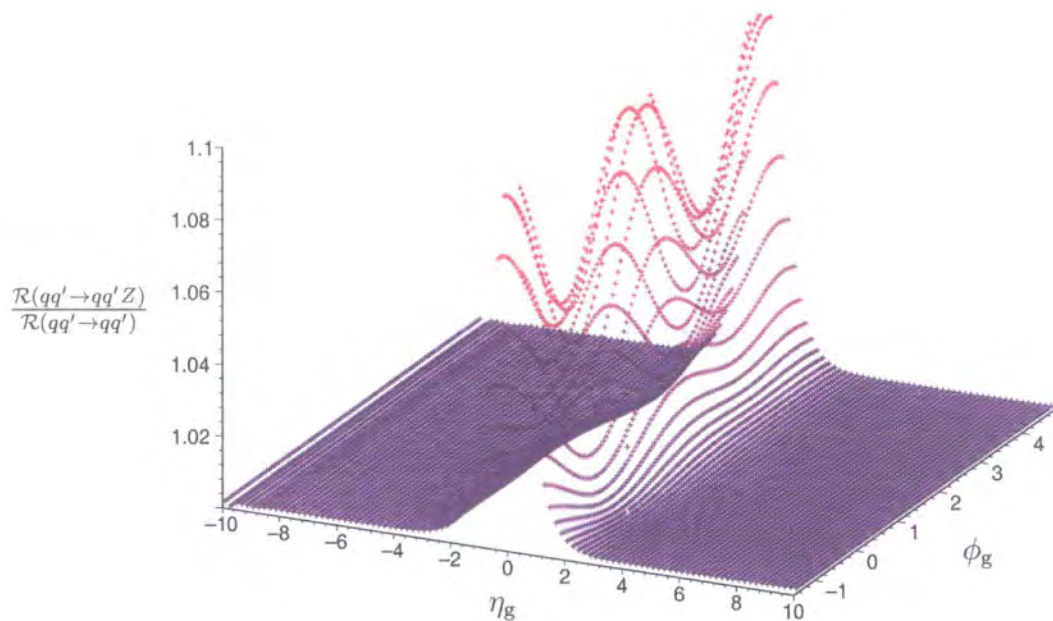


Figure 5.12: Ratio of numerical EW $qq' \rightarrow qq'Z$ to analytic $qq' \rightarrow qq'$ antenna patterns with $|\eta_{\text{jet}}| = 2$ and $k_{Tg} = 10^{-5}$ GeV.

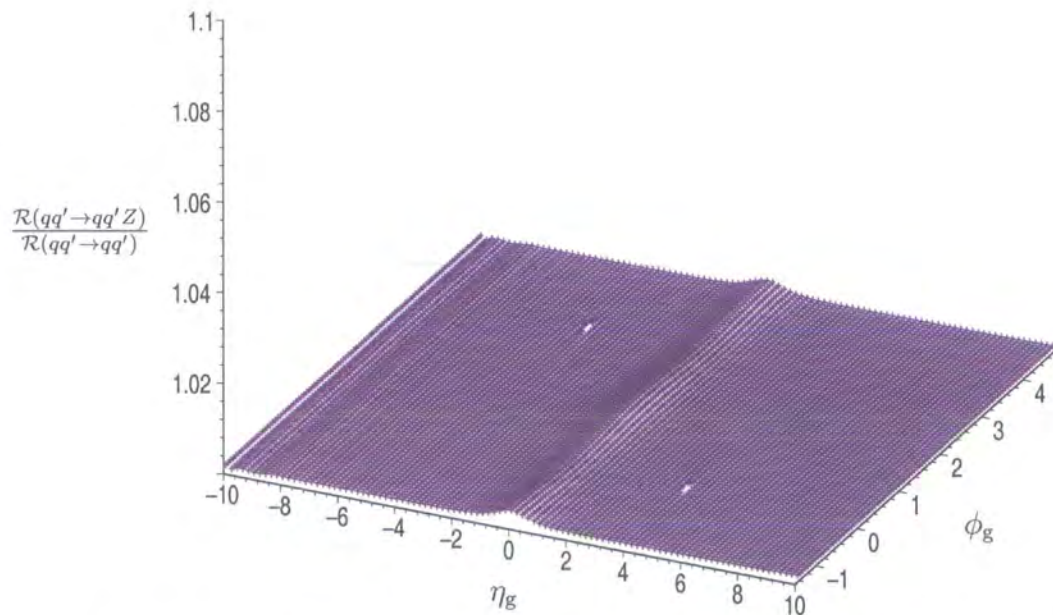


Figure 5.13: Ratio of numerical EW $qq' \rightarrow qq'Z$ to analytic $qq' \rightarrow qq'$ antenna patterns with $|\eta_{\text{jet}}| = 4$ and $k_{Tg} = 10^{-5}$ GeV.

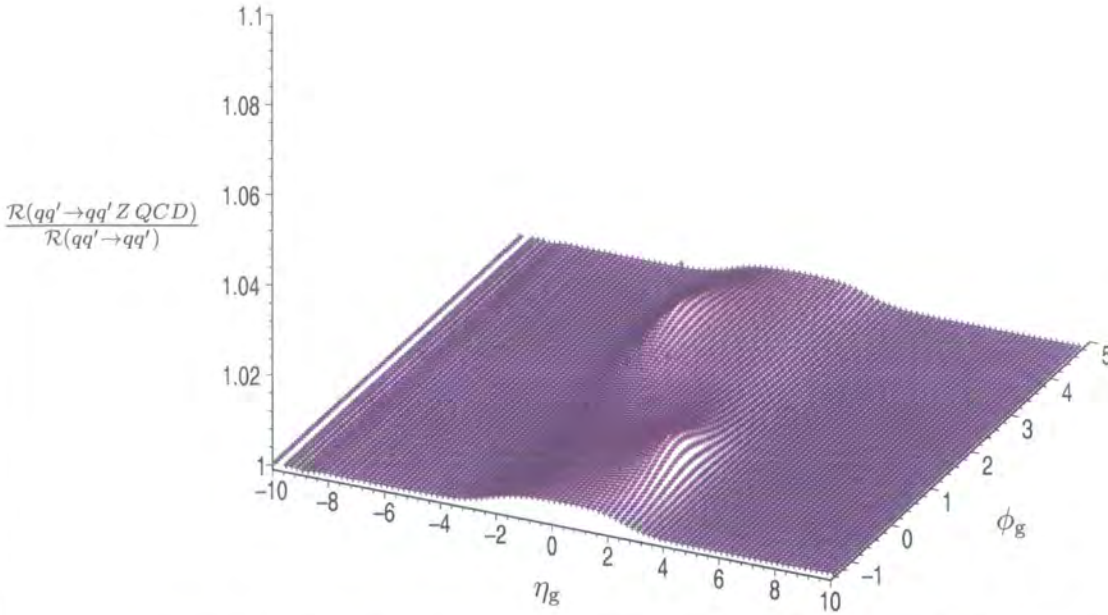


Figure 5.14: Ratio of numerical QCD $qq' \rightarrow qq' Z$ to analytic $qq' \rightarrow qq'$ antenna patterns with $|\eta_{\text{jet}}| = 2$ and $k_{Tg} = 10^{-5}$ GeV.

connection between p_1 and p_3 ,

$$[13] = \frac{p_1 \cdot p_3}{(p_1 \cdot k)(p_3 \cdot k)}. \quad (5.26)$$

In particular, due to the smallness of the numerator, this contribution is strongly suppressed for the radiation outside the narrow cones around the directions of the incoming and outgoing partons. Contrast this with the QCD Z production case where the dominant colour connection is between p_1 and p_4 ,

$$[14] = \frac{p_1 \cdot p_4}{(p_1 \cdot k)(p_4 \cdot k)}. \quad (5.27)$$

Here the numerator is not small. This cancellation is therefore more stable and our kinematic disturbance has less effect.

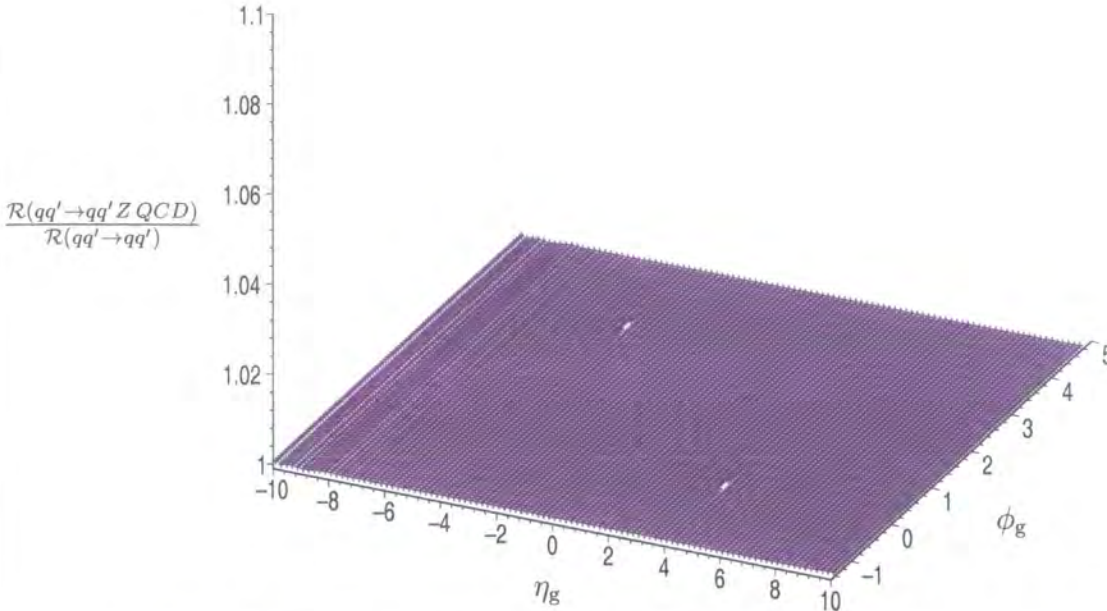


Figure 5.15: Ratio of numerical QCD $qq' \rightarrow qq'Z$ to analytic $qq' \rightarrow qq'$ antenna patterns with $|\eta_{\text{jet}}| = 4$ and $k_{Tg} = 10^{-5}$ GeV.

5.4.2 Numerical Antenna Patterns for Background Processes

Figure 5.16 shows the numerical antenna pattern for the QCD mediated process $qq' \rightarrow qq'b\bar{b}$. We will again focus mainly on the background process with initial state quarks, to allow comparison with the signal processes. In any case, the typical $\sqrt{\hat{s}}$ of the parton-level process is typically several TeV at the LHC⁴, so we are working at high x and quark initiated processes will dominate. Therefore the antenna patterns for the signal and background processes become identical near the beam and final state b -quark directions, being dominated by the (universal) collinear singularity for emission off quark lines.

Figure 5.17 shows the radiation pattern for the background QCD process $gg \rightarrow qg b\bar{b}$ with $|\eta_{\text{jet}}| = 4$ and $k_{Tg} = 1$ GeV. As expected, the pattern is much

⁴For example, from Eq. (5.19), $\sqrt{\hat{s}} \simeq m_H + 2E_T \cosh \eta_{\text{jet}} \simeq 2.8$ TeV for $E_T = 50$ GeV $m_H = 120$ GeV and $\eta_{\text{jet}} = 4$.

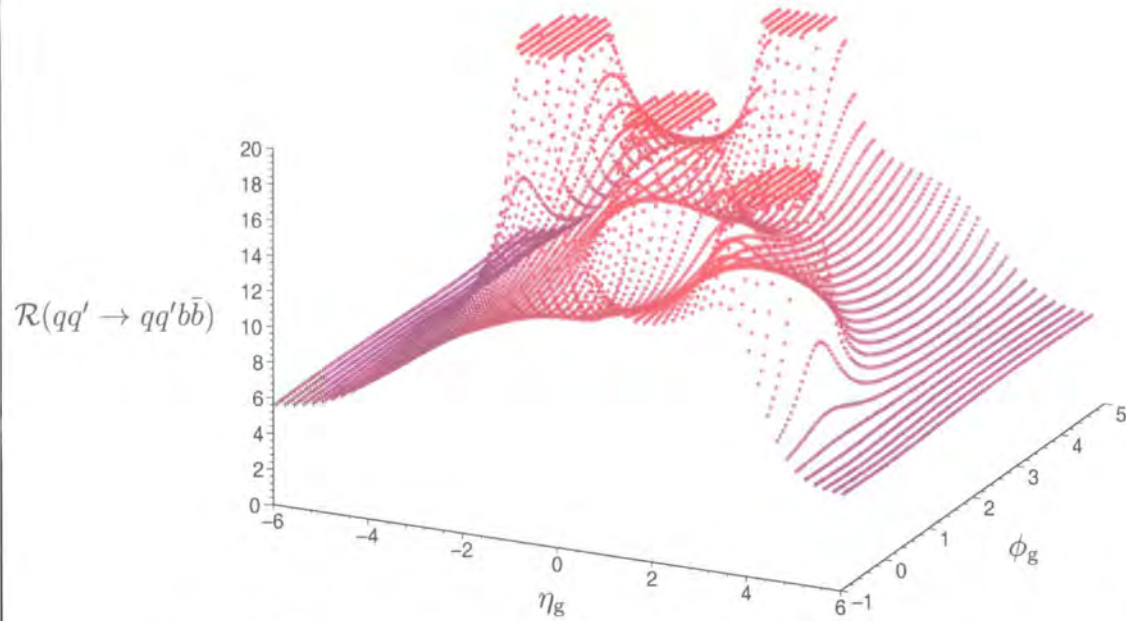


Figure 5.16: Numerical antenna pattern for $qq' \rightarrow qq'bb\bar{b}$ with $|\eta_{\text{jet}}| = 4$ and $k_{Tg} = 1$ GeV.

more complicated than that for the signal H or Z production processes. Colour strings can now connect many more pairs of initial and final state particles, and the overall level of radiation is higher as a result. However in the directions of the incoming and outgoing partons, the distribution of soft radiation is the same as that for the signal processes. Thus, in particular, the distribution approaches $4C_F$ for large positive η_g , cf. Eq. (5.23).

For completeness, we show in Figs. 5.17 – 5.20 the corresponding antenna patterns for the other QCD $2 \rightarrow 2 + (b\bar{b})$ processes. The most obvious differences are in the size of the distributions near the incoming and outgoing partons, where the limiting $4C_F$ behaviour for emission off quarks is replaced by $4C_A$ for emission off gluons.

Fig. 5.21 shows the ratio between the antennas for $qg \rightarrow qgbb\bar{b}$ and $qq' \rightarrow qq'bb\bar{b}$. The gluon emerges with negative rapidity. The ratio is $C_A/C_F = 9/4$ in the direction of radiation from the initial state gluon and rises to a value of 3.5 on the beamline side of the outgoing gluon jet, this is because radiation

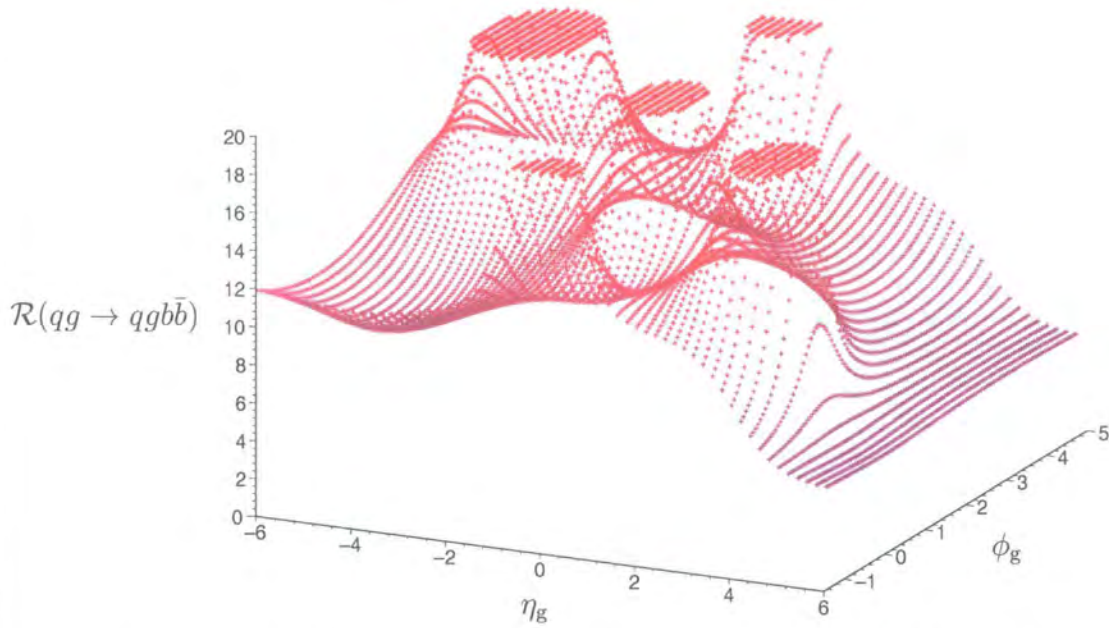


Figure 5.17: Numerical antenna pattern for $qg \rightarrow qgb\bar{b}$ with $|\eta_{\text{jet}}| = 4$ and $k_{Tg} = 1$ GeV.

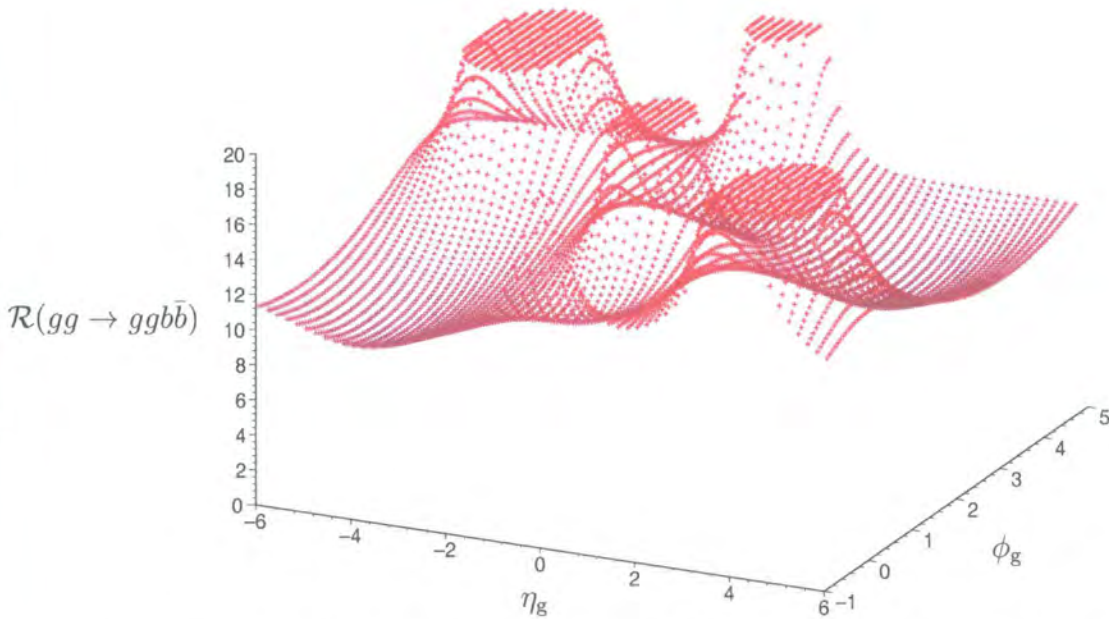


Figure 5.18: Numerical antenna pattern for $gg \rightarrow gg b\bar{b}$ with $|\eta_{\text{jet}}| = 4$ and $k_{Tg} = 1$ GeV.

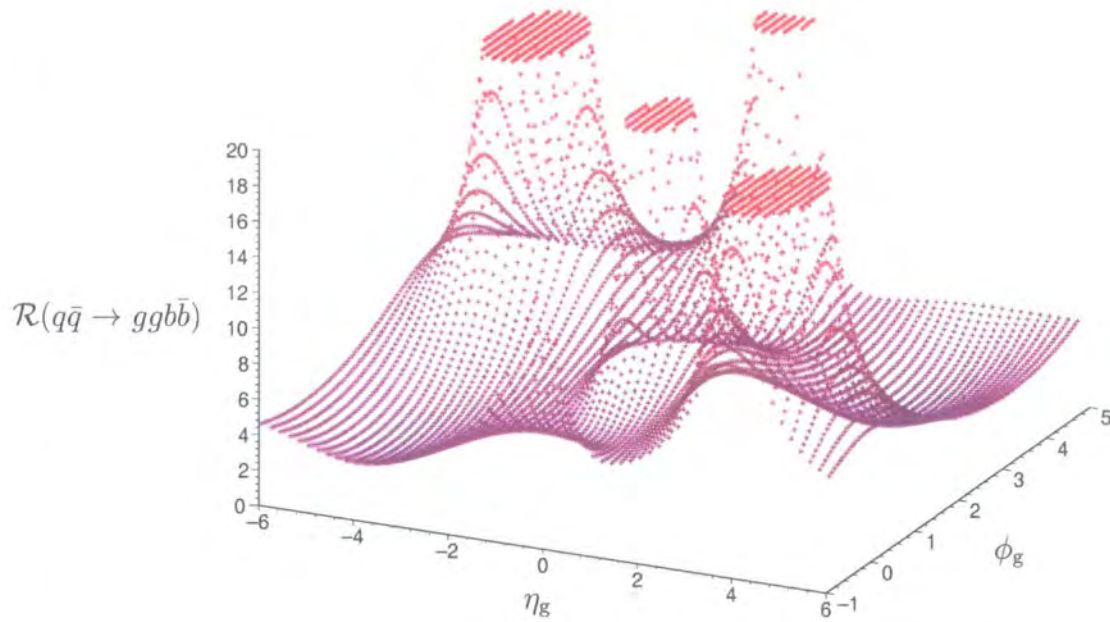


Figure 5.19: Numerical antenna pattern for $q\bar{q} \rightarrow gg\bar{b}\bar{b}$ with $|\eta_{\text{jet}}| = 4$ and $k_{Tg} = 1$ GeV.

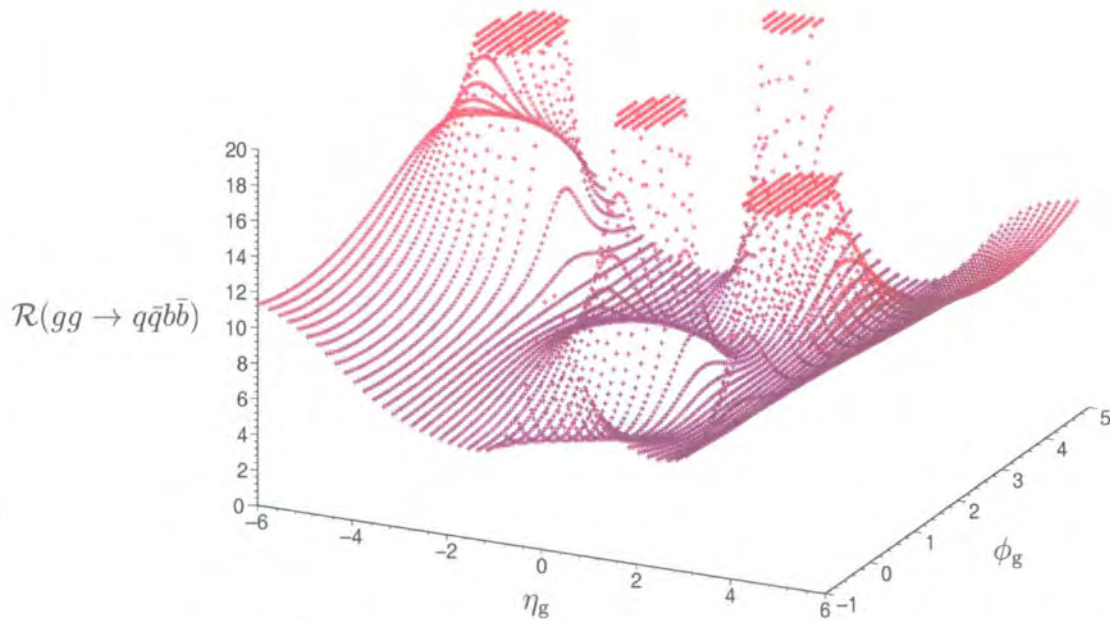


Figure 5.20: Numerical antenna pattern for $gg \rightarrow q\bar{q}\bar{b}\bar{b}$ with $|\eta_{\text{jet}}| = 4$ and $k_{Tg} = 1$ GeV.

from gluon jets is comparatively wider than that from quark jets. The ratio naturally falls to unity at the singularities and over the rest of the plane. Figure 5.22 shows the analytic antenna pattern for $qg \rightarrow qgZ; Z \rightarrow b\bar{b}$ for

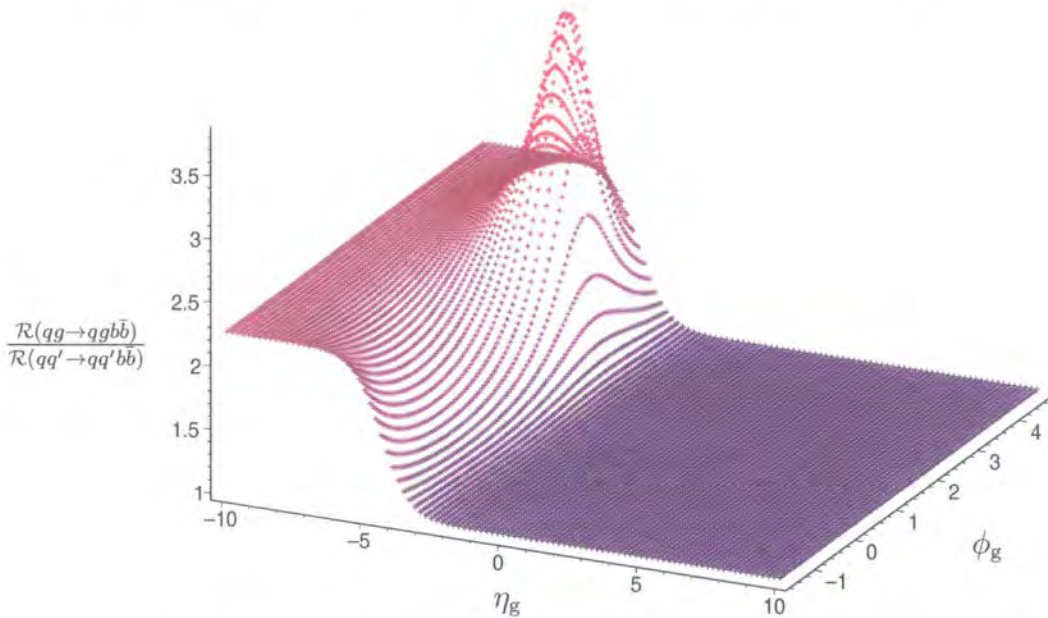


Figure 5.21: Ratio of antennas for $qg \rightarrow qgb\bar{b}$ and $qq' \rightarrow qq'b\bar{b}$.

comparison with the numerical QCD continuum background of Fig. 5.17.

The interesting quantities are of course the *differences* between the signals and backgrounds. Figure 5.23 shows the ratio of numerical $qq' \rightarrow qq'H; H \rightarrow b\bar{b}$ to numerical $qq' \rightarrow qq'b\bar{b}$ antenna patterns, for the same typical kinematic configuration as before, i.e. $|\eta_{\text{jet}}| = 4$ and $k_{Tg} = 1$ GeV. We see that the ratio (i) falls to near zero between the central and forward particles (rapidity gap effect), (ii) is larger than one between the final-state $b\bar{b}$ pair, (iii) is larger than one between the forward jets and the beam (the [13] and [24] connection in the signal), and (iv) approaches unity in the forward/backward directions and at the locations (marked as arrows) of the incoming and outgoing particles. Over the whole (η, ϕ) plot, the ratio varies in size from a minimum of 0.03 to a maximum of 2.3, i.e. a factor of 70. The corresponding ratio of the

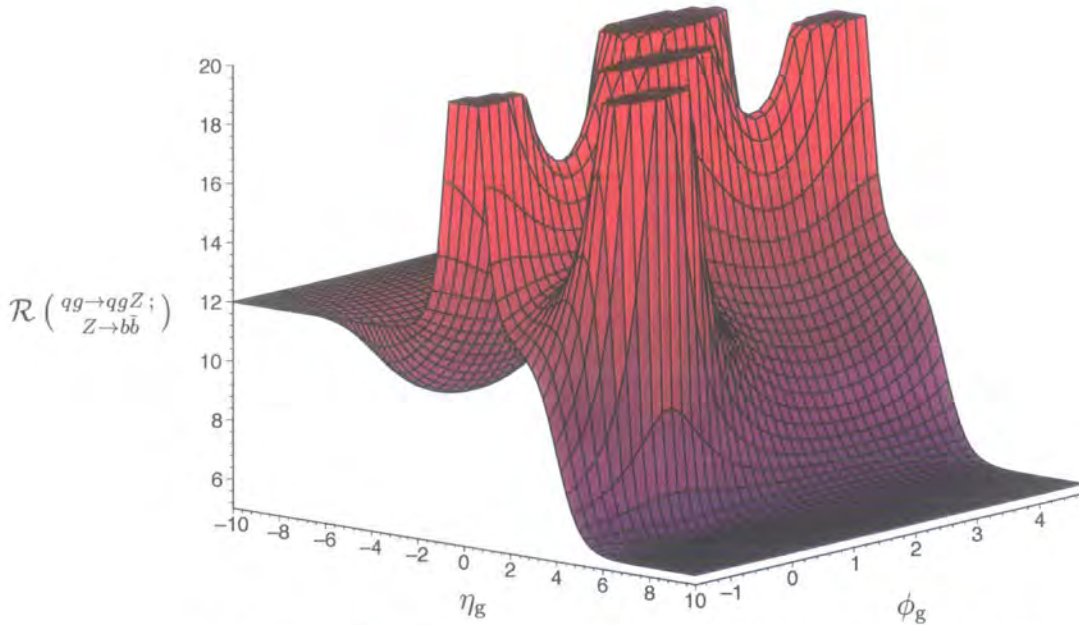


Figure 5.22: Analytic antenna pattern for $qq \rightarrow qqZ; Z \rightarrow b\bar{b}$.

antenna patterns for the electroweak Z production and QCD background is of course very similar.

We next consider (Fig. 5.24) the ratio of the QCD Z -production and background $qq' \rightarrow qq'b\bar{b}$ antenna patterns. There is much less structure here than there was in the corresponding Higgs case, note in particular that the rapidity gap dip between the forward and central particles is absent⁵, and indeed that the ratio is close to one everywhere except near the central b jets. In the Z production case, there is always a colour string connecting the b and the \bar{b} , and this results in the ratio increasing to a maximum of about 1.5 between these two particles. This value has a weak dependence on the rapidities of the forward jets. Figure 5.25 shows the slice through Fig. 5.24 at $\eta_g = 0$ as $|\eta_{\text{jet}}|$ is varied from 1 to 8. The ratio is always one at $\phi_{\text{jet}} = \pi$

⁵Note that by imposing the rapidity gap requirement to isolate the centrally produced system from the proton remnants, we would automatically cut off the colour connection between this system and the forward going partons. As shown in Chapter 4, this allows us to substantially reduce the background contributions, though at the price of a reduction in the overall event rate (due to the notorious survival factors).

and $3\pi/2$, the location of the b and \bar{b} .

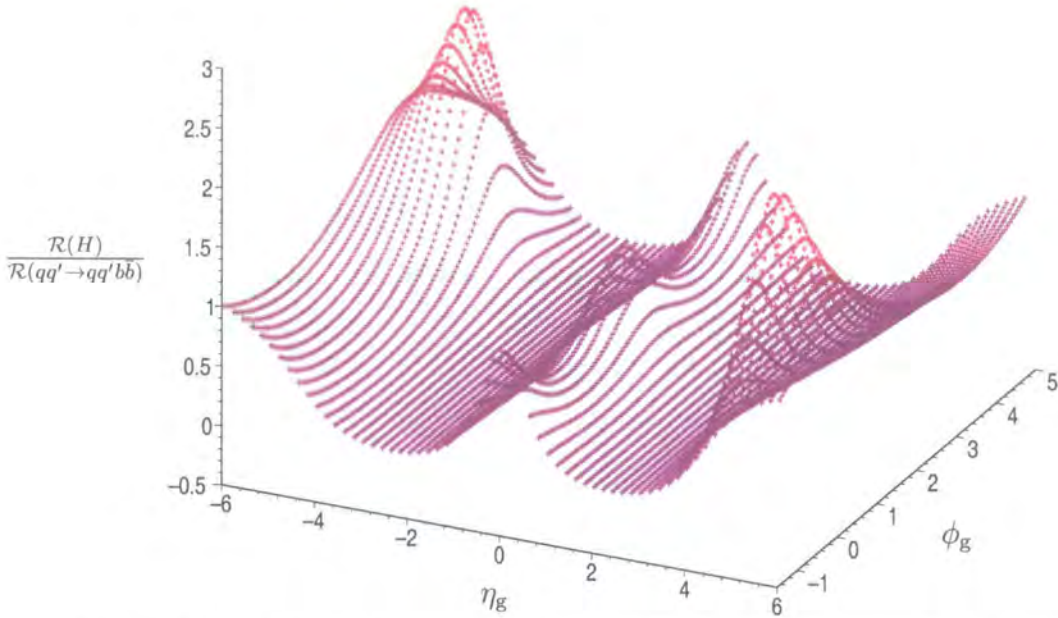


Figure 5.23: Ratio of numerical $qq' \rightarrow qq'H; H \rightarrow b\bar{b}$ to numerical $qq' \rightarrow qq'b\bar{b}$ with $|\eta_{\text{jet}}| = 4$ and $k_{Tg} = 1$ GeV.

5.5 Conclusions

Hadronic radiation patterns can provide a useful additional tool enabling us to improve the separation of Higgs production from the conventional QCD-induced backgrounds. In this Chapter we have focused on the vector boson fusion mechanism of Higgs production in the events with two forward tagging jets. We find that the fairly simple analytical expressions reflecting the coherent structure of QCD radiation off the multi-parton system (antenna pattern) can serve quite successfully as a qualitative guide for the more general numerical calculational technique, which in turn can be applied to a large variety of complicated processes.

The analysis presented here should be regarded as a ‘first look’ at the possibilities offered by hadronic flow patterns in searching for the Higgs in

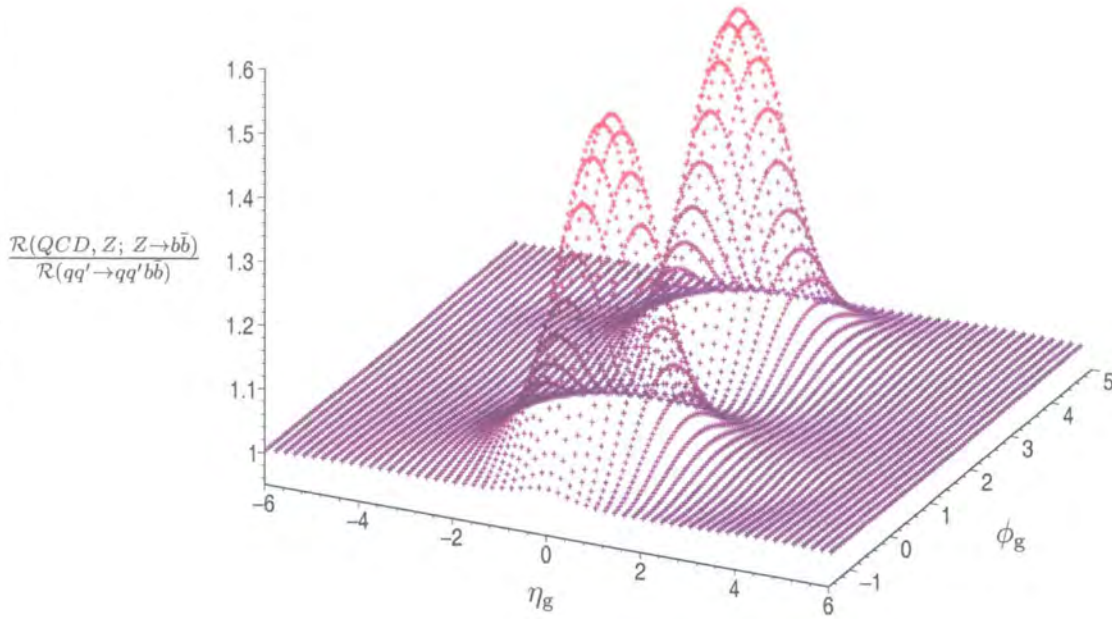


Figure 5.24: Ratio of numerical QCD $qq' \rightarrow qq'Z; Z \rightarrow b\bar{b}$ to numerical $qq' \rightarrow qq'b\bar{b}$ with $|\eta_{jet}| = 4$ and $k_{Tg} = 1$ GeV.

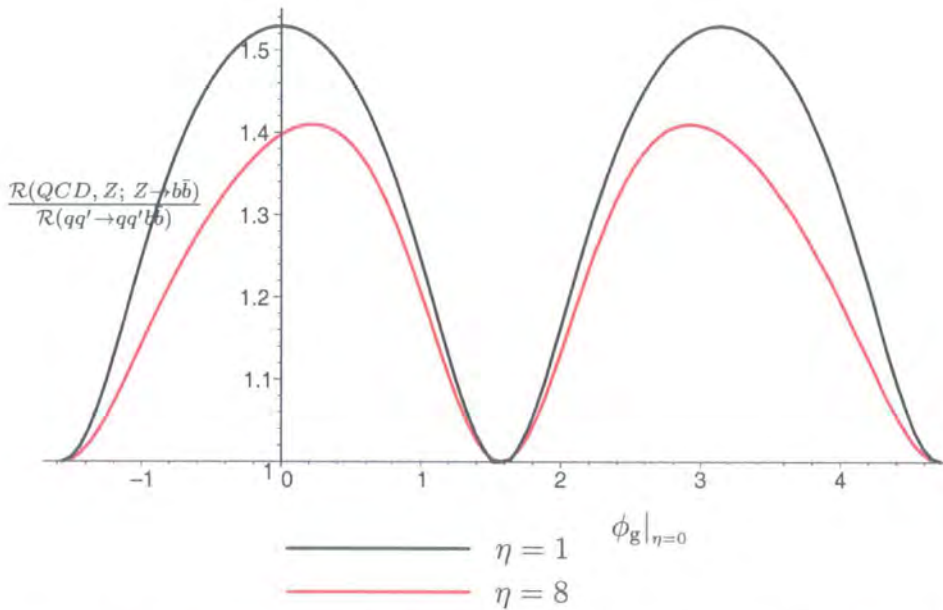


Figure 5.25: Slice in $\eta_g = 0$ of Fig. 5.24 as the rapidity of the forward jets is varied.

vector boson fusion. Of course, ultimately there is no substitute for a detailed Monte Carlo study including detector effects. However the results presented here indicate that the effects can be potentially large, and therefore that more detailed studies are definitely worthwhile.

Chapter 6

Approximating Higgs

Production in Forward Dijet

Events

In Chapter 4 we saw that QCD forward dijet plus central $b\bar{b}$ production obeyed the single effective subprocess approximation. The quark and gluon initiated subprocesses were related to each other simply by comparing the quark-gluon and gluon-gluon couplings. This suggests that, in this limit, the generally complicated cross section factorises into a hard $gg \rightarrow b\bar{b}$ piece accompanied by two splitting functions. This hypothesis is shown in figure 6.1. The intermediary gluons are thus described as being ‘nearly’ on-shell and are indicated with a dashed line through them. In QED this approximation is called the Weizsäcker-Williams equivalent photon approximation [119, 120] (EPA).

In this Chapter we explore the validity of this approach in the gluon fusion Higgs production channel.

The work in this Chapter is, at the time of writing, unfinished and the

results presented here should be viewed as preliminary. The author intends to apply the results here to vector boson fusion Higgs production and all backgrounds subsequently.

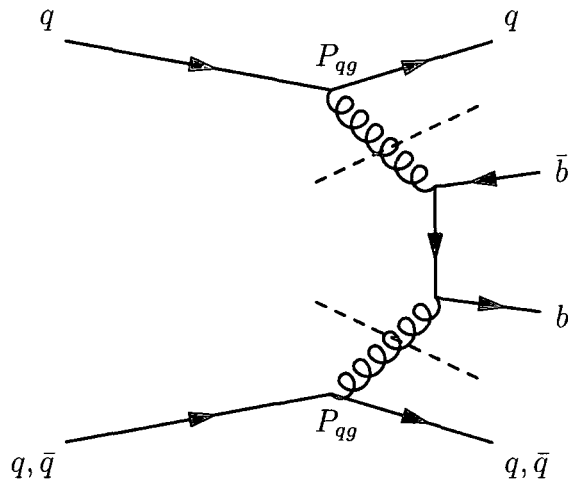


Figure 6.1: ‘Nearly’ on-shell gluon approximation

6.1 Equivalent Photon Approximation

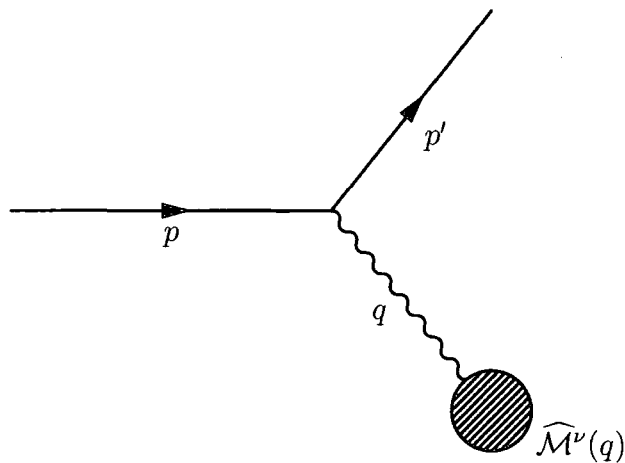


Figure 6.2: High energy electron scattering.

Consider the process of Figure 6.2 where an electron of very high energy scatter from a target. At leading order in α the electron is connected to the

target hard process by one photon propagator. This diagram contains a mass (IR) singularity as discussed in Chapter 1. It appears when the denominator of the propagator vanishes, that is, when the vector boson is almost on-shell. Thus it is natural to consider the electron emitting an almost real photon which then goes on to interact in the hard process. Mathematically, this is equivalent to factorising these two parts of the process.

To do this, we must define a polarisation for the intermediate photon. The electron emission vertex and the hard photon amplitude should then be contracted with physical transverse polarisation vectors for the photon. In Feynman gauge, the numerator of the photon propagator is $g^{\mu\nu}$, we must be careful to check that our intermediate propagator reduces to this. We expand $g^{\mu\nu}$ in terms of massless polarisation vectors as follows. Let $q^\mu \equiv (q^0, \mathbf{q})$ be our hypothetical light-like vector: $q^2 = 0$. Then there are two purely spatial vectors orthogonal to \mathbf{q} . As q is the momentum of a vector boson, these are the two transverse polarisations. To construct an orthogonal basis and be applicable to massive vectors, we include the longitudinal polarisation parallel to \mathbf{q} . A time-like polarisation ϵ completes our basis. We work with two light-like linear combinations of these states, with polarisation vectors parallel to q^μ and $\tilde{q}^\mu \equiv (q^0, -\mathbf{q})$. Thus the two unphysical polarisations (of a massless vector) can be written

$$\epsilon_\mu^+(q) = \left(\frac{q^0}{\sqrt{2}|\mathbf{q}|}, \frac{\mathbf{q}}{\sqrt{2}|\mathbf{q}|} \right); \quad \epsilon_\mu^-(q) = \left(\frac{q^0}{\sqrt{2}|\mathbf{q}|}, -\frac{\mathbf{q}}{\sqrt{2}|\mathbf{q}|} \right). \quad (6.1)$$

These are known as the *forward* and *backward* light-like polarisation vectors. Denote the two transverse polarisations $\epsilon_{i\mu}^T(q)$, for $i = 1, 2$. These four vectors

obey the orthogonality relations

$$\begin{aligned} \epsilon_i^T \cdot \epsilon_j^{*T} &= -\delta_{ij} & \epsilon^+ \cdot \epsilon_i^T &= \epsilon^- \cdot \epsilon_i^T = 0 \\ (\epsilon^+)^2 &= (\epsilon^-)^2 = 0 & \epsilon^+ \cdot \epsilon^- &= 1. \end{aligned} \quad (6.2)$$

They also satisfy the completeness relation

$$g_{\mu\nu} = \epsilon_\mu^- \epsilon_\nu^{+*} + \epsilon_\mu^+ \epsilon_\nu^{-*} - \sum_i \epsilon_{i\mu}^T \epsilon_{i\nu}^{T*}. \quad (6.3)$$

The forward polarisation is proportional to the photon momentum q^μ . When we contract ϵ_μ^+ with the hard scattering amplitude we will obtain zero by the Ward identity. Similarly, the contraction of ϵ_ν^{+*} with the electron emission vertex gives zero. Thus, for the purpose of computing the singular term as the photon momentum goes on-shell, we may replace

$$\frac{-ig_{\mu\nu}}{q^2} \rightarrow \frac{+i}{q^2} \sum_i \epsilon_{i\mu}^T \epsilon_{i\nu}^{T*} \quad (6.4)$$

and evaluate the photon emission and absorption amplitudes with transverse polarisation vectors.

Matrix Element for Electron Splitting

We have now decoupled the photon emission vertex from the rest of the diagram by our replacement of the propagator with a polarisation sum. We

will evaluate this vertex with the following kinematics

$$\begin{aligned}
 p &= (p, 0, 0, p) \\
 q &\approx (zp, p_T, 0, zp) \\
 p' &\approx ((1-z)p, -p_T, 0, (1-z)p)
 \end{aligned} \tag{6.5}$$

where z is the fraction of the energy of the initial state carried by the photon. The final state particles are almost collinear. These vectors satisfy $p^2 = q^2 = p'^2 = 0$, up to $\mathcal{O}(p_T^2)$.

In our process where the final state electron is real, we should have p^2 and p'^2 exactly zero and q^2 slightly off-shell by an amount of order p_T^2 . We will need to know the value of q^2 that appears in the photon propagator. So we modify Eq. (6.5) to satisfy the condition $p'^2 = 0$ up to $\mathcal{O}(p_T^4)$ thus

$$\begin{aligned}
 p' &= \left((1-z)p, -p_T, 0, \left[(1-z)p - \frac{p_T^2}{2(1-z)p} \right] \right) \\
 q &= \left(zp, p_T, 0, \left[zp + \frac{p_T^2}{2(1-z)p} \right] \right).
 \end{aligned} \tag{6.6}$$

Then

$$p'^2 = 0; \quad q^2 = -\frac{p_T^2}{(1-z)}. \tag{6.7}$$

The matrix element of the electron-photon vertex is leading $\mathcal{O}(p_T)$ and therefore, it does not matter whether we chose (6.5) or (6.6). Interestingly, it also does not matter which of the final state particles is real.

Choosing a left handed spinor, the photon emission amplitude is

$$i\mathcal{M} = \bar{u}_L(p')(-ie\gamma^\mu)u_L(p)\epsilon_\mu^{*T}(q). \tag{6.8}$$

Utilising the massless helicity basis:

$$\gamma^\mu = \begin{pmatrix} 0 & \sigma^\mu \\ \bar{\sigma}^\mu & 0 \end{pmatrix}, \quad u_L(p) = \sqrt{2p^0} \begin{pmatrix} \xi(p) \\ 0 \end{pmatrix} \quad (6.9)$$

(6.8) becomes

$$i\mathcal{M} = -ie\sqrt{2(1-z)}p\sqrt{2p}\xi^\dagger(p')\sigma^i\xi(p)\epsilon_i^{*T}(q). \quad (6.10)$$

To $\mathcal{O}(p_T)$, the left-handed spinors are

$$\xi(p) = \begin{pmatrix} 0 \\ 1 \end{pmatrix}, \quad \xi(p') = \begin{pmatrix} p_T/2(1-z)p \\ 1 \end{pmatrix}. \quad (6.11)$$

The polarisation vectors for the photon are

$$\epsilon_i^{*L}(q) = \frac{1}{\sqrt{2}}(1, i, -\frac{p_T}{zp}), \quad \epsilon_i^{*R}(q) = \frac{1}{\sqrt{2}}(1, -i, -\frac{p_T}{zp}). \quad (6.12)$$

When these vectors are contracted with the Pauli matrices, the first two components of the right-handed vector give $(\sigma^1 - i\sigma^3) = 2\sigma^-$, which annihilates $\xi(p)$. The only remaining term comes from the $i = 3$ component, and we find

$$i\mathcal{M}(e_L^- \rightarrow e_L^- \gamma_R) = ie \frac{\sqrt{2(1-z)}}{z} p_T. \quad (6.13)$$

For the left-handed photon polarisation, there is an additional contribution from the first two components of ϵ^{*L} . These add to

$$i\mathcal{M}(e_L^- \rightarrow e_L^- \gamma_L) = ie \frac{\sqrt{2(1-z)}}{z(1-z)} p_T. \quad (6.14)$$

Parity invariance guarantees that these are unchanged if the initial state is right-handed. Thus the averaged, squared matrix element is

$$\frac{1}{2} \sum_{\text{pols.}} |\mathcal{M}|^2 = \frac{2e^2 p_T^2}{z(1-z)} \left[\frac{1 + (1-z)^2}{z} \right]. \quad (6.15)$$

The first term in the brackets comes from a photon with spin parallel to the electron spin; the second term comes from a photon with spin opposite to the electron spin.

The Approximate Scattering Cross Section

Returning to Fig. 6.2, the cross section is

$$\sigma = \frac{1}{2p} \int \frac{d^3 p'}{2\pi^3 p'^0} \int d\hat{\Pi} \left[\frac{1}{2} \sum |\mathcal{M}|^2 \right] \left(\frac{1}{q^2} \right)^2 |\widehat{\mathcal{M}}|^2. \quad (6.16)$$

The integral has a singularity when p' is collinear with the incident electron. To isolate this singularity, substitute for p'^0 and q^2 from Eqs. (6.6) and (6.7), then the p' -integral is

$$d^3 p' = dp'^3 d^2 p'_T = pdz \cdot \pi dp_T^2. \quad (6.17)$$

Now the cross section is

$$\sigma = \int \frac{pdz dp_T^2}{16\pi^2(1-z)} \left[\frac{1}{2} \sum |\mathcal{M}|^2 \right] \frac{(1-z)^2 z}{p_T^4 2zp} \int d\hat{\Pi} |\widehat{\mathcal{M}}|^2 \quad (6.18)$$

$$= \int \frac{pdz dp_T^2}{16\pi^2(1-z)} \left[\frac{1}{2} \sum |\mathcal{M}|^2 \right] \frac{(1-z)^2}{p_T^4} \cdot \hat{\sigma}. \quad (6.19)$$

Replacing for our electron splitting matrix element, Eq. (6.15), one obtains

$$\sigma = \int_0^1 dz \int \frac{dp_T^2}{p_T^2} \frac{\alpha}{2\pi} \left[\frac{1 + (1-z)^2}{z} \right] \cdot \hat{\sigma}. \quad (6.20)$$

The p_T^2 -integral runs from some maximum (of order s) to some minimum (in this specific case m_e - but we shall be more general) which cuts off the singularity such that

$$\sigma = \int_0^1 dz \frac{\alpha}{2\pi} \ln \frac{p_{T\max}^2}{p_{T\min}^2} \left[\frac{1 + (1-z)^2}{z} \right] \cdot \hat{\sigma}. \quad (6.21)$$

This is the Weiszäcker-Williams equivalent photon approximation cross section.

Note that the electron splitting function

$$P_{ee}(z) \equiv \frac{1 + (1-z)^2}{z} \quad (6.22)$$

is the same as the QCD quark splitting function, $P_{qq}(x)$ (Eq. (1.69)) but, of course, without the colour factor.

The method outlined above can be generalised to multiple splittings and to higher orders in the coupling - a topic of current study in QCD.

6.2 Testing an Equivalent Gluon Approximation

In direct analogy to the QED case we now apply these techniques to Higgs production via gluon fusion accompanied by two forward jets. We will work exclusively in the large top mass limit. Our parton level cross section up to

constants is

$$\begin{aligned} \hat{\sigma}(ab \rightarrow a + H + b) = \int dz_1 dz_2 \frac{dp_{T1}^2}{p_{T1}^2} \frac{dp_{T2}^2}{p_{T1}^2} P_{ga}(z_1) P_{gb}(z_2) \\ \times \hat{\sigma}(gg \rightarrow H) \Big|_{\hat{s}=z_1 z_2 \hat{s}} \delta(\hat{s} - m_H^2) \end{aligned} \quad (6.23)$$

where $a, b = q, g$, plus signs indicate that we restrict the jets to be forward in rapidity and the Higgs central, wide hats signify the parton level variables and small hats signify the subprocess variables after parton splitting. $P_{ga}(z_i)$ are the QCD splitting functions of Eq. (1.69). The integration limits are $[0, 1]$ for the z_i and $[p_{T i \min}, p_{T i \max}]$ for the $p_{T i}$. Obviously, this expression should then be integrated over the parton momentum fractions weighted by appropriate parton distribution functions and summed over initial states to produce a hadron level cross section. We will compare this approximation with the exact helicity amplitude expressions for Higgs plus four jets [121, 122]. We will also compare to an analytic high energy limit derived from the exact amplitude [123].

6.2.1 The High Energy Limit

In the kinematics we are considering we have strongly ordered squared dijet masses, i.e. $s_{j_1 j_2} \gg s_{jH} \gg m_H^2$. In this case, the colour decomposed partial amplitudes of [122] factorise into effective vertices connected by a gluon exchanged in the t -channel. Unlike our EGA approximation, the gluon is not constrained to be nearly on-shell. This factorisation in the high energy limit constitutes a stringent check on the amplitudes and is independent of the large top mass limit. Recently this has been used as a check for a loop calculation of Higgs plus two jets with finite top mass [123]. Concentrating

on quark induced production, the amplitude for a particular helicity configuration can be expressed as

$$\begin{aligned}
 & i\mathcal{M}(p_2^-, p_1^+, p_H, p_3^+, p_4^-) \\
 &= 2s[g_s T_{a_1 \bar{a}_2}^c C^{\bar{q};q}(p_2^-; p_1^+)] \frac{1}{t_1} [\delta^{cc'} C^H(q_1, p_H, q_2)] \frac{1}{t_2} [g_s T_{a_3 \bar{a}_4}^{c'}(p_4^-; p_3^+)],
 \end{aligned} \tag{6.24}$$

where $q_1 = -(p_1 + p_2)$, $q_2 = p_3 + p_4$, $t_i \simeq -|q_{iT}|$ with $i = 1, 2$. The effective quark vertices have been calculated at LO and NLO and can be found in [124]. The effective Higgs vertex, while generally of complex structure, reduces in the large top limit to the following expression

$$\lim_{m_t \rightarrow \infty} C^H(q_1, p_H, q_2) = i \frac{A}{2} (|p_{HT}|^2 - |q_{1T}|^2 - |q_{2T}|^2), \tag{6.25}$$

where the effective coupling

$$A \equiv \frac{\alpha_s}{3\pi \sqrt{G_F \sqrt{2}}}. \tag{6.26}$$

Figure 6.3 provides an aid in visualising the amplitude, note this is not a Feynman graph as we use effective vertices. The authors of [123] calculate the spin/colour summed and averaged squared matrix element and obtain

$$|\mathcal{M}^{qq' \rightarrow qq' H}|^2 = 2g_s^4 \frac{s^2}{t_1^2 t_2^2} |C^H(q_1, p_H, q_2)|^2. \tag{6.27}$$

6.2.2 Comparing the Results

Before comparing the exact and approximate cross sections we must address the issue of what limits are appropriate in the $p_{T,i}^2$ -integrals of Eq. (6.23). We

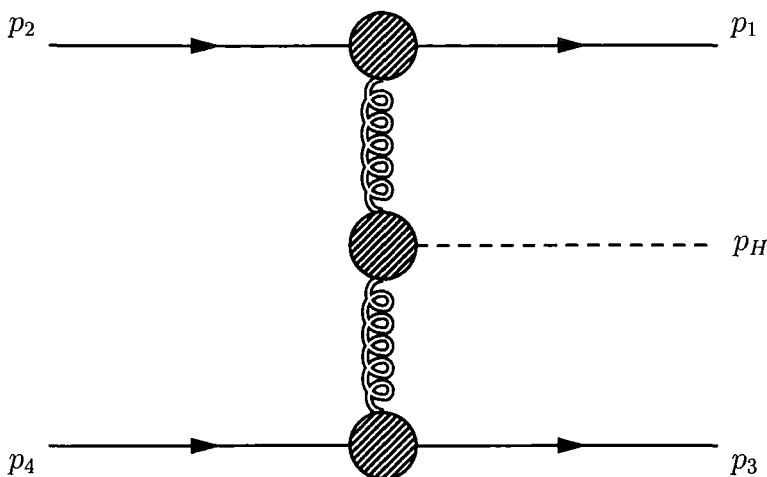


Figure 6.3: Higgs plus two jet production in the high energy limit.

expect the upper limit to be of the order of the scale of the hard scattering process - in our case this is m_H^2 . The lower limit should be the smallest p_T that we can experimentally measure, we expect the approximation to become more valid as this limit is lowered.

Figure 6.4 compares the EGA with the exact cross section for quark induced gluon fusion Higgs production with $m_H = 115$ GeV. The upper limits on the p_T^2 integrations is m_H^2 . The mantissa varies over values of the lower limit on this integration. Data for a number of parton centre of mass energies is shown. When we integrate over parton momentum fractions, our rapidity cuts will select those events where x is very large - typically larger than 0.2. The parton centre of mass energy will thus be in the range of TeV at the LHC. The figure shows that, in this range, a value of $p_{T\min}$ equal to 0.2 GeV reproduces the exact result to within 5%.

Figure 6.5 shows the parton level cross sections as a function of the centre of mass energy with the cuts described previously. As the energy is raised the EGA approximates the exact cross section well, whereas the high energy limit underestimates it. This must be an artifact of the cuts we are using

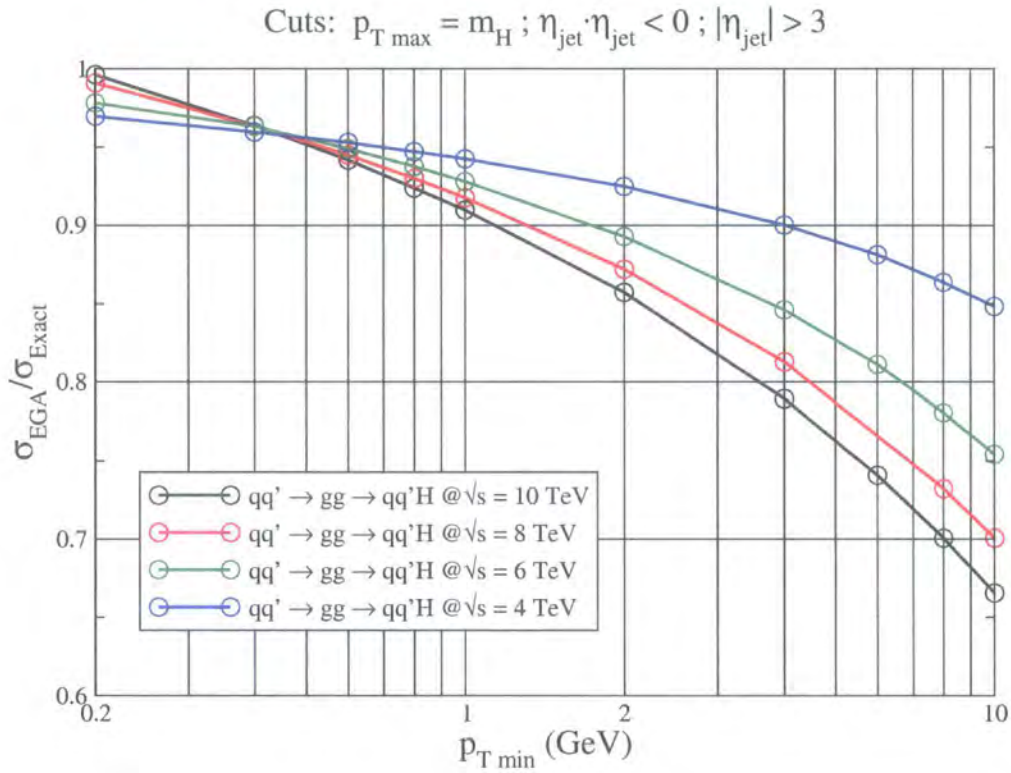


Figure 6.4: Ratio of EGA with exact gluon fusion Higgs production.

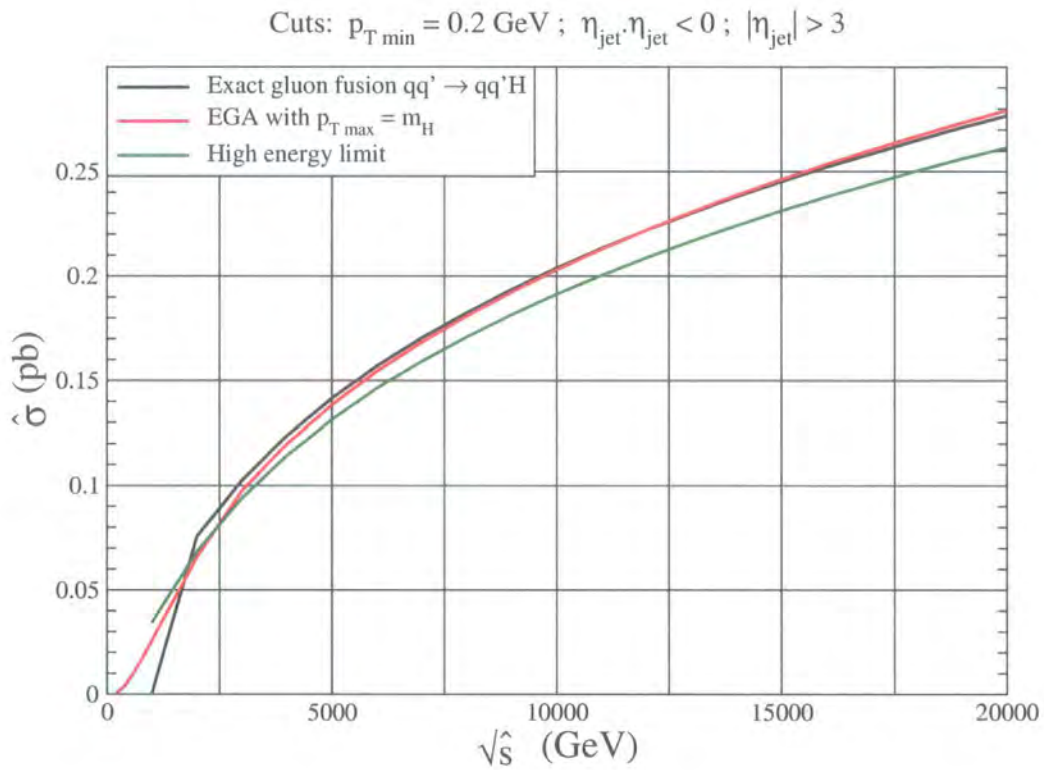


Figure 6.5: Approximate and exact cross sections for gluon fusion Higgs production at parton level.

and merits further investigation. When we integrate these cross sections over the parton distributions we sample the lower regions of this plot where the approximations both underestimate the cross section. This can be seen in Figure 6.6.

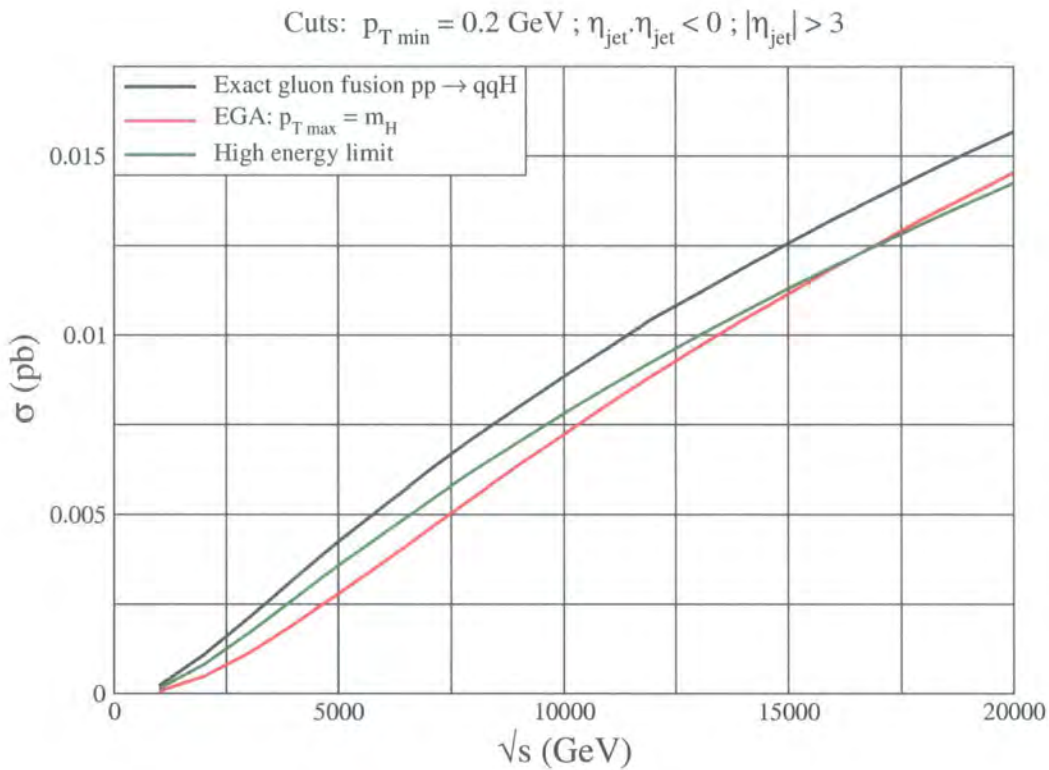


Figure 6.6: Approximate and exact cross sections for gluon fusion Higgs production at hadron level (qq -induced only).

6.3 Extending the Investigation

Unfortunately, due to time constraints, the comparison thus far has only been performed for quark-quark initial states in gluon fusion Higgs production. Implementation through the defining of extra FORTRAN subroutines for

the effective vertices in the cases of quark-gluon and gluon-gluon initiated processes is not trivial. This is due to the colour structure of the $gggH$ and $ggggH$ effective vertices. The author expects to complete these following the production of this thesis. A more direct, alternative method is also in progress. This involves numerically evaluating the analytic partial amplitudes and is close to completion.

The method should be applied to QCD induced forward dijet plus central $b\bar{b}$ and also to vector boson fusion Higgs production. In the QCD case, the method will have a practical spin-off as computational time will be many times less than that involved in numerically integrating the full matrix elements.

Appendix A

Soft Gluon Radiation

Probability

In this Appendix we explicitly calculate the probability that n soft gluons will be emitted from an arbitrary hard scattering. These results are needed in the context of the parton level gap survival probability presented in Chapter 4 and are also touched upon in Chapter 1 where we allude to the fact that IR divergences in QFT cancel between diagrams at all orders.

The derivation is analogous to the case of emitting soft photons in QED and we follow the standard argument set out in [125]. The results were first presented in a paper by Bloch and Nordsieck [126], written before the invention of relativistic perturbation theory. The version of the analysis we explore is originally due to Weinberg [127].

A.1 Summation of Infrared Divergences in QED

In Section 1.5 we saw that an IR divergence originating from soft or collinear gluon at leading order cancelled with an IR divergence arising from a virtual contribution at next-to-leading order. The purpose of this section is to generalise this and, in doing so, derive an expression for the mean number of emitted soft photons. Thus, we consider diagrams in which an arbitrary hard process, possibly involving the emission of hard and soft photons, is modified by the addition of soft real and virtual photons on the electron legs. This is illustrated in Fig. A.1. We will add up the contributions of all such diagrams,

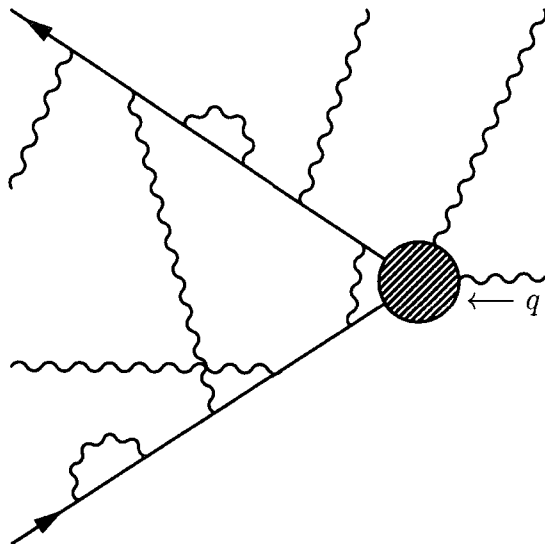


Figure A.1: Soft real and virtual photons (left) emitted from an arbitrary hard process (right).

being careful about the combinatorics. We attach n photons to the outgoing electron line, Fig. A.2, with momenta $k_1 \dots k_n$. For the moment we do not care whether these are external photons, virtual photons connected to each other, or virtual photons connected to vertices on the incoming electron line.

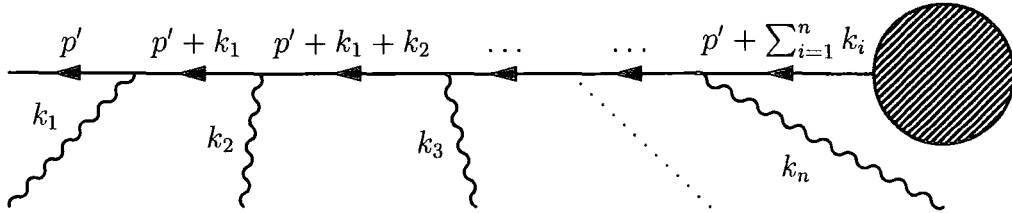


Figure A.2: The outgoing electron line of Fig. A.1.

The Dirac structure of this is

$$\begin{aligned} \bar{u}(p')(-ie\gamma^{\mu_1})\frac{i(\not{p}' + \not{k}_1 + m)}{2p' \cdot k_1}(-ie\gamma^{\mu_2})\frac{i(\not{p}' + \not{k}_1 + \not{k}_2 + m)}{2p' \cdot (k_1 + k_2) + \mathcal{O}(k^2)} \\ \dots (-ie\gamma^{\mu_n})\frac{i(\not{p}' + \not{k}_1 + \dots + \not{k}_n + m)}{2p' \cdot (k_1 + \dots + k_n) + \mathcal{O}(k^2)}(i\mathcal{M}_{\text{hard}}). \end{aligned} \quad (\text{A.1})$$

Using the soft limit where we drop the \not{k}_i terms in the numerators and use the Dirac equation as in Eq. (5.2) we obtain

$$\bar{u}(p') \left(e \frac{p'^{\mu_1}}{p' \cdot k_1} \right) \left(e \frac{p'^{\mu_2}}{p' \cdot (k_1 + k_2)} \right) \dots \left(e \frac{p'^{\mu_n}}{p' \cdot (k_1 + \dots + k_n)} \right) \dots \quad (\text{A.2})$$

We must now sum over all possible orderings of the momenta $k_1 \dots k_n$ (this procedure will overcount when two of the photons are attached together to form a single virtual photon. We deal with this later.) There are $n!$ different diagrams to sum corresponding to the $n!$ permutations of the n photon momenta. Let π denote one such permutation, so that $\pi(i)$ is the number between 1 and n that i is taken to¹. Armed with this notation, we

¹For example, if π denotes the permutation that takes $1 \rightarrow 3$, $2 \rightarrow 1$ and $3 \rightarrow 2$, then $\pi(1) = 3$, $\pi(2) = 1$ and $\pi(3) = 2$.

can perform the sum over permutations by means of the following identity:

$$\sum_{\substack{\text{all permuta-} \\ \text{tions } \pi}} \frac{1}{p \cdot k_{\pi(1)}} \frac{1}{p \cdot (k_{\pi(1)} + k_{\pi(2)})} \cdots \frac{1}{p \cdot (k_{\pi(1)} + k_{\pi(2)} + k_{\pi(n)})} \\ = \frac{1}{p \cdot k_1} \frac{1}{p \cdot k_2} \cdots \frac{1}{p \cdot k_n}. \quad (\text{A.3})$$

This formula can be proved by induction on n . For $n = 2$ we have

$$\sum_{\pi} \frac{1}{p \cdot k_{\pi(1)}} \frac{1}{p \cdot (k_{\pi(1)} + k_{\pi(2)})} = \frac{1}{p \cdot k_1} \frac{1}{p \cdot k_2} + \frac{1}{p \cdot k_2} \frac{1}{p \cdot (k_2 + k_1)} \\ = \frac{1}{p \cdot k_1} \frac{1}{p \cdot k_2}. \quad (\text{A.4})$$

For the induction step, notice that the last factor on the left hand side of Eq. (A.3) is the same for every permutation π . Putting this factor outside the sum, the left hand side becomes

$$\text{LHS} = \frac{1}{p \cdot \sum k} \sum_{\pi} \frac{1}{p \cdot k_{\pi(1)}} \frac{1}{p \cdot (k_{\pi(1)} + k_{\pi(2)})} \cdots \frac{1}{p \cdot (k_{\pi(1)} + \cdots + k_{\pi(n-1)})}. \quad (\text{A.5})$$

For any given π , the quantity being summed is independent of $k_{\pi(n)}$. Letting $i = \pi(n)$, we can now write

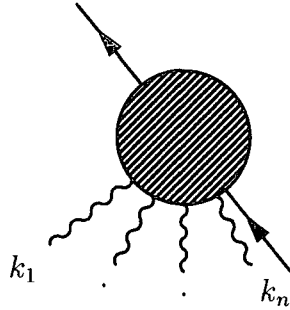
$$\sum_{\pi} = \sum_{i=1}^n \sum_{\pi'(i)}, \quad (\text{A.6})$$

where $\pi'(i)$ is the set of all permutations on the remaining $n - 1$ integers.

Assuming by induction that Eq. (A.3) is true for $n - 1$, we have

$$\text{LHS} = \frac{1}{p \cdot \sum k} \sum_{i=1}^n \frac{1}{p \cdot k_1} \frac{1}{p \cdot k_2} \cdots \frac{1}{p \cdot k_{i-1}} \frac{1}{p \cdot k_{i+1}} \cdots \frac{1}{p \cdot k_n}. \quad (\text{A.7})$$

If we now multiply and divide each term in this sum by $p \cdot k_i$, we easily obtain our desired result, Eq. (A.3). Applying this to Eq. (A.2), we find



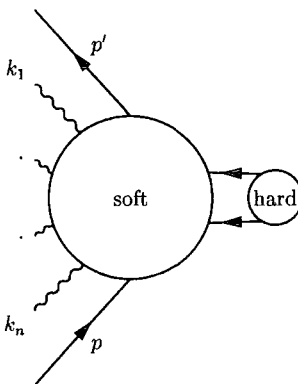
$$= \bar{u}(p') \left(e \frac{p'^{\mu_1}}{p' \cdot k_1} \right) \left(e \frac{p'^{\mu_2}}{p' \cdot k_2} \right) \cdots \left(e \frac{p'^{\mu_n}}{p' \cdot k_n} \right), \quad (\text{A.8})$$

where the blob denotes a sum over all possible orders of inserting the n photon lines.

A similar set of manipulations simplifies the sum over soft photons on the initial electron line. There, however, the propagator momenta are $p - k_1$, $p - k_1 - k_2$ and so on. We therefore get an extra minus sign in the factor for each photon, since $(p - \sum k)^2 - m^2 \simeq -2p \cdot \sum k$.

Now consider diagrams containing a total of n soft photons, connected in any possible order to the initial or final electron lines. The sum over all such

diagrams can be written



$$\begin{aligned}
 &= \bar{u}(p') i \mathcal{M}_{\text{hard}} u(p) \times e \left(\frac{p'^{\mu_1}}{p' \cdot k_1} - \frac{p'^{\mu_1}}{p \cdot k_1} \right) \dots \\
 &\dots \times e \left(\frac{p'^{\mu_n}}{p' \cdot k_n} - \frac{p'^{\mu_n}}{p \cdot k_n} \right).
 \end{aligned}
 \tag{A.9}$$

By multiplying out all the factors, you can see that we get the correct term for each possible way of dividing the n photons between the two lines.

Next we must decide which photons are real and which are virtual.

We can make a virtual photon by picking two photon momenta k_i and k_j , setting $k_j = -k_i \equiv k$, multiplying by the photon propagator, and integrating over k . For each virtual photon we then obtain the expression

$$\frac{e^2}{2} \int \frac{d^4 k}{(2\pi)^4} \frac{-i}{k^2} \left(\frac{p'}{p' \cdot k} - \frac{p}{p \cdot k} \right) \cdot \left(\frac{p'}{-p' \cdot k} - \frac{p}{-p \cdot k} \right) \equiv \mathbf{X}. \tag{A.10}$$

The factor of $1/2$ is required because our procedure has counted each Feynman diagram twice: interchanging k_i and k_j gives back the same diagram. It is possible to evaluate this expression by careful contour integration. Weinberg does this and obtains

$$\mathbf{X} = -\frac{\alpha}{2\pi} f_{\text{IR}}(q^2) \ln(-q^2/\mu^2) \tag{A.11}$$

with

$$f_{\text{IR}}(q^2) = \int_0^1 \left(\frac{m^2 - q^2/2}{m^2 - q^2\xi(1-\xi)} \right) d\xi - 1. \quad (\text{A.12})$$

If there are m virtual photons we get m factors like Eq. (A.11), and also an additional symmetry factor of $1/m!$ since interchanging virtual photons with each other does not change the diagram. We can then sum over m to obtain the complete correction due to the presence of arbitrarily many soft virtual photons:

$$\text{soft} \text{---} \text{hard} \text{---} = \text{hard} \text{---} \times \sum_{m=0}^{\infty} \frac{\mathbf{X}^m}{m!} = \bar{u}(p')(i\mathcal{M}_{\text{hard}})u(p) \exp(\mathbf{X}). \quad (\text{A.13})$$

If, in addition to the m virtual photons, we also emit a real photon, we must multiply by its polarisation vector, sum over polarisations, and integrate the squared matrix element over the photon's phase space. This gives an additional factor

$$\int \frac{d^3k}{(2\pi)^3} \frac{1}{2k} e^2 (-g_{\mu\nu}) \left(\frac{p'^\mu}{p' \cdot k} - \frac{p^\mu}{p \cdot k} \right) \left(\frac{p'^\nu}{p' \cdot k} - \frac{p^\nu}{p \cdot k} \right) \equiv \mathbf{Y} \quad (\text{A.14})$$

in the cross section. Assuming that the energy of the photon is greater than μ and less than E_l (the detector threshold), this expression is simply

$$\mathbf{Y} = \frac{\alpha}{\pi} f_{\text{IR}}(q^2) \ln \left(\frac{E_l^2}{\mu^2} \right). \quad (\text{A.15})$$

If n real photons are emitted we get n such factors, and also a symmetry

factor of $1/n!$ since there are n identical bosons in the final state. The cross section for emission of any number of soft photons is therefore

$$\sum_{n=0}^{\infty} \frac{d\sigma}{d\Omega}(\mathbf{p} \rightarrow \mathbf{p}' + n\gamma) = \frac{d\sigma}{d\Omega}(\mathbf{p} \rightarrow \mathbf{p}') \times \sum_{n=0}^{\infty} \frac{1}{n!} \mathbf{Y}^n = \frac{d\sigma}{d\Omega}(\mathbf{p} \rightarrow \mathbf{p}') \cdot \exp(\mathbf{Y}). \quad (\text{A.16})$$

Combining our results for virtual and real photons gives our final result for the measured cross section, to all orders in α , for the process $\mathbf{p} \rightarrow \mathbf{p}' +$ (any number of photons with $k < E_l$):

$$\begin{aligned} \left(\frac{d\sigma}{d\Omega}\right)_{\text{meas.}} &= \left(\frac{d\sigma}{d\Omega}\right)_0 \times \exp(2\mathbf{X}) \times \exp(\mathbf{Y}) \\ &= \left(\frac{d\sigma}{d\Omega}\right)_0 \times \exp\left[-\frac{\alpha}{\pi} f_{\text{IR}}(q^2) \ln\left(\frac{-q^2}{\mu^2}\right)\right] \times \exp\left[-\frac{\alpha}{\pi} f_{\text{IR}}(q^2) \ln\left(\frac{E_l^2}{\mu^2}\right)\right] \\ &= \left(\frac{d\sigma}{d\Omega}\right)_0 \times \exp\left[-\frac{\alpha}{\pi} f_{\text{IR}}(q^2) \ln\left(\frac{-q^2}{E_l^2}\right)\right]. \end{aligned} \quad (\text{A.17})$$

The correction factor depends on the detector sensitivity E_l , but is independent of the infrared cutoff μ . In the limit $-q^2 \gg m^2$, our result becomes

$$\left(\frac{d\sigma}{d\Omega}\right)_{\text{meas.}} = \left(\frac{d\sigma}{d\Omega}\right)_0 \times \left| \exp\left[-\frac{\alpha}{2\pi} \ln\left(\frac{-q^2}{m^2}\right) \ln\left(\frac{-q^2}{E_l^2}\right)\right] \right|^2. \quad (\text{A.18})$$

In this limit, the probability of scattering without emitting a hard photon decreases faster than any power of q^2 . The exponential correction factor, containing the Sudakov double logarithm, is known as the *Sudakov form factor*.

Now let us apply all this to the probability, in the same approximation, that some hard scattering process is accompanied by the production of n soft photons, all with energies between E_- and E_+ . The phase space integral for these photons gives $\ln(E_+/E_-)$ instead of $\ln(E_l/\mu)$. If we assign photons with energy greater than E_+ to the “hard” part of the process, we find that

the cross section is given by Eq. (A.17), times the additional factor

$$\begin{aligned} \text{Prob}(n\gamma \text{ with } E_- < E < E_+) &= \frac{1}{n!} \left[\frac{\alpha}{\pi} f_{\text{IR}}(q^2) \ln \left(\frac{E_+^2}{E_-^2} \right) \right]^n \\ &\times \exp \left[-\frac{\alpha}{\pi} f_{\text{IR}}(q^2) \ln \left(\frac{E_+^2}{E_-^2} \right) \right]. \end{aligned} \quad (\text{A.19})$$

This expression has the form of a Poisson distribution,

$$P(n) = \frac{1}{n!} \lambda^n e^{-\lambda} \quad (\text{A.20})$$

with

$$\lambda = \langle n \rangle = \frac{\alpha}{\pi} \ln \left(\frac{E_+^2}{E_-^2} \right) f_{\text{IR}}(q^2). \quad (\text{A.21})$$

A.2 The QCD Result

Equation (A.21) is interpreted as the number of radiated photons from an arbitrary process. It is equivalent to Equation (4.37). The factor of $\ln(\frac{E_+^2}{E_-^2})$, being between the extreme hardest and softest energies of the emitted photons is interpreted as $\ln(\frac{p_i^2}{Q_T^2})$. The factor $f_{\text{IR}}(q^2)$ reduces to $\ln(-q_i^2/t_i^2) = \Delta\eta_i$ in the massless electron limit. The exact result is then recovered by calculating the colour factor for gluon emission from a gluon, which is N_c .

Bibliography

- [1] M. Gell-Mann, Phys. Lett. **8**, 214 (1964).
- [2] G. Zweig, CERN-TH-412.
- [3] M. Gell-Mann, Acta Phys. Austriaca Suppl. **9**, 733 (1974).
- [4] PLUTO, J. Burmester *et al.*, Phys. Lett. **B66**, 395 (1977).
- [5] DASP, R. Brandelik *et al.*, Phys. Lett. **B76**, 361 (1978).
- [6] T. D. Lee and M. Nauenberg, Phys. Rev. **133**, B1549 (1964).
- [7] T. Kinoshita, J. Math. Phys. **3**, 650 (1962).
- [8] G. Sterman and S. Weinberg, Phys. Rev. Lett. **39**, 1436 (1977).
- [9] R. K. Ellis, W. J. Stirling, and B. R. Webber, Cambridge Monogr. Part. Phys. Nucl. Phys. Cosmol. **8**, 1 (1996).
- [10] G. Altarelli and G. Parisi, Nucl. Phys. **B126**, 298 (1977).
- [11] V. N. Gribov and L. N. Lipatov, Yad. Fiz. **15**, 781 (1972).
- [12] Y. L. Dokshitzer, Sov. Phys. JETP **46**, 641 (1977).
- [13] W. Furmanski and R. Petronzio, Phys. Lett. **B97**, 437 (1980).

- [14] G. Curci, W. Furmanski, and R. Petronzio, Nucl. Phys. **B175**, 27 (1980).
- [15] S. L. Glashow, Nucl. Phys. **22**, 579 (1961).
- [16] J. Goldstone, A. Salam, and S. Weinberg, Phys. Rev. **127**, 965 (1962).
- [17] S. Weinberg, Phys. Rev. Lett. **19**, 1264 (1967).
- [18] UA1, G. Arnison *et al.*, Phys. Lett. **B126**, 398 (1983).
- [19] UA2, P. Bagnaia *et al.*, Phys. Lett. **B129**, 130 (1983).
- [20] C. Quigg, Front. Phys. **56**, 1 (1983).
- [21] P. W. Higgs, Phys. Lett. **12**, 132 (1964).
- [22] F. Englert and R. Brout, Phys. Rev. Lett. **13**, 321 (1964).
- [23] LEP, Phys. Lett. **B276**, 247 (1992).
- [24] L. E. W. Group, <http://lepewwg.cern.ch/LEPEWWG/Welcome.html>.
- [25] LEP Higgs Working Group for Higgs Boson Searches, Phys. Lett. **B565**, 61 (2003), hep-ex/0306033.
- [26] ALEPH, R. Barate *et al.*, Phys. Lett. **B495**, 1 (2000), hep-ex/0011045.
- [27] DELPHI, P. Abreu *et al.*, Phys. Lett. **B499**, 23 (2001), hep-ex/0102036.
- [28] A. Djouadi, J. Kalinowski, and M. Spira, Comput. Phys. Commun. **108**, 56 (1998), hep-ph/9704448.
- [29] H. M. Georgi, S. L. Glashow, M. E. Machacek, and D. V. Nanopoulos, Phys. Rev. Lett. **40**, 692 (1978).

- [30] S. Dawson, Nucl. Phys. **B359**, 283 (1991).
- [31] A. Djouadi, M. Spira, and P. M. Zerwas, Phys. Lett. **B264**, 440 (1991).
- [32] R. V. Harlander, Phys. Lett. **B492**, 74 (2000), hep-ph/0007289.
- [33] C. Anastasiou and K. Melnikov, Nucl. Phys. **B646**, 220 (2002), hep-ph/0207004.
- [34] Z. Bern, L. Dixon, and C. Schmidt, Phys. Rev. **D66**, 074018 (2002), hep-ph/0206194.
- [35] CMS, Y. Musienko, Nucl. Instrum. Meth. **A494**, 308 (2002).
- [36] A. Kovalyov, W. J. Stirling, and P. H. Williams, Particle Physics and Astronomy International Undergraduate Summer School Project, July 2003.
- [37] A. D. Martin, R. G. Roberts, W. J. Stirling, and R. S. Thorne, Eur. Phys. J. **C23**, 73 (2002), hep-ph/0110215.
- [38] A. D. Martin, R. G. Roberts, W. J. Stirling, and R. S. Thorne, Eur. Phys. J. **C28**, 455 (2003), hep-ph/0211080.
- [39] R. N. Cahn and S. Dawson, Phys. Lett. **B136**, 196 (1984).
- [40] T. Han, G. Valencia, and S. Willenbrock, Phys. Rev. Lett. **69**, 3274 (1992), hep-ph/9206246.
- [41] S. L. Glashow, D. V. Nanopoulos, and A. Yildiz, Phys. Rev. **D18**, 1724 (1978).
- [42] J. M. Campbell and R. K. Ellis, Phys. Rev. **D62**, 114012 (2000), hep-ph/0006304.

- [43] Z. Kunszt, Nucl. Phys. **B247**, 339 (1984).
- [44] L. Reina, S. Dawson, and D. Wackerth, Phys. Rev. **D65**, 053017 (2002), hep-ph/0109066.
- [45] S. Dawson, L. H. Orr, L. Reina, and D. Wackerth, Phys. Rev. **D67**, 071503 (2003), hep-ph/0211438.
- [46] W. Beenakker *et al.*, Phys. Rev. Lett. **87**, 201805 (2001), hep-ph/0107081.
- [47] W. Beenakker *et al.*, Nucl. Phys. **B653**, 151 (2003), hep-ph/0211352.
- [48] V. A. Khoze, Private Correspondence.
- [49] V. S. Fadin, V. A. Khoze, and T. Sjostrand, Z. Phys. **C48**, 613 (1990).
- [50] CDF, J. Kroll and B. Winer, Summary Note: CDF 6353.
- [51] CERN-LHCC-99-15.
- [52] V. A. Khoze, A. D. Martin, and M. G. Ryskin, Eur. Phys. J. **C26**, 229 (2002), hep-ph/0207313.
- [53] CDF, T. Affolder *et al.*, Phys. Rev. Lett. **84**, 5043 (2000).
- [54] M. Boonekamp, R. Peschanski, and C. Royon, Phys. Rev. Lett. **87**, 251806 (2001), hep-ph/0107113.
- [55] B. Cox, J. Forshaw, and B. Heinemann, Phys. Lett. **B540**, 263 (2002), hep-ph/0110173.
- [56] V. A. Khoze, A. D. Martin, and M. G. Ryskin, Eur. Phys. J. **C24**, 459 (2002), hep-ph/0201301.

- [57] R. Enberg, G. Ingelman, A. Kissavos, and N. Timneanu, Phys. Rev. Lett. **89**, 081801 (2002), hep-ph/0203267.
- [58] T. Sjostrand *et al.*, Comput. Phys. Commun. **135**, 238 (2001), hep-ph/0010017.
- [59] J. D. Bjorken, Int. J. Mod. Phys. **A7**, 4189 (1992).
- [60] V. A. Khoze, A. D. Martin, and M. G. Ryskin, Eur. Phys. J. **C18**, 167 (2000), hep-ph/0007359.
- [61] A. B. Kaidalov, V. A. Khoze, A. D. Martin, and M. G. Ryskin, Eur. Phys. J. **C21**, 521 (2001), hep-ph/0105145.
- [62] R. Enberg, G. Ingelman, and N. Timneanu, J. Phys. **G26**, 712 (2000), hep-ph/0001016.
- [63] A. Bialas, Acta Phys. Polon. **B33**, 2635 (2002), hep-ph/0205059.
- [64] V. A. Khoze, A. D. Martin, and M. G. Ryskin, Eur. Phys. J. **C23**, 311 (2002), hep-ph/0111078.
- [65] V. A. Khoze, A. D. Martin, and M. G. Ryskin, Eur. Phys. J. **C21**, 99 (2001), hep-ph/0104230.
- [66] S. Heinemeyer, W. Hollik, and G. Weiglein, Eur. Phys. J. **C9**, 343 (1999), hep-ph/9812472.
- [67] F. A. Berends, R. Kleiss, P. De Causmaecker, R. Gastmans, and T. T. Wu, Phys. Lett. **B103**, 124 (1981).
- [68] F. A. Berends *et al.*, Nucl. Phys. **B206**, 61 (1982).
- [69] R. Kleiss and W. J. Stirling, Nucl. Phys. **B262**, 235 (1985).

- [70] L. J. Dixon, (1996), hep-ph/9601359.
- [71] H. Murayama, I. Watanabe, and K. Hagiwara, KEK-91-11.
- [72] T. Stelzer and W. F. Long, *Comput. Phys. Commun.* **81**, 357 (1994), hep-ph/9401258.
- [73] F. Maltoni and T. Stelzer, *JHEP* **02**, 027 (2003), hep-ph/0208156.
- [74] W. Press, S. Teukolsky, W. Vetterling, and B. Flannery, *Numerical Recipes in FORTRAN*, Second ed. (Cambridge University Press, 1992).
- [75] F. James, *Rept. Prog. Phys.* **43**, 1145 (1980).
- [76] G. P. Lepage, CLNS-80/447.
- [77] G. Marsaglia, *Linear Algebra and Its Applications* **67**, 147 (1985).
- [78] H. Chehime and D. Zeppenfeld, *Phys. Rev.* **D47**, 3898 (1993).
- [79] D. Rainwater, R. Szalapski, and D. Zeppenfeld, *Phys. Rev.* **D54**, 6680 (1996), hep-ph/9605444.
- [80] A. D. Martin, R. G. Roberts, W. J. Stirling, and R. S. Thorne, *Eur. Phys. J.* **C4**, 463 (1998), hep-ph/9803445.
- [81] CERN-LHCC-94-38.
- [82] A. De Roeck, V. A. Khoze, A. D. Martin, R. Orava, and M. G. Ryskin, *Eur. Phys. J.* **C25**, 391 (2002), hep-ph/0207042.
- [83] B. L. Combridge and C. J. Maxwell, *Nucl. Phys.* **B239**, 429 (1984).
- [84] V. A. Khoze, A. D. Martin, and M. G. Ryskin, *Phys. Lett.* **B401**, 330 (1997), hep-ph/9701419.

- [85] V. A. Khoze, A. D. Martin, and M. G. Ryskin, *Eur. Phys. J.* **C14**, 525 (2000), hep-ph/0002072.
- [86] A. D. Martin, M. G. Ryskin, and V. A. Khoze, *Phys. Rev.* **D56**, 5867 (1997), hep-ph/9705258.
- [87] L. N. Lipatov, *Sov. Phys. JETP* **63**, 904 (1986).
- [88] J. R. Forshaw and M. G. Ryskin, *Z. Phys.* **C68**, 137 (1995), hep-ph/9501376.
- [89] V. G. Gorshkov, V. N. Gribov, L. N. Lipatov, and G. V. Frolov, *Sov. J. Nucl. Phys.* **6**, 95 (1968).
- [90] R. Kirschner and L. N. Lipatov, *Nucl. Phys.* **B213**, 122 (1983).
- [91] A. DeRoeck, Private Correspondence.
- [92] Y. L. Dokshitzer, V. A. Khoze, and T. Sjostrand, *Phys. Lett.* **B274**, 116 (1992).
- [93] D. Rainwater and D. Zeppenfeld, *Phys. Rev.* **D60**, 113004 (1999), hep-ph/9906218.
- [94] V. D. Barger, K.-m. Cheung, T. Han, and D. Zeppenfeld, *Phys. Rev.* **D44**, 2701 (1991).
- [95] J. M. Butterworth, B. E. Cox, and J. R. Forshaw, *Phys. Rev.* **D65**, 096014 (2002), hep-ph/0201098.
- [96] D. Zeppenfeld, R. Kinnunen, A. Nikitenko, and E. Richter-Was, *Phys. Rev.* **D62**, 013009 (2000), hep-ph/0002036.

- [97] N. Kauer, T. Plehn, D. Rainwater, and D. Zeppenfeld, *Phys. Lett.* **B503**, 113 (2001), hep-ph/0012351.
- [98] Y. L. Dokshitzer, S. I. Troian, and V. A. Khoze, *Sov. J. Nucl. Phys.* **46**, 712 (1987).
- [99] Y. L. Dokshitzer, V. A. Khoze, S. I. Troian, and A. H. Mueller, *Rev. Mod. Phys.* **60**, 373 (1988).
- [100] V. A. Khoze and W. Ochs, *Int. J. Mod. Phys.* **A12**, 2949 (1997), hep-ph/9701421.
- [101] V. A. Khoze, W. Ochs, and J. Wosiek, (2000), hep-ph/0009298.
- [102] J. R. Andersen *et al.*, *J. Phys.* **G28**, 2509 (2002), hep-ph/0205127.
- [103] Y. L. Dokshitzer, V. A. Khoze, A. H. Mueller, and S. I. Troian, Gif-sur-Yvette, France: Ed. Frontieres (1991) 274 p. (Basics of Perturbative QCD).
- [104] Y. L. Dokshitzer, V. A. Khoze, and S. I. Troian, *Sov. J. Nucl. Phys.* **50**, 505 (1989).
- [105] G. Marchesini and B. R. Webber, *Nucl. Phys.* **B330**, 261 (1990).
- [106] D. Zeppenfeld, *Acta Phys. Polon.* **B27**, 1653 (1996).
- [107] J. R. Ellis, V. A. Khoze, and W. J. Stirling, *Z. Phys.* **C75**, 287 (1997), hep-ph/9608486.
- [108] V. A. Khoze and W. J. Stirling, *Z. Phys.* **C76**, 59 (1997), hep-ph/9612351.

- [109] J. Amundson, J. Pumplin, and C. Schmidt, *Phys. Rev.* **D57**, 527 (1998), hep-ph/9708458.
- [110] V. A. Khoze, S. Lupia, and W. Ochs, *Eur. Phys. J.* **C5**, 77 (1998), hep-ph/9711392.
- [111] J. M. Butterworth, V. A. Khoze, and W. Ochs, *J. Phys.* **G25**, 1457 (1999), hep-ph/9901419.
- [112] M. A. Buican, V. A. Khoze, and W. Ochs, *Eur. Phys. J.* **C28**, 313 (2003), hep-ph/0212189.
- [113] C. F. Berger, T. Kucs, and G. Sterman, *Phys. Rev.* **D68**, 014012 (2003), hep-ph/0303051.
- [114] M. Heyssler, V. A. Khoze, and W. J. Stirling, *Eur. Phys. J.* **C7**, 475 (1999), hep-ph/9805490.
- [115] M. Heyssler and W. J. Stirling, *Phys. Lett.* **B407**, 259 (1997), hep-ph/9705229.
- [116] Y. I. Azimov, Y. L. Dokshitzer, V. A. Khoze, and S. I. Troian, *Z. Phys.* **C27**, 65 (1985).
- [117] CDF, F. Abe *et al.*, *Phys. Rev.* **D50**, 5562 (1994).
- [118] D0, B. Abbott *et al.*, *Phys. Lett.* **B414**, 419 (1997), hep-ex/9706012.
- [119] C. F. von Weizsacker, *Z. Phys.* **88**, 612 (1934).
- [120] E. J. Williams, *Phys. Rev.* **45**, 729 (1934).
- [121] S. Dawson and R. P. Kauffman, *Phys. Rev. Lett.* **68**, 2273 (1992).

- [122] R. P. Kauffman, S. V. Desai, and D. Risal, *Phys. Rev.* **D55**, 4005 (1997), hep-ph/9610541.
- [123] V. Del Duca, W. Kilgore, C. Oleari, C. R. Schmidt, and D. Zeppenfeld, *Phys. Rev.* **D67**, 073003 (2003), hep-ph/0301013.
- [124] V. Del Duca, A. Frizzo, and F. Maltoni, *Nucl. Phys.* **B568**, 211 (2000), hep-ph/9909464.
- [125] M. E. Peskin and D. V. Schroeder, Reading, USA: Addison-Wesley (1995) 842 p.
- [126] F. Bloch and A. Nordsieck, *Phys. Rev.* **52**, 54 (1937).
- [127] S. Weinberg, *Phys. Rev.* **140**, B516 (1965).

